Title
Experimental study of nanofluidics and phase transitions of normal and superfluid He4

Author
Velasco, Angel Enriques

Publication Date
2014

UNIVERSITY OF CALIFORNIA,
IRVINE

Experimental study of nanofluidics and phase transitions of normal and superfluid ^{4}He

DISSERTATION

submitted in partial satisfaction of the requirements
for the degree of

DOCTOR OF PHILOSOPHY

in Physics

by

Angel Enriques Velasco

Dissertation Comittee:
Professor Peter Taborek, Chair
Professor Zuzanna Siwy
Professor Philip Collins

2014

Table of Contents

List of Figures

List of Tables

Acknowledgements

The completion of this thesis was only possible with the help and support of so many important people throughout the years. First and foremost I would like to thank God. I am grateful to my labmates Bobby, Jeff, Serah, Chris, Fawn, Chin, Andrew, Eli, and Jordan for our many research discussions, set of extra hands, and at times needed distractions to continue moving forward throughout the years. To Zuzanna Siwy and her lab for their nanopore provisions and patience while using their lab resources. The machine shop guys: Lee, Chris, and Ron. Their patience and steady hands helped me graduate much sooner than later. Jim Rutledge and his honesty throughout my academic career has been refreshing and motivating.

I am forever grateful to my advisor Peter Taborek. His zeal, guidance, trust, and example have been paramount in forming me as a scientist. My brother Nick who always had encouraging words when times got rough. To my mother and father who were my first teachers. Their courage and example led me to believe anything was possible. Finally I am forever indebted to my lovely wife Alice. Her love, sacrifice, and unwaivering support made those long nights, weekends, and setbacks endurable.

This research was funded by the National Science Foundation (NSF).

Curriculum Vitae

Angel Enriques Velasco

Education:

2007	B.S. in Physics University of California, Irvine
2012	M.S. in Physics, University of California, Irvine
2014	Ph.D. in Physics, University of California, Irvine Dissertation: Experimental study of nanofluidics and phase transitions of normal and superfluid ^{4}He Professor Peter Taborek, Chair

Work Experience:

2007 - 2009	Research and Development: Composite materials	JD Lincoln Umeco Composites
2009 - 2010	Teaching Assistant	University of California, Irvine
2010 - 2014	Research Assistant	University of California, Irvine

Publications:

A. E. Velasco, C. Yang, Z.S. Siwy, M.E. Toimil-Molares, P. Taborek, "*Flow and evaporation in single micrometer and nanometer scale pipes.*" Appl. Phys. Lett. **105**, 226101 (2014).

F. M. Huisman, A. E. Velasco, E. Van Cleve, P. Taborek "*Quartz Tuning Forks as Cryogenic Vacuum Gauges.*" J. Low Temp. Phys., 1-14 (2014).

A. E. Velasco, S. R. Friedman, M. Pevarnik, Z. S. Siwy, P. Taborek,"*Pressure-driven flow through a single nanopore*." Phys. Rev. E. **86**, 025302(R) (2012).

Abstract of the Dissertation

Experimental study of nanofluidics and phase transitions of normal and superfluid ^{4}He

By

Angel Enriques Velasco

Doctor of Philosophy in Physics

University of California, Irvine, 2014

Professor Peter Taborek, Chair

This thesis addresses the experimental results of two different research topics. The first is the experimental work of pressure driven flows in the smallest, single nanotubes ever investigated. The nanotube boundary conditions and slip lengths from argon, nitrogen, water, and helium experiments were analyzed and compared to macroscopic boundary conditions. The second research topic discusses the work on ellipsometric and quartz microbalance measurements of the 2D superfluid phase diagram of ^{4}He on alkali substrates. Ellipsometric results of sodium on HOPG provide the first evidence of the existence of the 2D critical point on an intermediate strength substrate.

Pressure driven flows through single nanopores and microtubes were measured with a calibrated mass spectrometer with pressure drops up to 30 Atm. The nanopores were between 30 nm to 600 nm in diameter and etched in mica and PET membranes of several microns thickness. Microtubes several inches long of fused quartz and nickel material were tested with diameters between 1.8 micron and 25 micron. For ^{4}He and argon gas we observed the flow transition between the free molecular and continuum regimes at 293 K and 77 K. No discrepancy between the macroscopic theory and the 30 nm nanopore data was found. Because of the exceptionally low viscosity of gaseous helium the laminar-turbulent transition could also be observed within these submicron

channels. The small viscosity of ^{4}He was too small to dampen inertial effects at a Reynolds number of 2000.

In addition to single phase gas flows, our experimental technique also allows us to investigate flows in which the nano or micro scale pipe is either partially or completely filled with liquids. The position of the intrinsic liquid/vapor interface was important for understanding this type of flow. Strong evaporation and cooling at the liquid-vapor interface can lead to freezing for conventional fluids such as nitrogen and water, which in turn leads to complex intermittent flows. Liquid helium in the normal state is a simpler system because it does not have a triple point and will not solidify at the pressures of our experiments. A systematic study of liquid helium in a 31 nm mica nanopore was done from T_λ to $T>T_c$. A no slip model accurately represented data if the Laplace pressure and the vapor pressure at the interface were present. The model can also make predictions of the internal location of the liquid/vapor interface as a function of pressure. We also optically investigated the effects of freezing on the liquid/vapor location with water flowing through micron scale capillaries into vacuum. The observations were combined with a numerical modeling which confirmed that external interfaces froze as the result of large evaporation rates and the low thermal conductivity of glass.

In laminar flow of classical fluids, the mass flux is linearly proportional to the pressure drop. Flow of superfluid in a pipe has dramatical different dependence on pressure drop. At low temperatures, the flow rate is almost independent of the pressure drop up to 50 Torr. The temperature dependent critical velocities fluctuated between two states within a 31 nm nanopore At $T<1.4$ K. A larger, linearly temperature dependent critical velocity was measured with a maximum value of 11 m/s. A thermal nucleation of vortices was predicted to be the source of energy dissipation. The lower second state was temperature independent and caused by the generation of vortices from a pinned site within the nanopore. In the range $1.4\ \mathrm{K}<T<T_\lambda$ the velocity exponentially approached the normal viscous state. The fast dissipation rate could be related to the 10^7 vortex cores scattering from the increasing thermal excitations and generating a complex turbulent state.

The second portion of this thesis presents the experimental results on the 2D superfluid phase diagram of helium on alkali metals. A simultaneous measurement of the total and superfluid film thickness were done with a combination of a photoelastic modulated ellipsometer and a quartz crystal microbalance. Sodium and lithium films were ablated onto the gold electrodes of a QCM at 4 K. The adsorption isotherms of ^{4}He were controlled by increasing the chemical potential from vacuum to bulk coexistence. The behavior of helium films are dependent on the strength of the substrate potential. For strong potentials such as gold and graphite the initial layers solidify while for the weaker substrate cesium films do not grow. Lithium and sodium were predicted to be intermediate in strength and for a mobile, helium film to directly grow on its surface. In addition to the superfluid transition a liquid/vapor coexistence region was predicted to also exist directly on an intermediate strength substrate. Our simultaneous QCM and ellipsometer measurements showed no clear evidence for the coexistence of 2D liquid/vapor on sodium or lithium. The gold electrodes which supported the alkali films were suspected of being too rough. We then ablated sodium on atomically smooth HOPG and the ellipsometer measured a discontinuous step at 0.5 K implying a liquid/vapor coexistence which decreased in size until it disappeared at the critical temperature $T \approx 0.7$ K. This is the first experimental evidence of a 2D critical point on sodium.

Chapter 1

Introduction

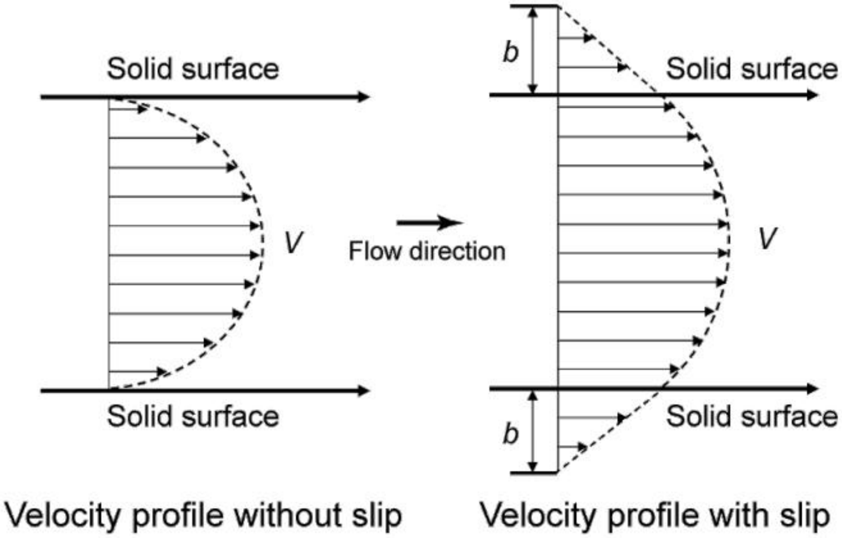

Figure 1.1: A no slip flow on the left has a parabolic velocity profile with a normal and tangential velocity of zero at the boundary. The figure on the right has a flow with a slip length of b. The slip length is the distance beyond the boundary where the tangential velocity reaches zero. A flow with slip has a larger mass flux than a flow with no slip.[4]

In a laminar flow through a pipe the velocity profile has a parabolic shape with a maximum velocity at its center and a velocity of zero at the boundaries. The zero velocity condition at the boundary is called the no slip condition. Although the no slip condition works for macroscopic pipes and channels there is no fundamental law of nature which forces this condition to be true in all cases. A non zero tangential velocity at the wall is also an acceptable boundary condition to the equations of fluid dynamics. Slip at the wall reduces viscous dissipation and increases the total mass flow through a channel. Flow enhancements in micro and nano scaled channels are believed to be the result of slip. The slip length b can be calculated by the general equation 1.1 in which it is the proportionality constant between the tangential velocity at the wall to the rate of strain. For a pure shear flow the slip length reduces to equation 1.2 where b is the normal distance at which the velocity would reach zero. The velocity gradient at the boundary is used as the rate in the calculation. A slip length of zero is the normal no slip condition with a parabolic velocity profile. A slip length of infinity transitions a laminar flow to a Bernoulli flow with a uniform velocity profile.

$$\mathbf{v}_{\parallel} = b\mathbf{n} \cdot (\nabla\mathbf{v} + (\nabla\mathbf{v})^T) \cdot (1 - \mathbf{nn}) \tag{1.1}$$

$$\mathrm{v}_{wall} = b\frac{\partial \mathrm{v}}{\partial n} \tag{1.2}$$

The source of slip is highly debated and a large body of research exists which at times can be self-contradictory [5, 6, 7, 8, 9, 10, 11, 12, 13, 14, 15, 16]. The consensus view is that slip may be dependent on surface roughness, trapped nanobubbles, hydrophobicity, and the interaction of the particles to the boundary. Carbon nanotubes is a special example where significant enhancement of liquid and gaseous flows through an array of carbon nanotubes has been reported recently in reference [17]. In Table 2 of ref [17] an enhancement over no-slip hydrodynamic flow of two to three orders of magnitude for water and one to two orders for gaseous flows were reported. Similar results were also published in the literature by references [18, 19, 20, 21]. The atomically smooth and hydrophobic CNT boundaries were theorized to cause the massive slip lengths.

Slip is only one of many phenomena which emerge as the scales approach atomic dimensions. Since surface properties scale as L^2 and volume properties scale as L^3 as a system is reduced in size surface properties will primarily dominate $\frac{p1(A)}{p2(V)} = \frac{L^2}{L^3} = \frac{1}{L}$ [22]. For nanofluidics and microfluidics the reduced importance of inertial effects and the dominating effects of surface properties such as friction, surface roughness, surface reactions, surface charges, viscous effects, and slip will combine to create unique dynamics that differ from macroscopic systems. These nanosystems are finding applications in particle separation, filtration, liquid separation, DNA analysis, biological assays, inkjet printing, pervaporation, mass spectrometry, and high pressure liquid chromatography.

The first experimental investigations of capillary phenomena have been as early as the 16th century by Leonardo da Vinci and later by Boyle. But it wasn't until the work of Young and Laplace in the 19th century that the important theoretical framework for liquid/vapor interfaces was developed [23, 24]. They found a new energy proportional to the surface area was necessary in the thermodynamic equations to explain capillary behavior. The proportionally constant γ was the surface tension and was a result of molecules at the surface being of higher energy compared to their interior neighbors. The presence of a new energy term sets a new length scale called the capillary length $\lambda_c = \sqrt{\frac{\gamma}{\rho g}}$. ρ is the liquid density and g is the gravitational acceleration. When a system's characteristic dimension L is smaller than the capillary length surface tension effects become important. The Laplace pressure is an example of a surface tension effect. The Laplace pressure is a discontinuity in pressure across an interface which is equal to the product of the local curvature and surface tension $\frac{2\gamma}{R}$. The surface tension decreases monotonically to zero as the critical temperature is reached and the difference between a liquid and gas is no longer present.

In systems with a characteristic scale smaller than the capillary length, the dynamics of a fluid also can change. The Navier-Stokes equation in standard form reads as equation 1.3. Although it is notoriously difficult to solve because of the non-linear term a simplification can be made for nano flows. The non-linear term $\rho(\vec{v} \cdot \vec{\nabla})\vec{v})$ is on the order $\frac{\rho U^2}{L}$, where U is a characteristic velocity. The viscous term $\eta \nabla^2 \vec{v}$ is on the order of $\frac{\eta u}{L^2}$. The ratio of these is the Reynolds number. In an incompressible, steady state flow the Navier-Stokes equation becomes a simple, linear equation 1.4 for low Reynolds numbers[25]. For nano scaled channels the Reynolds number can almost certainly be considered small. Equation 1.4 along with the equation of continuity 1.5 and boundary condition with the correct slip length completely determines any isothermal flow in nano-scaled channels. If $L < \lambda_c$ and interfaces are present then the Laplace pressure must also be included in the Navier-Stokes momentum flux tensor.

$$\rho(\frac{\partial \vec{v}}{\partial t} + (\vec{v} \cdot \vec{\nabla})\vec{v}) = -\nabla P + \eta \nabla^2 \vec{v} \tag{1.3}$$

$$\nabla P = \eta \nabla^2 \vec{v} \tag{1.4}$$

$$\vec{\nabla} \cdot \vec{v} = 0 \tag{1.5}$$

For pipes with diameter measured in nanometers, flow rates are extremely small even if the pressure drop is several atmospheres, and probing the flow properties becomes experimentally challenging. Existing techniques to address this problem include the measurement of viscous forces with AFM tips [12], a μPIV method[14] or the use of an array of channels[17]. Although challenging, single nanotube detection is advantageous and desirable for several reasons. By simultaneously measuring a large array of nanotubes subtle flow behaviors could be averaged out. A dispersion of diameters and the uncertainty in open nanotubes introduces assumptions to measurements. Unwanted pathways in the membranes could also exist showing erroneously as an increased flux and wrong slip lengths. Part of this thesis presents an experimental technique capable of measuring pressure driven gas, liquid, and superfluid flows through single nanotubes utilizing a mass spectrometer.

This thesis is divided into two main categories. Chapters 2-4 are on the phenomena of slip within nano and micro meter scaled channels which is appropriately named nanofluidics. The second category in chapter 5 presents research on two dimensional phase transitions on intermediate strength substrates. Although at first glance these topics may appear to be unrelated they both can be categorized under the umbrella of surface effects on the thermo and fluid dynamics of a fluid.

The majority of chapter 2 summarizes the results for gas flows from reference [26] as well as the engineering involved in building a low temperature compatible nanofluidic system. A description on properly calibrating a mass spectrometer for flow rate measurements and procedures for etching large aspect ratio nanopores ranging in diameter from 30 nm to 1000 μm were presented. The method will be shown to be robust for a variety of gases. Similar work with mass spectrometry in flows through nano scaled orifices are found in references [27, 28]. The method can experimentally detect the transitions of a molecular to continuum flow. Helium-4 and argon data at 77 K and room temperature exhibit a clear P^2 dependance at low Knudsen numbers and a linear P dependance at high Knudsen numbers. Remarkably a laminar to turbulent transition in helium-4 was also observed. The gaseous data indicate perfectly diffuse scattering of the particles from the walls.

The majority of chapter 3 summarizes the two phase results from reference [29]. The mass spectrometer was shown to be of sufficient accuracy to measure slip lengths and transitions in flow regimes. However as a high vacuum is necessary for our mass spectrometer to work properly any liquid flow must inherently possess a liquid/vapor interface. We found this interface to affect flows in nanopores with liquid helium-4 but not in larger micron pipes with liquid nitrogen. A simple two phase model was developed which includes the Laplace pressure and a resistive pressure which differs from previous two phase models [30, 31]. A new transition was also observed for a 441 nm PET nanopore. We believe this might be evidence for an early onset in turbulence or destabilizing into a Bernoulli flow for short pipes. A variety of materials were used as the pipes including mica, polyethylene terephthalate (PET), and quartz.

Chapter 4 presents the behavior of superfluid ^4He flowing through nano scale pipes. Liquid helium-4 goes through a second order phase transition at the lambda temperature of 2.17 K. Below the lambda point a two-fluid model is used to explain the extraordinary properties that emerge. For small chemical potential gradients the superfluid fraction will flow without dissipation. Dissipation for superfluid occurs at velocities greater than a critical velocity which appears to be at times either size or temperature dependent [32]. In this chapter we present experimental data on pressure driven flows in isothermal conditions through a 31 nm mica nanopore. A very small pressure dependence is observed except near the lambda point where a slight negative dependence is observed. We compare the data to the Iordanskii-Langer-Fisher (ILF) theory which introduces a possible dissipation mechanism through thermally activated vortices.

In chapter 5 work on mapping the two dimensional phase diagram of ^4He on intermediate strength alkali metals is presented. On an intermediate strength substrate ^4He grows continuously without solidified layers and the direct interaction of a mobile phase and the substrate is possible. A complete 2D phase diagram has not been measured on lithium or sodium where the classical 2D liquid/vapor transition and the quantum superfluid transition were predicted to intersect at $T<1$ K. We simultaneously measure film growth of the total and superfluid films with a quartz crystal microbalance and an ellipsometer. We present data for sodium and lithium ablated onto QCM's which do not show evidence of a 2D critical point for helium. We then replaced the gold electrode backbone with highly ordered pyrolytic graphite (HOPG) and ablated 90 layer sodium films. This system gave us the first experimental measurement of the 2D critical temperature of 0.7 K.

Chapter 2

Gas Flow

Chapter 2 explains the fabrication, engineering, and calibration steps necessary for the measurement of flows through single nanopores. The agreement of gas flow measurements and theoretical models validate the accuracy of our results in subsequent research with two phase and superfluid flows. Although the full details are in references [26] and [33] this chapter gives a review and introduces information on our cryogenics and new measurements on the laminar-turbulent transition at the end.

2.1 Microtube and nanopore production

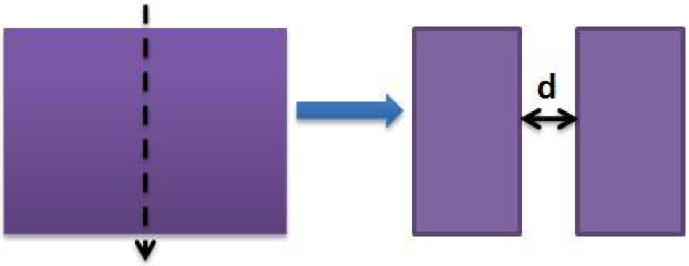

Figure 2.1: The left image shows a membrane being irradiated with a single heavy ion (Xe, Au, or Pb) creating a damaged track. The damaged track of atomic dimension serves as an initiator for the etching of cylindrical nanopores. The right image is a membrane after a wet chemical etch of the damaged track with a cylindrical nanopore of diameter D and length L. The diameter of the pore is linearly dependent on the etching time.

Single nanopores were fabricated by first irradiating mica or polyethylene terephthalate(PET) membranes, 2 cm in diameter with a single heavy ion (Xe, Au, or Pb). The thicknesses of the PET and mica membranes were 12 and 20 microns respectively. These membranes were then symmetrically etched with a 0.5 M sodium hydroxide solution at 70 C for PET [34, 35, 36] and a 10% hydrofluoric acid solution at 20 C for mica [1, 37]. At the specified conditions PET radially etches at a rate of 3nm/min and 1 nm/min for mica. Because the etching was highly anisotropic with the axial etching rate exceeding the radial etching rate by 1000 times cylindrical nanopores were fabricated. The mica membranes were found to be more susceptible to closing. Mica was precleaned in a 3 M solution of KOH at 70° for thirty minutes before etching. Diameters of the nanopores ranged between 30 nm to 1100 nm. In figure 2.3 the resulting PET nanopores had circular cross sections and the surface roughness was typically between 10% to 30% of the diameter. Mica nanopores in figure 2.2 had diamond cross sections with complimentary angles of 60 and 120 degrees.

The diameters were measured after etching by an ionic conductivity method /citeApel2001. The membrane was placed between two reservoirs filled with 1.0 M potassium chloride solution. An ionic current was created by two Ag/AgCl electrodes placing a potential difference on the order of 1 volt in the solutions. The cylindrical pore is analogous to a cylindrical wire and the conductance of the wire is proportional to the radius squared $\pi \sigma_i R^2$/L. The slope of the I-V curve determines the radius of the nanopore with σ_i as the bulk ionic conductivity of $10\frac{S}{m}$ and L is the thickness of the membrane. Figure 2.4 shows a visual representation of an ionic conductivity measurement.

A set of fused quartz, microtubes with an internal diameters of 1.8, 5, and 10 μm were purchased from Polymicro Technology. An outer polyimide coating was burned away revealing outer diameters of 150 μm for the 1.8 micron pipes and 353 μm for the rest. Electroformed nickel pipes with an internal diameter of 25 μm and outer diameter of 360 μm were purchased from Valco Instruments Co. Inc. The pipes were cleaved to the length 1″ for glass and 12″ for nickel. The glass microtubes were epoxied with Stycast 2850FT midway into a 1.895″ copper disc with a 0.1″ hole. A cell was constructed for the glass pipes by sealing the copper disc into two 2 3/4″ conflat pieces

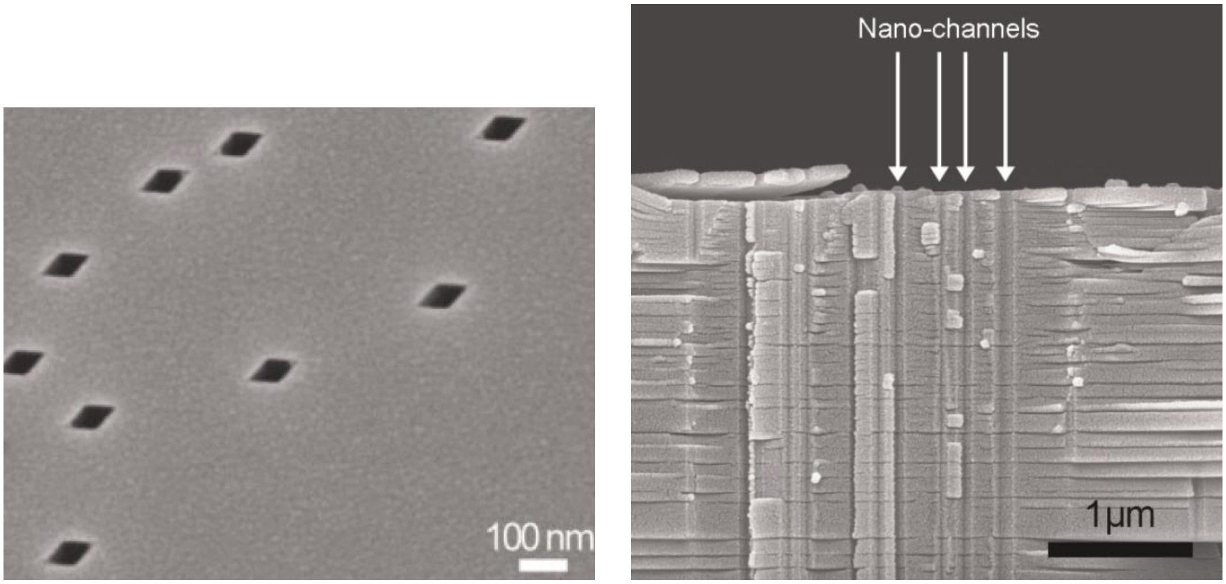

(a) Mica nanopores with diamond cross sections are etched with complimentary angles of 60 and 120 degrees in either 10% to 20% HF solutions. Single mica nanopores were used in all experiments.

(b) Cleaved mica membranes exposes etched nanochannels. Very little surface roughness is observed.

Figure 2.2: Mica cross section and roughness.[1]

with 1/4″ VCR male connectors. The nickel capillary was soldered into two 1/4″ VCR female fittings.

2.2 Mass Spectrometer Calibration

The configuration used in all nanopore and microtube experiments is shown in figure 2.5. A high pressure side consisted of a pressure reservoir, an Omegadyne PX309-1KG5V pressure gauge, MKS 1000 Torr Baratron Gauge and needle valve. The low pressure side was maintained at a high vacuum by either a turbo or diffusion pump backed by a rotary vane pump. A pirani gauge and mass spectrometer measured pressures while a NIST calibrated ^4He leak was used to convert the measured pressures into flow rates. The cell containing the micropipe or nanopore was inserted creating a barrier between the low and high pressure sides. A residual gas analyzer (RGA) mass spectrometer from Stanford Research Systems was used in combination with a Lesker Series 945

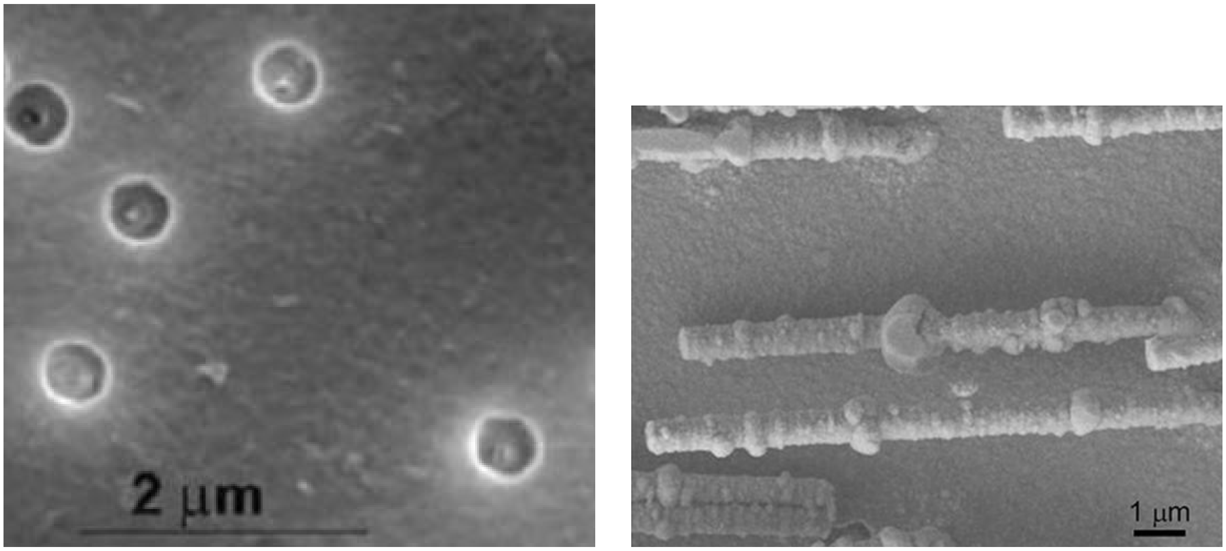

(a) PET nanopores etched in sodium hydroxide solution. Single PET nanopores were used in all experiments.

(b) Gold was electrodeposited into the PET membranes forming gold nanowires. The membrane was subsequently etched away revealing the interior profile with a surface roughness of 10-30%.

Figure 2.3: PET cross section and roughness.[2, 3]

pirani gauge as the flow meters. The experimental range of flow rates we could measure were from 1.0×10^{10} to 1.0×10^{21} $\frac{particles}{s}$. With appropriate ultra high vacuum materials and procedures this design can be improved to fifteen orders of magnitude ranging from 1.0×10^{6} to 1.0×10^{21} $\frac{particles}{s}$. The calibration constant was measured each run and was the ratio of the known NIST calibrated leak flow rate 4.45×10^{12} $\frac{particles}{s}$ to the measured pressure. The calibration constant was accurate as long as the pressure gauges were within their tolerable ranges and the pumping speed was constant. For higher flow rates where the pumping speed no longer was constant those data sets were excluded.

The cell for the membrane needed to be low temperature compatible and permit removal of the membranes after sealing. Two metallic pieces $2''$ in diameter and $3/4''$ thick compressively sealed the membrane between two indium O-rings withstanding a pressure of 5 Atm. Stainless steel was used for experiments at 77 K and oxygen-free high thermal conductivity copper (OFHC) for liquid helium temperatures at ≈0.5 K to ensure an isothermal system. The $515 mm^3$ internal volume was

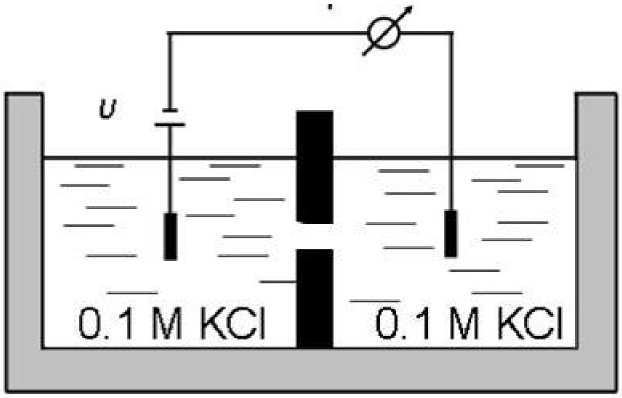

Figure 2.4: An etched membrane is placed between two 1.0 M potassium chloride reservoirs. Two Ag/AgCl electrodes place a potential difference of order 1 volt. From the slope of an I-V curve the diameter is measured [34].

filled by slowly condensing vapor through a 1/8″ VCR connector. The exit of the cell was pumped through a 1/4 ″ VCR connector.

Helium is the smallest, most inert noble gases earning it the title champion of diffusion. We correctly assumed diffusive flows through thin, polymer membranes could overshadow the minute flows through a nanotube at room temperature. Since the diffusion constant exponentially decays with temperature in theory there exists a temperature at which diffusion becomes insignificant. Figure 2.6 shows the experimental diffusion constant of helium through a 12 μm thick PET film from room temperature to 100 K. Below 100 K the diffusion constant was too low to measure. All experiments with membranes were performed at T<77 K to ensure diffusion would be negligible.

2.3 Cryogenic engineering

For experiments at T=77 K the stainless steel cell was submerged in liquid nitrogen to ensure an isothermal environment. For liquid helium temperatures the OFHC cell was mechanically and thermally secured to a continuous $^3He/^4He4$ pulse tube cryostat described in detail in ref. [38]. The cryostat is composed of two components, the cryogen free, pulse tube which cools two plates to 40 K and 4 K and a pair of evaporative refrigerators on the third plate. The incoming $^3He/^4He$

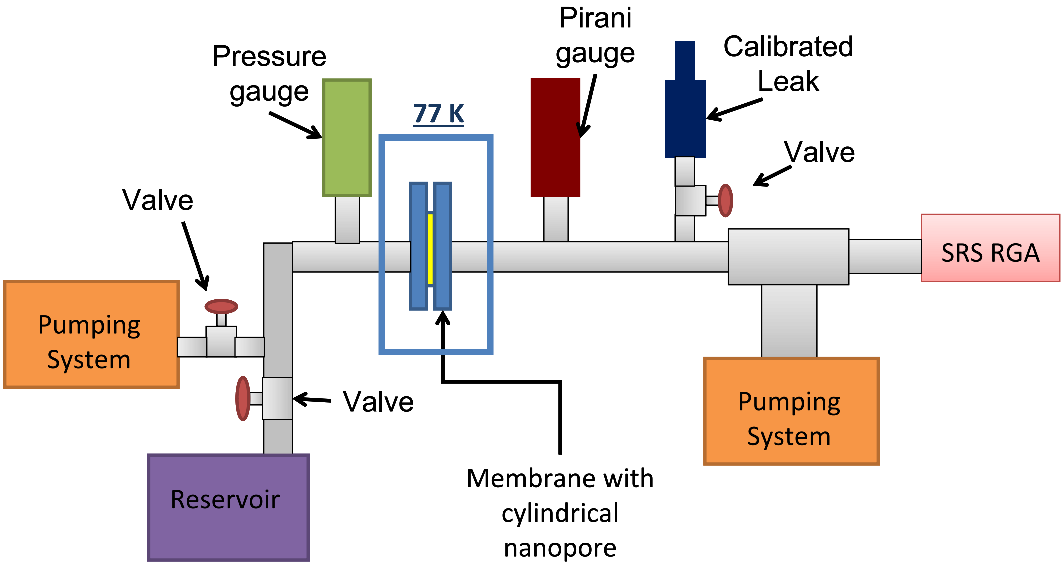

Figure 2.5: The membranes were sealed with indium o-rings in either a stainless steel or oxygen-free copper cell. A high pressure reservoir connected to a pressure gauge and needle valve introduced the fluid to one side. A turbo or diffusion pump backed by a rotary vane pump created the high vacuum environment for the mass spectrometer to function. A Lesker 945 series pirani gauge was also used for higher flow rates. A NIST ^4He leak calibrated the pressure measurements into quantitative flow rates for ^4He.

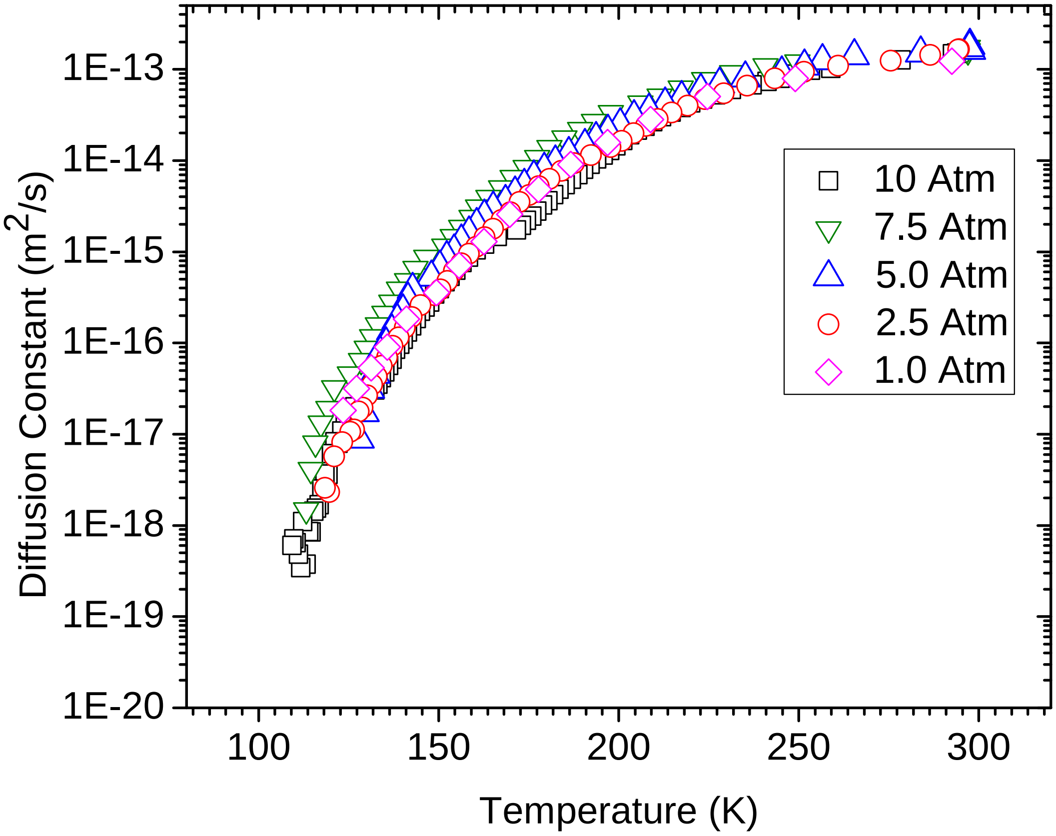

Figure 2.6: Measured diffusion constant of ^4He through a 12 μm thick PET membrane as a function of temperature at constant pressures. At T>100 K the diffusion rates were detectable.[33]

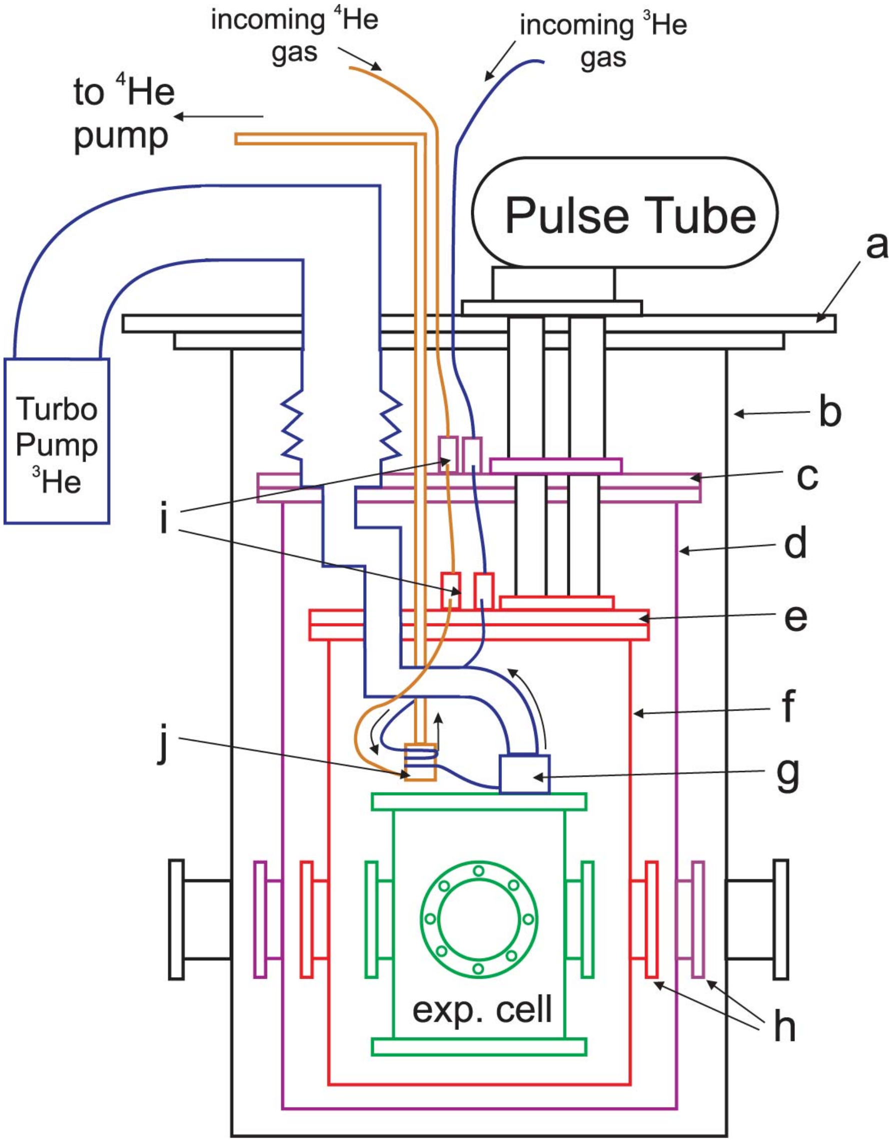

Figure 2.7: The schematic diagram of the pulse tube cryostat from reference [38].The labeled components are a) stainless steel vacuum flange; b) stainless steel outer vacuum can; c) large copper plate attached to the first stage of the pulse tube (40 K); d) 40 K copper radiation shield; e) copper plate attached to the lower stage of the pulse tube (4 K); f) 4 K copper radiation shield; g) helium-3 refrigerator; h) IR-absorbing windows; i) heat sinks to the 40 K and 4 K plates for the ^3He and ^4He refrigerator input lines; j) ^4He refrigerator, used to cool and liquefy the incoming ^3He gas to 1.5 K; k) experimental cell. The cell can reach a temperature of ≈0.4 K with 2.5 mW of cooling power. The total cool down time is ≈18 hours.

gas lines are thermally sunk to each plate precooling them to ≈ 4 K. The ^4He evaporative pot was thermally isolated from the third plate and precools the ^3He further to ≈1.5 K. The precooled helium-3 enters its own evaporative pot through an impedance of order $1.0 \times 10^{18} m^{-3}$ and cools the third plate to 0.4 K with 2.5 mW of cooling power. Temperatures on the third plate were measured with calibrated germanium and carbon-glass thermometers.

2.4 Microtube and Nanopore Data

Kn	Flow type	Q	C
$\gg 1$	effusion through hole or specular reflection in long tube	$\frac{\Delta P \pi R^2}{\sqrt{2\pi m k_B T}}$	$\frac{\pi}{\sqrt{2\pi m k_B T}} R^2$
$\gg 1$	diffuse reflection in long tube	$\frac{8\Delta P \pi R^3}{3L\sqrt{2\pi m k_B T}}$	$\frac{8\pi}{3L\sqrt{2\pi m k_B T}} R^3$
$\ll 1$	laminar flow	$\frac{P}{2k_B T} \frac{\pi \Delta P R^4}{8\eta L}$	$\frac{P}{2k_B T} \frac{\pi}{8\eta L} R^4$

Table 2.1: Number flow rate Q and conductance C for various flow regimes

The experimental conductance for the microtubes and PET nanopores correspond well to theory in figures 2.8 and 2.9. The conductance C was derived from equation 2.1 as the ratio of particle flow rate Q to pressure drop ΔP_R. Because the low pressure side of the nanopipe is connected to the mass spectrometer where the pressure is zero, $\Delta P_R \approx P_R$. The conductance was plotted as a function of the Knudsen number K_n which is the ratio of the average mean free path of a particle to the diameter of the pipe $\frac{\lambda}{D}$. Equation 2.2 has the temperature T, Boltzmann constant k_B, and mass of a particle m. The viscosity of helium gas η from 0.5 K to 300 K is equation 2.3 from reference [40]. For K_n greater than one a pressure independent conductance is observed while for K_n less than 0.01 a conductance proportional to P_R is measured for the microtube and nanopore data. Table 2.1 summarizes the gas conductance in the asymptotic limit. The microtube data shows a temperature dependence for helium at 293 K and 77 K as well a mass dependence for argon and helium. The nanopore conductance were shown normalized to their respective free molecular conductance. The black theoretical lines assume no-slip, laminar flow for $K_n < 0.01$ and perfectly diffusive boundary condition for $K_n > 1$.

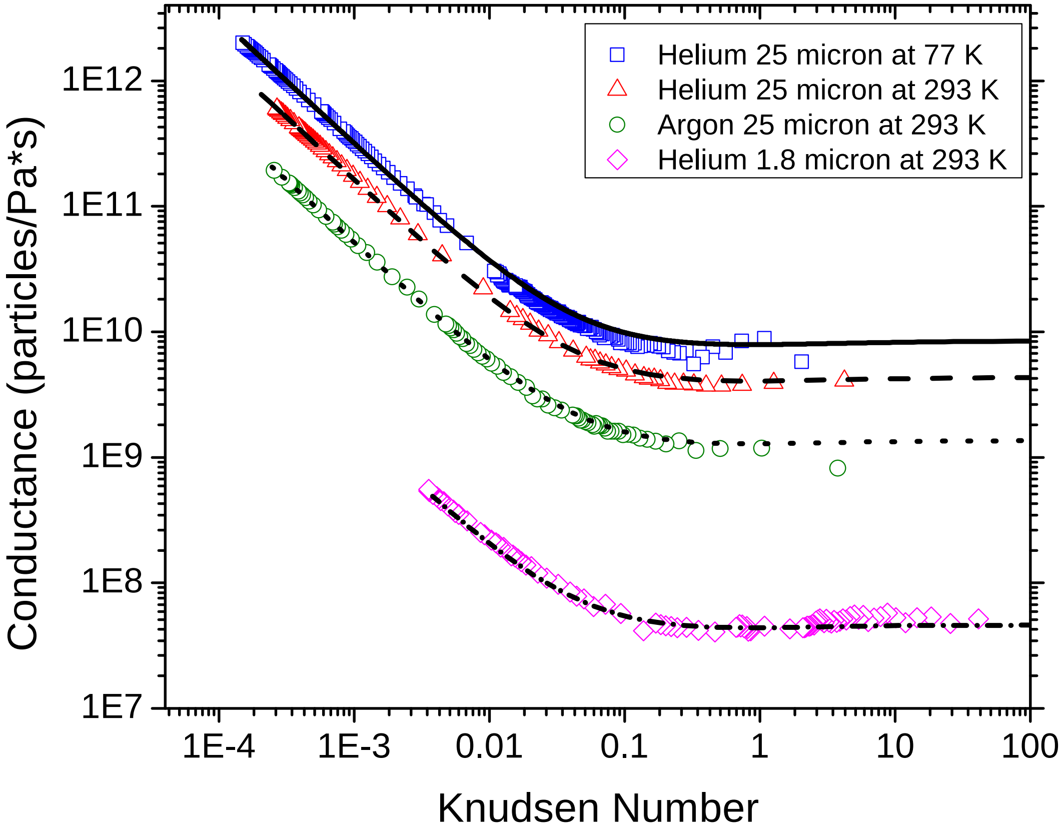

Figure 2.8: The conductance of ^4He and argon in nickel and glass capillaries are plotted as a function of Knudsen number. The colored symbols represent the data while the black lines represent a unified theory by Sharipov[39]. The lengths of the nickel and glass micropipes are 12″ and 1″ respectively. At $K_n > 1$ the conductance was pressure independent and at $K_n < 0.01$ the conductance transitions to a linear pressure dependance. The no slip and diffuse boundary conditions worked well for the continuum and molecular regimes. The temperature dependance of the conductance can also be observed between the 77 K and 293 K data [26].

$$Q = C\Delta P_R \tag{2.1}$$

$$K_n = \frac{\eta\sqrt{2\pi k_B T}}{2DP\sqrt{m}} \tag{2.2}$$

$$\eta = 4.602 \times 10^{-7} T^{0.659} - 3.64 \times 10^{-7} T e^{-0.537T} \tag{2.3}$$

2.5 Free molecular flow, hydrodynamic flow, and the transition between them

In the continuum limit (K_n<0.01) the no slip Poiseuille conductance fits the data plotted in figures 2.8 and 2.9. In no slip, laminar flows the velocity is parabolic with a velocity of zero at the boundaries. The flow regimes are classified by the Knudsen number and displayed in table 2.1. The transition regime between the free molecular and continuum begins at $K_n = 1$. At this point the assumption that particles are non-interacting cannot be made anymore. A complicated combination of viscous and ballistic theory are in play in this regime. Empirical and numerical solutions exist which connect the free molecular and continuum limits [39]. Figure 2.10 shows several of these theories normalized to the free molecular theory. The unified theory by Sharipov in equation 2.4 were plotted as theory in our figures. The one dimensional velocity v_m is $\sqrt{2k_B T/m}$ and the function G_p is defined in [30].

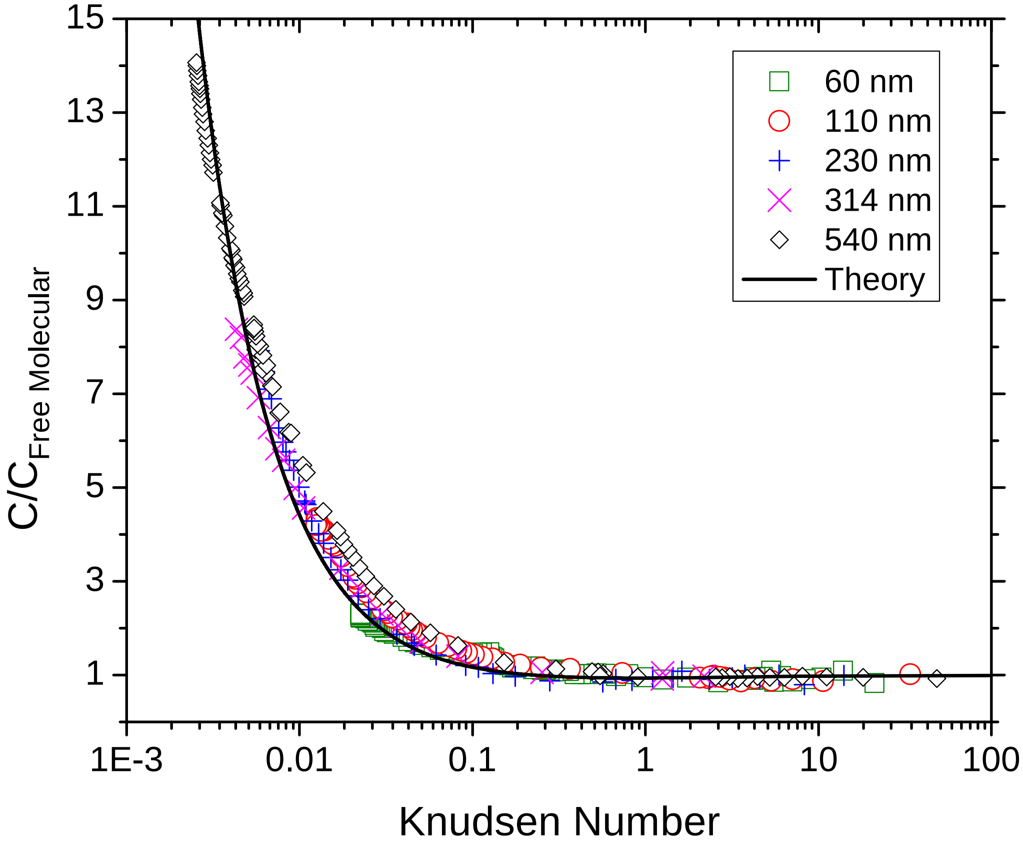

Figure 2.9: The PET conductance data for diameters of 60 nm, 110 nm, 230 nm, 314 nm, and 540 nm are presented. The length of the nanopore was 12 μm. The conductances were normalized to the constant free molecular conductance. A pressure independent conductance was seen for $K_n > 1$ and at $K_n < 0.01$ the conductance is linearly dependent on the pressure. The black line assumes no slip in the continuum limit and diffuse boundaries for the free molecular limit [26].

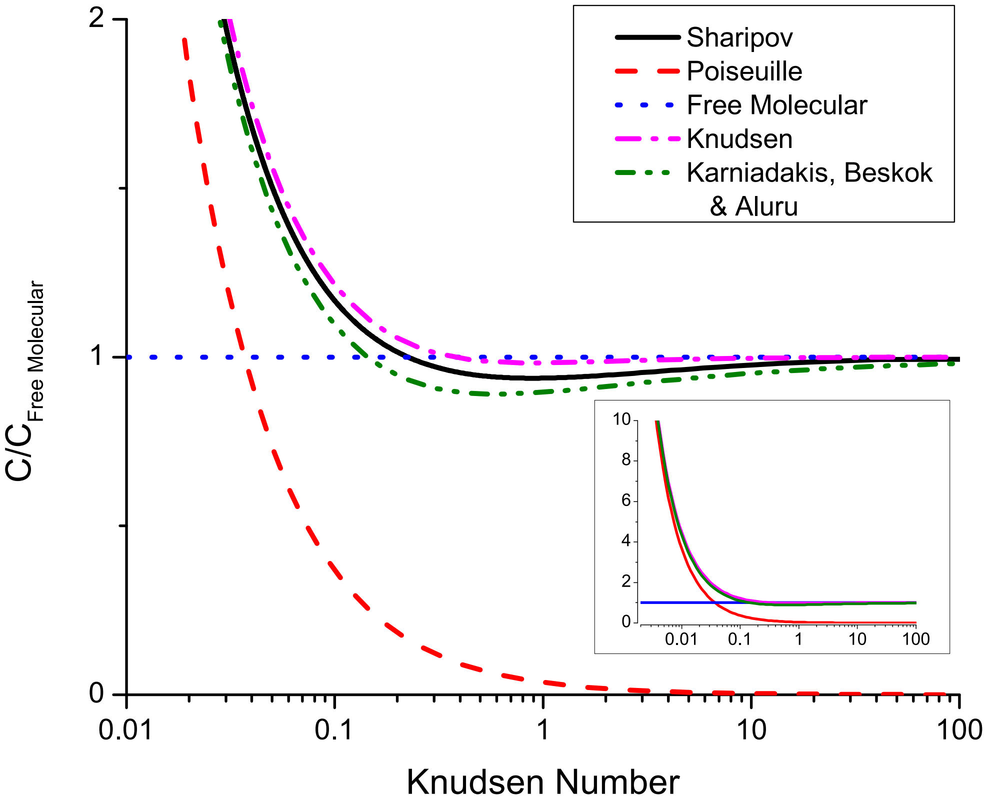

Figure 2.10: The theoretical conductances for several unified theories were plotted. The continuum and free molecular conductances were also included as the red, dashed line and blue dotted line. All conductances were normalized to the constant free molecular conductance. The insert shows the unified conductances approaching Poiseuille's conductance at $K_n < 0.01$ [26].

$$Q_g = \frac{\pi R^3}{\mathrm{v}_m L} \int_0^{P_{int}} G_p\left(\frac{PR}{\eta \mathrm{v}_m}\right) \mathrm{d}P \tag{2.4}$$

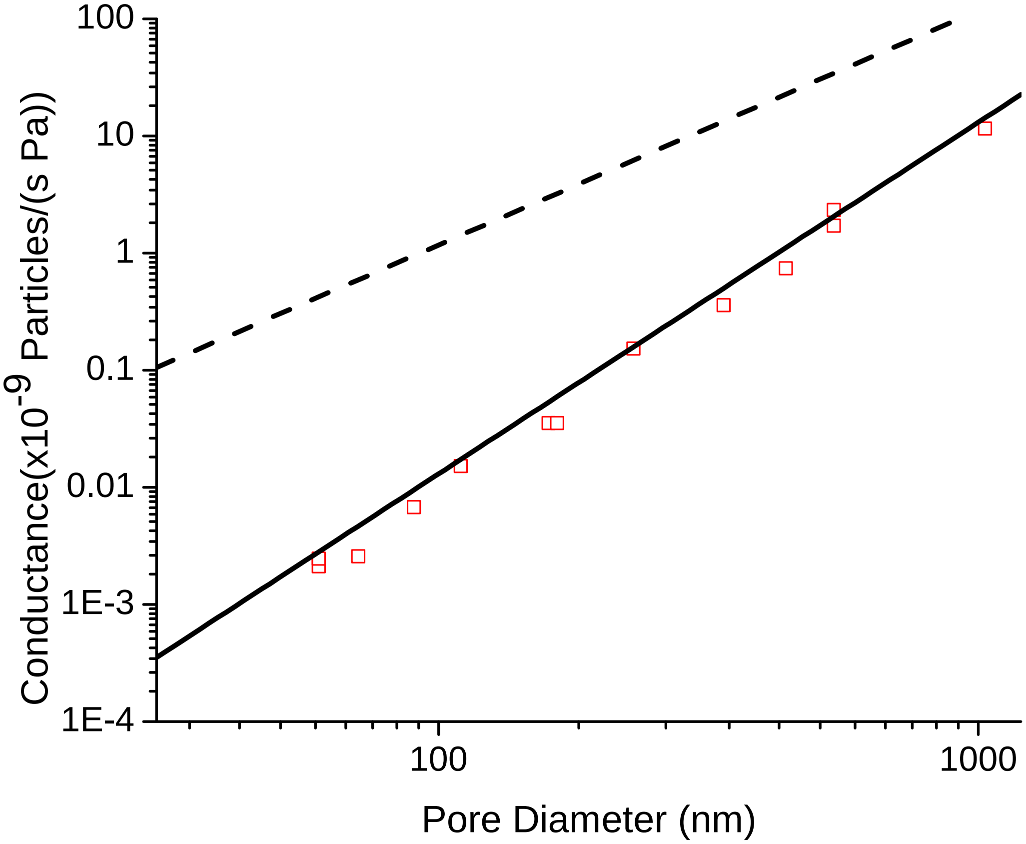

Figure 2.11: The free molecular conductance were plotted as a function of diameter. The diameters were measured two ways. By an ionic conductivity method and gas flow measurements. The black, dashed line was the conductance for an orifice which scales as R^2. The solid, black line scales as R^3 and was for pipes with perfectly diffusive boundaries. There was no evidence of a specular boundary in PET nanopores [26].

The mass flow in the free molecular regime is proportional to the probability that a single particle enters a pipe and traverses the full length to the exit. Part B and C of figure 2.12 illustrates free molecular flows with either diffusive or specular surfaces. For diffusive surfaces the probability for a particle to be transmitted equals to $\frac{8R}{3L}$ [41]. The probability in specular pipes is simply unity where every entering particle is transmitted. The proportionality constant is the total number of incident particles $\pi R^2 \frac{P}{\sqrt{2\pi k_B m T}}$. Flow rates therefore are expected to scale as R^3 for diffuse surfaces and R^2 for specular. Figure 2.11 plots measured gas conductance as a function of the nanopore diameter from ionic conductance measurements. A clear R^3 dependance was observed which points to nanopores with perfectly diffuse surfaces.

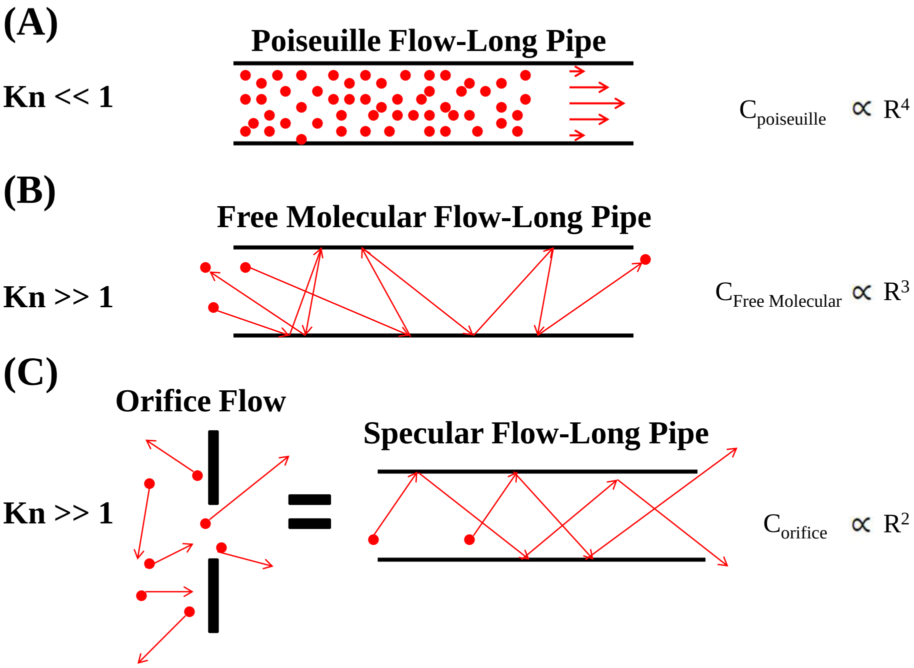

Figure 2.12: Top: Dense fluid through a pipe in the continuum regime. Particle-particle interactions are important, and the mass flow rate Q and the conductance C are proportional to R^4. Middle: Flow of a rarefied gas in a long pipe with diffusive scattering at the walls. C is proportional to R^3. Bottom: Flow of rarefied gas through an orifice is equal to the number of particles incident on the area of the aperture which scales as R^2. A long pipe with specular reflection at the walls has the same conductance [26].

2.6 Laminar-Turbulent Transition

While sweeping through a variety of diameters we measured by fortunate chance a laminar to turbulent transition in a 441 nm PET nanopore. Turbulence at small length scales was not expected since large pressure gradients were typically necessary to destabilize the flow[42]. Viscous forces normally dominate over inertial terms and the Reynold's number $\frac{\rho v D}{\eta}$ in our flows was on the order of ≈ 1. Fortunately the viscosity of ^4He was sufficiently reduced at 6 K that a laminar to turbulent transition was observed in the larger 441 nm nanopore. At Re=2000 the flow approached the new state from above eventually leveling off near 20 Atm. At the transition the velocity profile was expected to change from a parabolic profile to a nearly flat logarithmic profile at its center. The average turbulent flow (equation 2.5) depends inversely on the relative roughness $\frac{d}{R}$ of the surface and on an empirical constant κ named after von Karman[25]. Figure 2.13 assumes a relative roughness of 10% and the von Karman value of 0.4 for a pipe. A clear change in pressure dependence was observed from a quadratic to linear dependence at the laminar-turbulent transition. The large surface roughness was a result of the etching process and 10% was a reasonable value[43, 3].

$$Q = \frac{\Delta P \pi R^2}{2k_B T}\sqrt{\frac{R k_B T}{\kappa^2 m L}}\, ln[\frac{R}{d}] \tag{2.5}$$

2.7 Conclusion

We have devised a robust way to measure gas flows through single nanotubes and observe transitions between the molecular and continuum regimes. In subsequent chapters this method was extended to liquid and superfluid systems at cryogenic temperatures. With this large range of temperatures we gain access to a wide range of flow parameters which are difficult to achieve using conventional methods. Helium is a unique fluid with a number of features which could help give insight to flows at the nano scale. Its weak interaction gives it the ability to wet almost any surface and have a wetting contact angle of zero. The simple atomic structure and Van der Waals interaction is much simpler to model than water. The viscosity of helium is exceptionally low and the study of turbulence within nanotubes is possible with pressure gradients of only a few atmospheres.

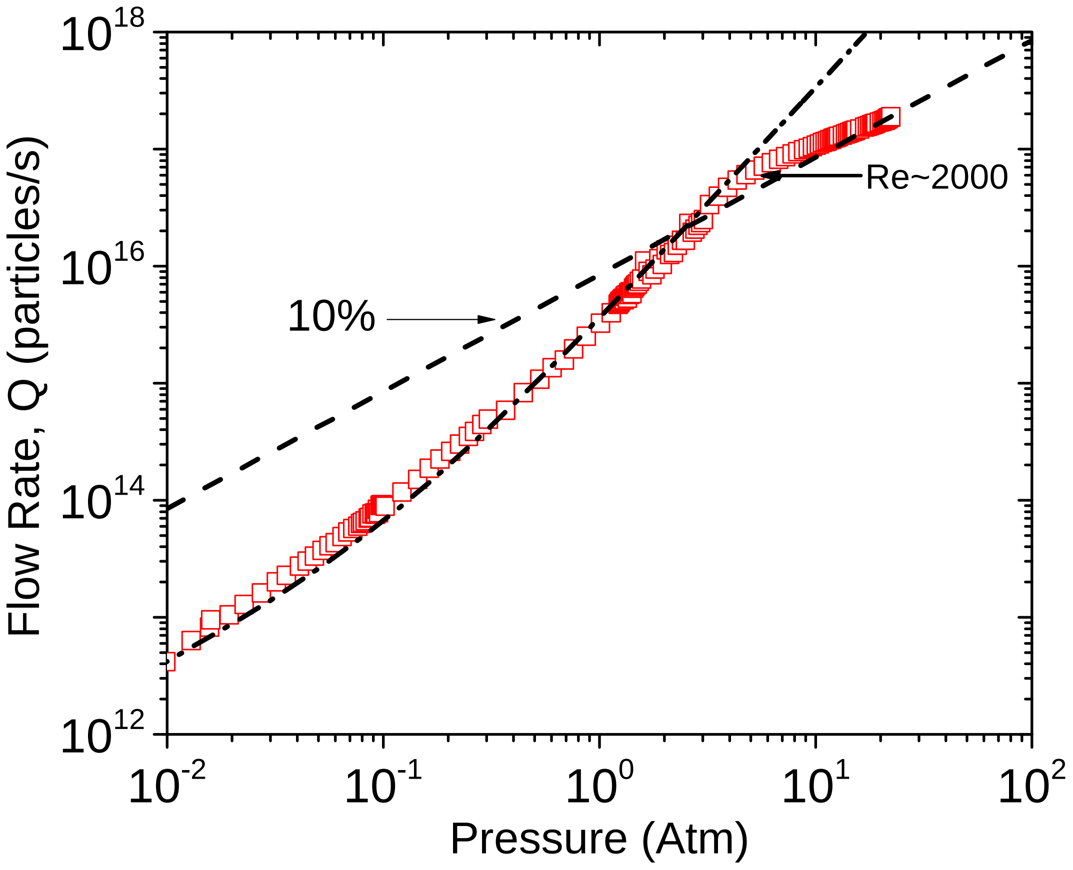

Figure 2.13: A laminar to turbulent transition was observed at a Reynolds number of 2000. Typically in a 441 nm PET nanopore viscous forces would dominate but at 6 K the viscosity of ^4He was sufficiently low that an instability could grow. The turbulent theory was plotted as the dashed line with a relative roughness of 10%. The dash dotted line was the laminar theory by Sharipov.

Turbulence research within nanotubes we believe remains highly uncharted. The effects of surfaces on the onset and development of turbulence within a nanotube has not been experimented and could lead to novel behavior. The relationship between flow rate and surface roughness can be exploited as a tool in characterizing nanopore surface profiles by the measurement of turbulent flow rates.

Chapter 3

Two Phase Flow

3.1 The role of slip and the position of the liquid-vapor interface

A portion of data in this chapter was published in reference [29]. We investigated the versatility of a mass spectrometer as described in section 2.2 to the measurement of slip in liquid flows. The slip length is the normal distance beyond the boundary at which the velocity linearly reaches zero. Slip in micro and nano scaled channels appears as enhancements in flow rates [17, 19, 20] and can be related to the smoothness and hydrophobicity of a surface [44]. We have made independent measurements of the flow rates and the geometric properties of our pipes to calculate slip lengths with equation 3.1 where λ_s is the slip length and ρ_N is the average particle density.

$$Q_s = \rho_N \frac{\pi \Delta P}{8 \eta L} \left(R^4 + 4R^3 \lambda_s \right) \tag{3.1}$$

The liquid/vapor interface was intrinsic to our system because the mass spectrometer must operate in high vacuum. The role of surface tension became important since the capillary length λ_c was greater than the diameter of the pipes. For a normal experimental run the pressure of a gas was increased until the saturated vapor pressure (SVP) or bulk coexistence was reached whereby liquefaction occurred. The liquid was then wicked into a horizontal capillary by surface tension

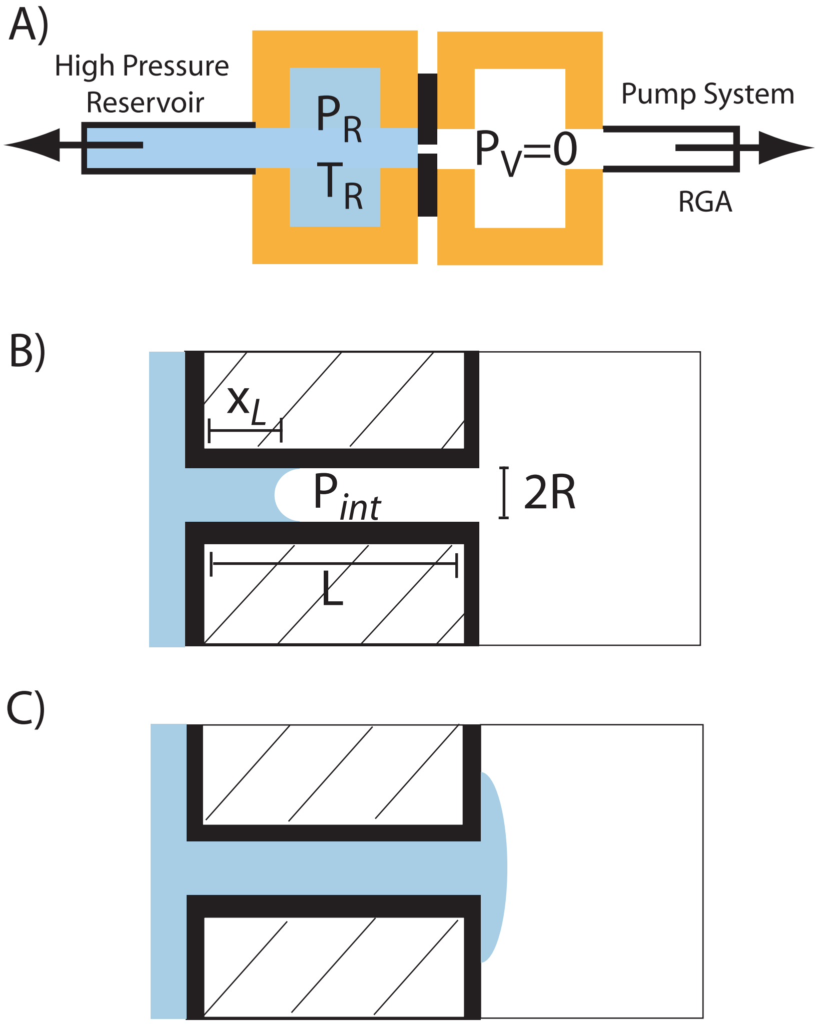

Figure 3.1: Schematic diagram of the apparatus. (A) Overall view which shows a high pressure reservoir at pressure P_R and temperature T_R and a low pressure section at pressure $P_V \approx 0$ connected to high vacuum pumping system and an RGA mass spectrometer. The two sections were separated by a flow impedance, which was either a micron-scale pipe or a nanopore. (B) The pipe has length L and diameter 2R. In some cases, the liquid/gas interface occurs inside the pipe at a distance x_L from the inlet. The pressure in the vapor at the interface is P_{int}. (C) In other cases, the liquid fills the pipe and evaporates from a droplet that forms on the end of the pipe [29].

forming a liquid/vapor interface. The position of the meniscus was dependent on the balance of the flow rate and evaporation. Figure 3.1 shows the possible meniscus positions. An external interface was present when the liquid mass flow Q_L was greater than the evaporation from the interface Q_{evap}. If Q_{evap} was greater than Q_L an internal interface was present. The interface position x_L was the solution to equations 3.2 and 3.4 as long as the quantity $(L - x_L)$ was greater than ten diameter lengths from the exit. With the solution to x_L equation 3.3 correctly predicts an internal flow rate with P_{int} being the pressure at the interface and the surface tension γ at the value at T_R.

$$Q_g = \frac{\pi R^3}{\mathrm{v}_m (L - x_L)} \int_0^{P_{int}} G_p\left(\frac{PR}{\eta \mathrm{v}_m}\right) \mathrm{d}P \tag{3.2}$$

$$Q_L = \rho_N \frac{\pi \Delta P}{8 \eta x_L} (R^4 + 4R^3 \lambda_s) \tag{3.3}$$

$$\Delta P = P_R - \left(P_{int} - \frac{2\gamma}{R}\right) \tag{3.4}$$

3.2 Optical and Mass Flow Cell

The construction procedure for the nanopores and microtubes as well as data acquisition methods were described in sections 2.1 and 2.2. Although the etching procedure for mica and PET were similar the resulting cross sections and surface roughness were different. Figure 2.3 and 2.2 shows PET's fairly circular cross section and mica's diamond cross section respectively[1, 2]. An effective diameter for mica was obtained from ionic current and gas flows measurements as described in section 2.1 and using equation 2.4. The surface roughness of mica was typically of atomic smoothness with slight roughness due to the etching procedure while PET can have roughness on the

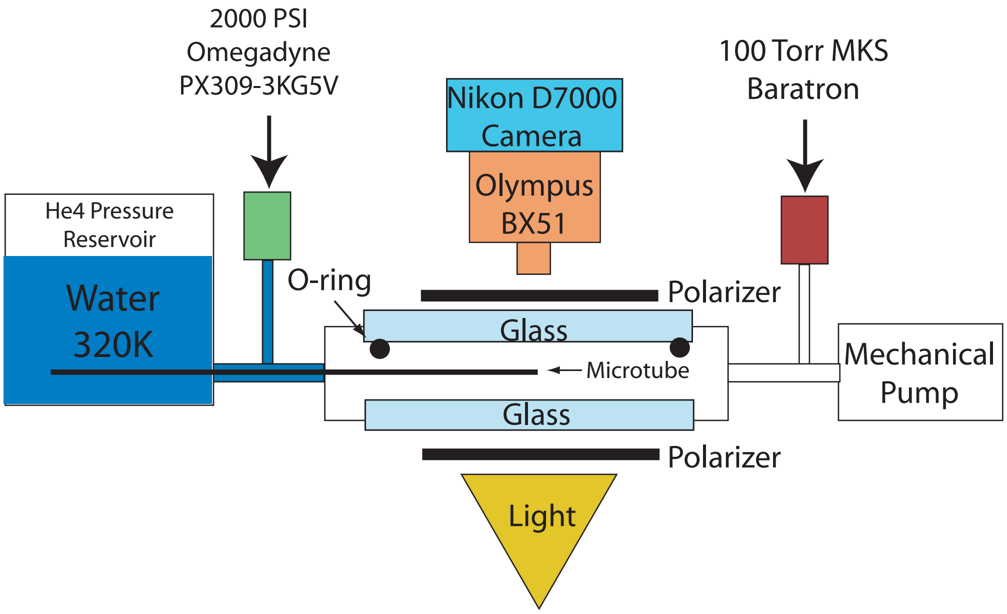

Figure 3.2: The location of a water meniscus in quartz microtubes of 10 μm diameters were imaged with a Nikon 7000 camera, Olympus BX51 microscope, and two objective lens of 20x and 50x magnification. Deionized water pressurized up to 20 Atm and heated to 320 K was introduced into an aluminum optical cell under a vacuum of 100 mTorr.

order of 10% to30% of its diameter. Temperature regulation of the cells were described in section 2.3 for liquid nitrogen and liquid helium temperatures.

An optical study was also undertaken of deionized water into vacuum at a reservoir temperature of 320 K. Flow rate measurements were not possible for comparison due to large background water vapor pressures. All optical images of water flowing into vacuum through a microtube were taken with the setup in figure 3.2. An aluminum cell with optical access was built to observe deionized water entering vacuum through a 10 μm micropipe. A Nikon D7000 attached to an Olympus BX51 optical microscope with a 10x and 50x objective lens served to image the meniscus and droplet. Two linear polarizers set orthogonally on either side of the cell illuminated ice formation. A Vision Research Phantom v7.2 high speed camera was used to take video at 1000 fps. The cell's dimensions had an outer diameter of 2-1/4″, 1-1/2″ inner diameter, and 3/4″ thick with a single rubber O-ring to seal a removable two inch window for access. A secondary 2″ diameter window was permanently epoxied to the cell opposite to the first for backlighting of the microtube. A 1/4″ VCR and ultra-torr port were used to vacuum and insert a sample into the cell respectively. A 5″ microtube was epoxied into a 1/4″ copper pipe with 1″ protruding from the copper pipe into the optical cell. The outer polyimide coating was removed exposing the fused quartz to allow transparency. The 1/4″ copper tubing with the epoxied capillary was inserted through the ultra-torr fitting and temperature controlled with the cell and water reservoir to 320 K. Deionized water was boiled for thirty minutes to degas and inserted into a helium pressurized reservoir which can be raised to a max pressure of 20 Atm. An MKS Baratron 100 Torr and Omegadyne PX309-3KG5V 0-2000 psig measured the vacuum and high pressure sides respectively. The Nikon camera images and videos were taken with the Nikon software Camera Control Pro 2.

3.3 Modeling with COMSOL

A numerical model was implemented to predict the liquid/vapor interface location by simultaneously solving the heat and momentum equations for a liquid and the thermal equation for the channel itself. A solution to the coupled partial differential equations 1.3,1.5, and 3.5 was easily produced by the finite element method (FEM). The FEM software COMSOL 4.3 is specifically designed for multiphysics simulations by solving simultaneous sets of PDE's numerically. A 3D rendering was drawn and the appropriate boundary conditions applied. In all instances a heat flux (Eq. 3.6) at the liquid/vacuum interface was simulated by the removal of latent heat L_{vap} at a rate equal to the Hertz-Knudsen relation 3.7. Although the Hertz-Knudsen relation was believed to be an incorrect equation for the mass flux it was a good starting point for understanding the qualitative behavior [45, 46, 47].

$$\frac{\partial T}{\partial t} + (\vec{v} \cdot \vec{\nabla})T - \frac{\kappa}{\rho C_p}\nabla^2 T = 0 \tag{3.5}$$

$$H_{evap} = L_{vap} J_{evap} \tag{3.6}$$

$$J_{evap} = |\frac{m(P_s - P_0)}{\sqrt{2\pi m k_b T}}\vec{n}| \tag{3.7}$$

3.4 Flow of Nitrogen

3.4.1 Microtubes

Before measuring the flow rates in nanotubes the robustness of the mass spectrometer to liquids was examined first in microtubes. Flow data of nitrogen at 77 K in fused silica pipes 1″ long and 1.8 μm, 5 μm, and 10 μ diameter are shown in figure 3.3. A clear discontinuity at the saturated vapor pressure (SVP) of 1 Atm is present where a transition from gas to liquid occurs. At low pressures a P to P^2 dependance is indicative of a free molecular to laminar transition. At pressures greater than the SVP gas condensed and filled the microtube completely with liquid. The data has a linear pressure dependance up to 30 Atm which means a laminar, no-slip liquid flow with the Laplace pressure and P_{int} set to zero in equations 3.4 and 3.1. An external meniscus or drop must

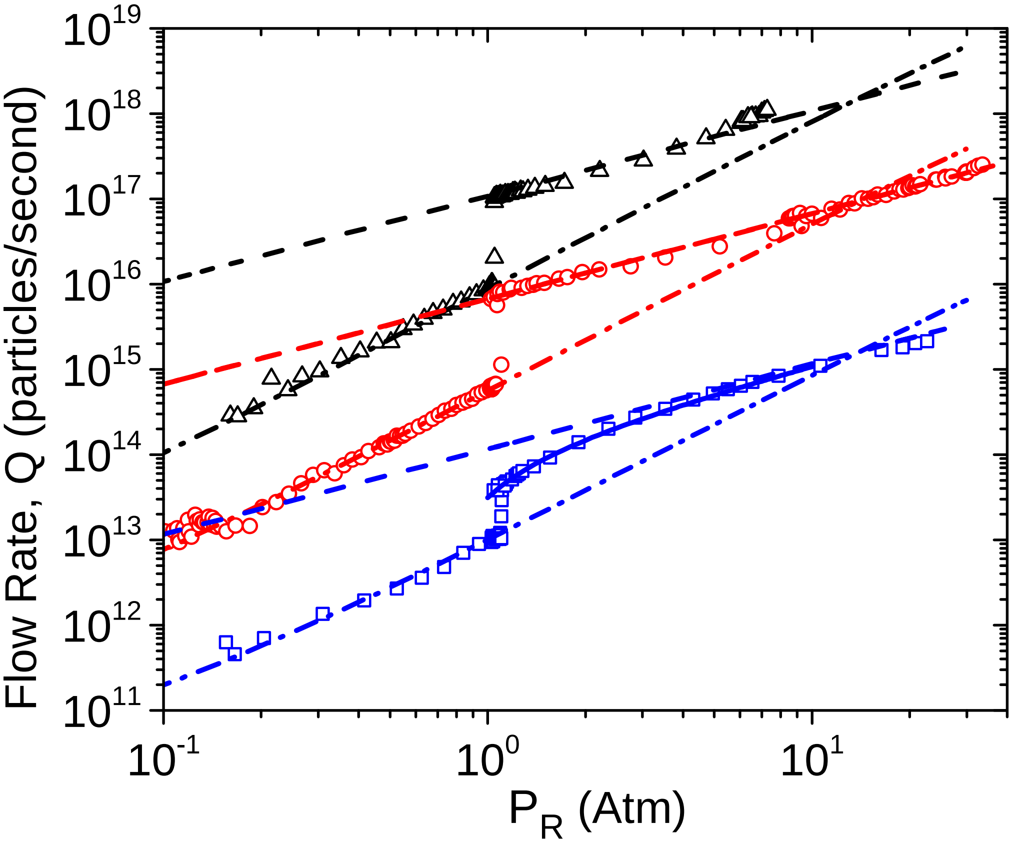

Figure 3.3: Nitrogen data at 77 K for three glass capillaries an inch long and internal diameter of 1.8 μm, 5 μm, 10 μm. The dash dotted lines were solutions to equation 2.4. The discontinuous step at P_R=1 Atm was the onset of liquefaction. The dash line was equation 3.1 for a laminar liquid flow with a slip of zero at the walls. The Laplace pressure and interface pressure were set to zero in equation 3.4 [29].

be present where the liquid evaporates into vacuum. The volume of the drop reaches a steady state size determined by the balance of influx to evaporation at the surface of the drop. With the higher densities of liquids care must be taken to ensure the pumping speed remains constant with higher mass flows. At larger flows the pumping speed may be dependent on pressure and non-linear relations might give misleading data.

3.4.2 Nanopores

The first nanoflow measurements were attempted with single PET nanopores 12 μm thick and diameter of 320 nm, 500 nm, and 540 nm. The results with liquid nitrogen are in figure 3.4. For a number of experimental runs the gas data below SVP was reproducible and the transition from a free molecular to laminar flow was clear. After the discontinuous step due to liquefaction the data was stochastic and fluctuations as large as an order of magnitude were observed. The solid black lines represent equation 3.1 and 3.4 with $P_{int} = 0$ and $\lambda_s = 0$. An explanation for the stochastic data can be from nitrogen freezing and partially closing the pore. A liquid can be frozen by pumping on it and reducing its temperature below the liquid/solid coexistence curve. To further worsen the situation the poor thermal conductance of PET was cut further by half at 77 K[48]. Thermally cycling the nanopores from 77 K to room temperature between experimental runs reinitialized the nanopore and clean gas flows were measured again. With no thermal cycling between experimental runs the gas data remained stochastic and reduced.

3.4.3 COMSOL results for nitrogen flows

An immediate distinction arises when a comparison of figures 3.4 and 3.3 was done. The solidification of nitrogen affects the nanopore data with far greater frequency than the microtube data. In only a handful of experimental runs the microtubes had stochastic flows which could imply nitrogen solidification. Temperature measurements at the interface and the surrounding material were necessary to justify solidification. Experimentally measuring temperatures in micro and nano scaled pipes was extremely challenging and not readily accessible. Instead a 3D rendering of

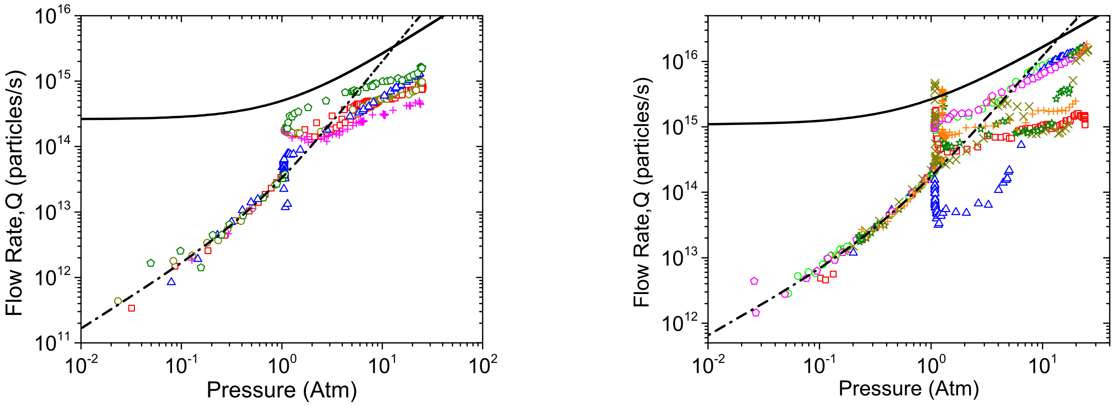

(a) The dash-dotted line is equation 2.4. The solid line was equation 3.1 and 3.4. D=320 nm diameter, $P_{int} = 0$, $\gamma = 0$

(b) The dash-dotted line is equation 2.4. The solid line was equation 3.1 and 3.4. D=500 nm diameter, $P_{int} = 0$, $\gamma = 0$

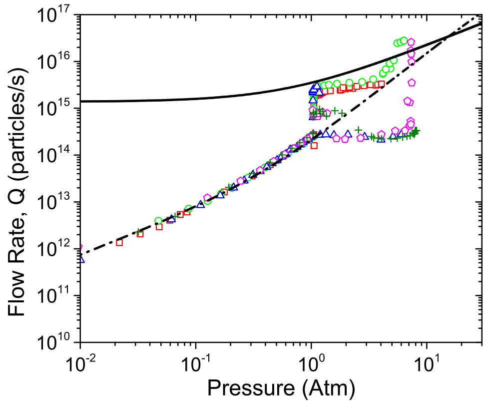

(c) The dash-dotted line is equation 2.4. The solid line was equation 3.1 and 3.4. D=540 nm diameter, $P_{int} = 0$, $\gamma = 0$

Figure 3.4: Nitrogen flow at 77 K in PET nanopores

our experiment was drawn in COMSOL and a steady state solution to the heat and fluid equations 1.3,1.5, and 3.5 were found. The material properties for fused silica and PET were derived from reference [49]. The temperature dependent properties of nitrogen such as viscosity, density, heat capacity, latent heat, and thermal conductivity were taken from NIST [50, 51, 52].

$$z = \frac{\theta(g^2 - r^2)}{2r} \tag{3.8}$$

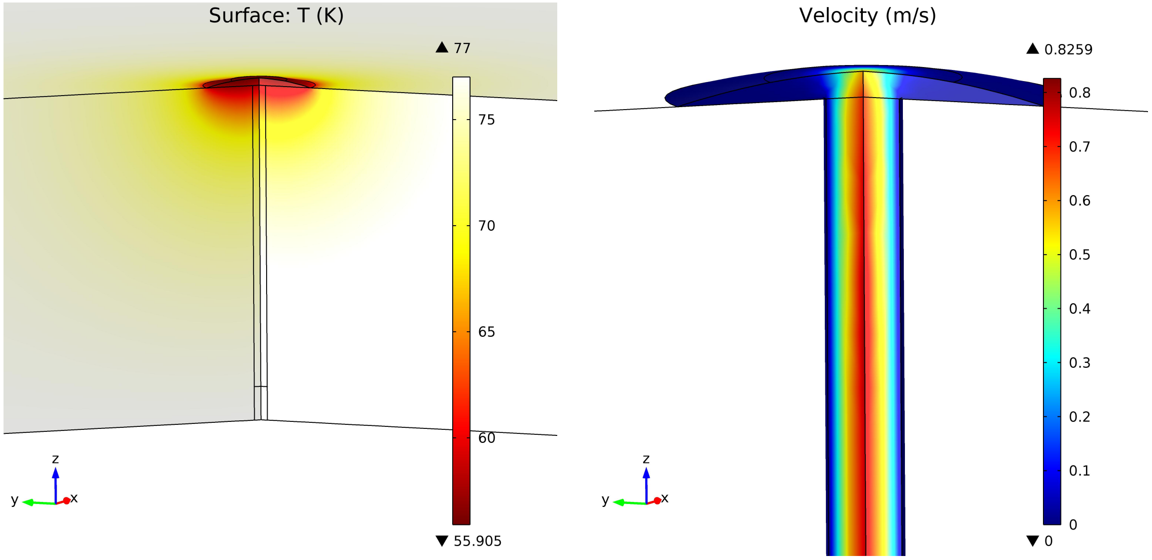

(a) Temperature profile (b) Velocity profile

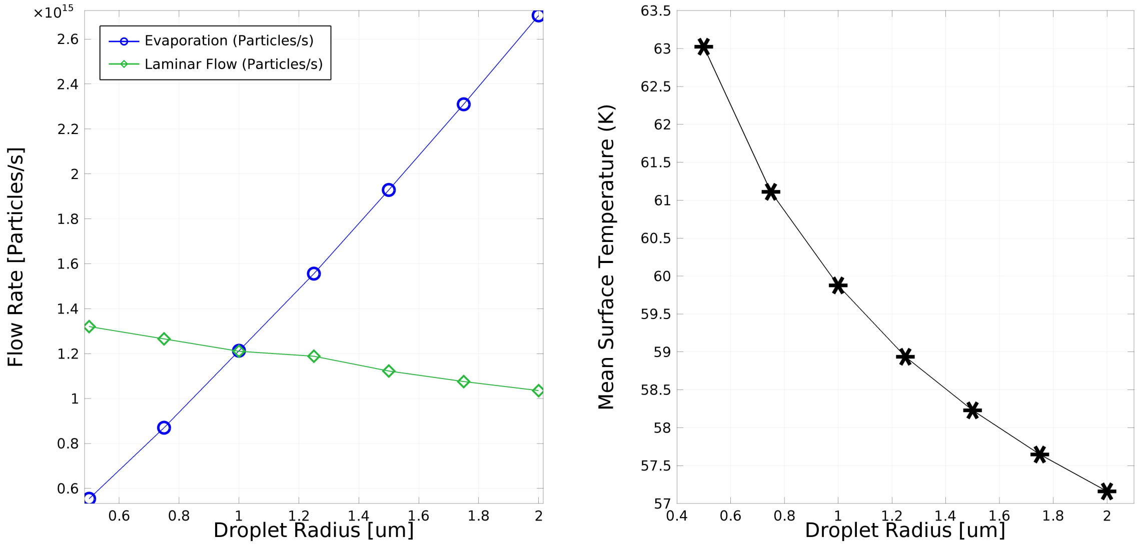

(c) The equilibrium droplet radius was at the intersection of the exit flow rate and evaporation for various drop sizes.

(d) Mean surface temperature of the drop at various radii.

Figure 3.5: COMSOL: N_2 flow at 77 K in PET nanopore. D=500 nm, L=12 μm.

COMSOL couples the solid, fluid, and radiative heat interactions in our model to reflect realistic temperature profiles based off inputted values. In the limit where surface tension dominates over gravity and the edges were far from bounding edges the droplet was modeled as a paraboloid [53]. Equation 3.8 has a contact angle of θ, radius of the droplet g, and coordinate r. The contact angle of liquid nitrogen on fused quartz was assumed to be 20 degrees. The entrance of the nanopore and membrane was in direct contact with the liquid nitrogen reservoir and assumed to be at T_R=77 K. The exit was modeled with a drop which was exposed to vacuum. A radiative heat transfer from the surrounding container was applied to the PET membrane and drop surface at the exit side. Evaporation was included by a heat flux at the surface (equation 3.6) which was proportional to the Hertz-Knudsen equation 3.7. The vapor pressure term makes the flow rates highly sensitive to temperature effects. The latent heat of vaporization for nitrogen L_{vap} is ≈200 kJ/kg. The Hertz-Knudsen equation generally overestimates the mass flow but can be used with appropriate corrections[46, 47, 45]. A temperature discontinuity across the non-equilibrium interface further complicates the correct temperature to use. For qualitative purposes the Hertz-Knudsen equation was still used as an upper limit to the mass flux and in turn an upper limit to the heat flux as well. Our model can easily incorporate a more realistic mass flux for future work. The radius g of the drop was swept to see the effects of varying sizes on temperature and flow conditions.

Results for a 500 nm nanopore calculation at a pressure drop of 1 Atm are in figure 3.5. The 500 nm nanopore was outlined at the center of the PET membrane cutaway. Figure 3.6(a) was a visual representation of the temperature profile with a droplet of radius 2 μm. The temperature at the entrance was 77 K and quickly dropped to the minimum value of ≈ 55 K near the exit. The minimum temperature was below the triple point of nitrogen 63 K where freezing is thermodynamically favorable. Figure 3.6(b) has the velocity profile inside the nanopore. A parabolic shape appears with a maximum velocity of 0.83 m/s at the center and zero at the walls. The maximum velocity deviates from theory by 2.4%. Figure 3.6(c) plots mass flow in particles/s exiting the pipe versus various radii of the droplet. The green diamonds were exiting mass flows and decrease as a function of either the radii or surface area. This was a consequence of the temperature dependent viscosity which can increased by up to a factor of 3 near the exit as the temperature drops were larger as surface areas increased. Blue circles were evaporative mass flows which increase with the surface area. Although the mean temperature of the surface falls in figure 3.6(d) which reduces the evaporating mass flux the increased surface area more than compensates. The intersection of the green and blue data predicts a 1 μm radius steady state for a pressure drop of 1 Atm. The model predicts freezing of nitrogen very near the nanopore exit at the onset of liquefaction. Increasing the pressure drop increases the steady state radius of the drop by about an order of magnitude which was still relatively close to the exit.

The results of a 10 μm and 1.8 μm diameter microtube model were shown in figure 3.6 and 3.7 respectively. A pressure drop of 1 Atm was assumed across the 1″ length. Similarly to the nanopore model the microtube model reflects conditions to the actual experiment at the onset of liquefaction. The boundary condition for half the microtube was at T_R=77 K to replicate the conditions of being inside the liquid nitrogen reservoir. The remaining half protruding into vacuum experiences a radiative heat flux from the cell walls. A liquid nitrogen drop with a parabolic profile (equation 3.8) was modeled to have a heat flux proportional to equation 3.6. Again this parabolic profile assumes an initial drop formation.

Evaporation reduces the temperature of the pipe significantly as seen in figures 3.6(a) and 3.7(a). Portions of the pipe were below the triple temperature of nitrogen and can be expected to freeze. The pressure profiles 3.6(b) and 3.7(b) were no longer linear because of the temperature gradients changing the viscosity. At D=10 μm the laminar flow exceeded any evaporation that a parabolic droplet could produce and a large drop can be expected to grow at the tip. This contrasts to a D=1.8 μm pipe where the evaporation exceeded the laminar flow at a pressure drop of 1 Atm. An internal interface was therefore predicted by COMSOL for the 1.8 micron pipe and in fact evidence of this was observed in the data (figure 3.3). At 1 Atm the data was observed to be below the theoretical laminar flow with an asymptotic approach to the line at higher pressures. The suppression can be explained by the fact that vapor pressure at the internal interface P_{int} was no longer zero but now equal to 1 Atm. The existence of the interface was necessary to explain experimental results.

The mean temperature of the droplet interface in figures 3.6(d) and 3.7(d) were below the triple point and freezing was possible. However because evaporation was suggested to be much larger than laminar flow for the 1.8 μm capillary an external interface model was no longer valid

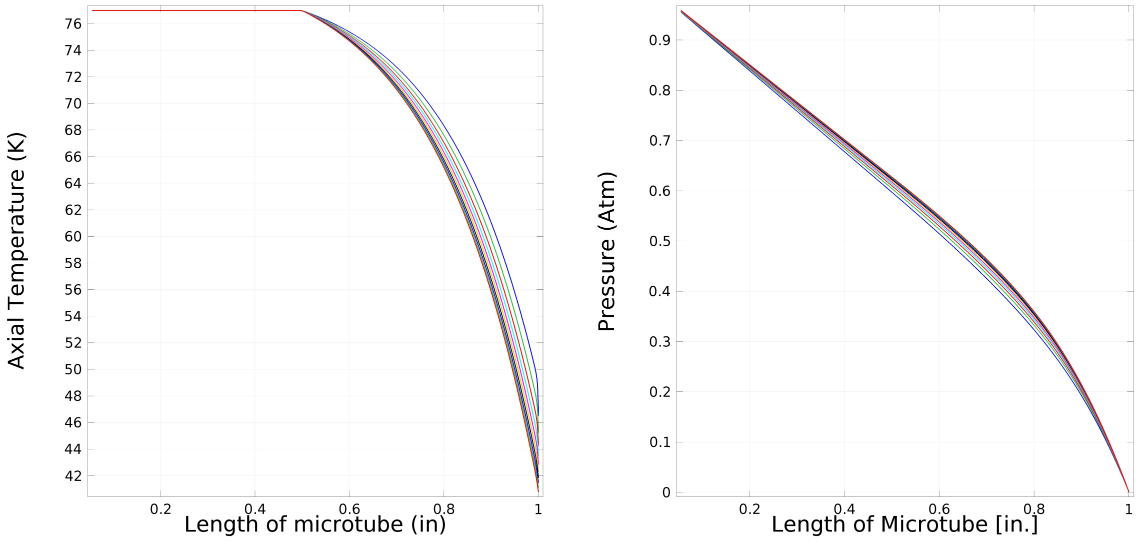

(a) The axial temperature profiles of drops with increasing surface areas shows temperatures below the triple point of nitrogen. The lowest curve was for a 40 μm drop and the highest curve was for a 130 μm drop.

(b) The axial pressure profiles of drops deviate from the expected linear fit.

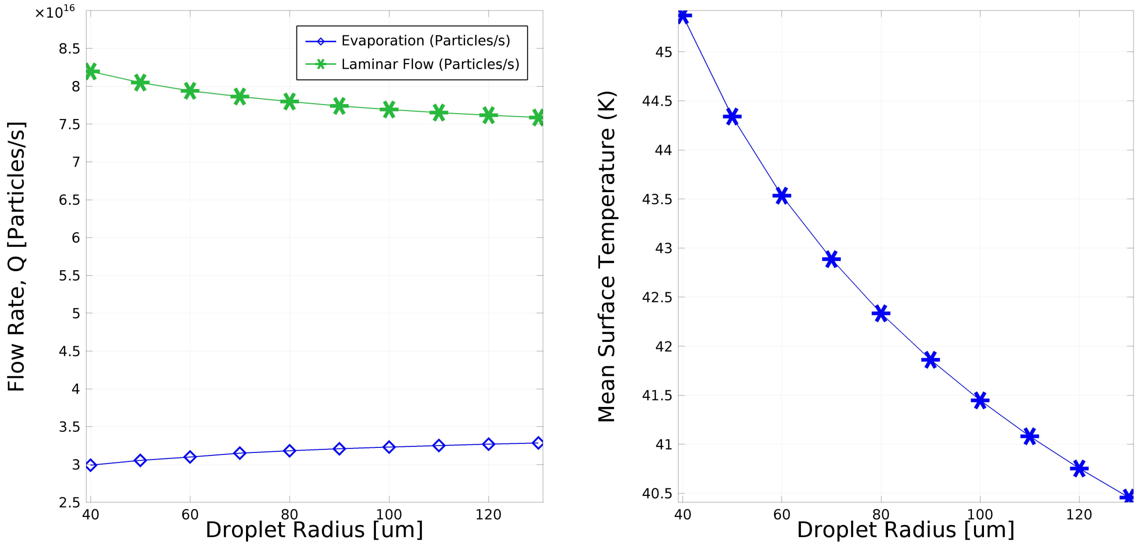

(c) No equilibrium droplet size was determined with a simple parabolic profile. A large droplet was expected to grow at the end of the capillary.

(d) Mean surface temperature of the drop at various droplet radii. The mean surface temperature were below the critical point of nitrogen ≈63 K.

Figure 3.6: COMSOL: N_2 flow at 77 K in glass capillary. D=10 μm,L= 1 in.

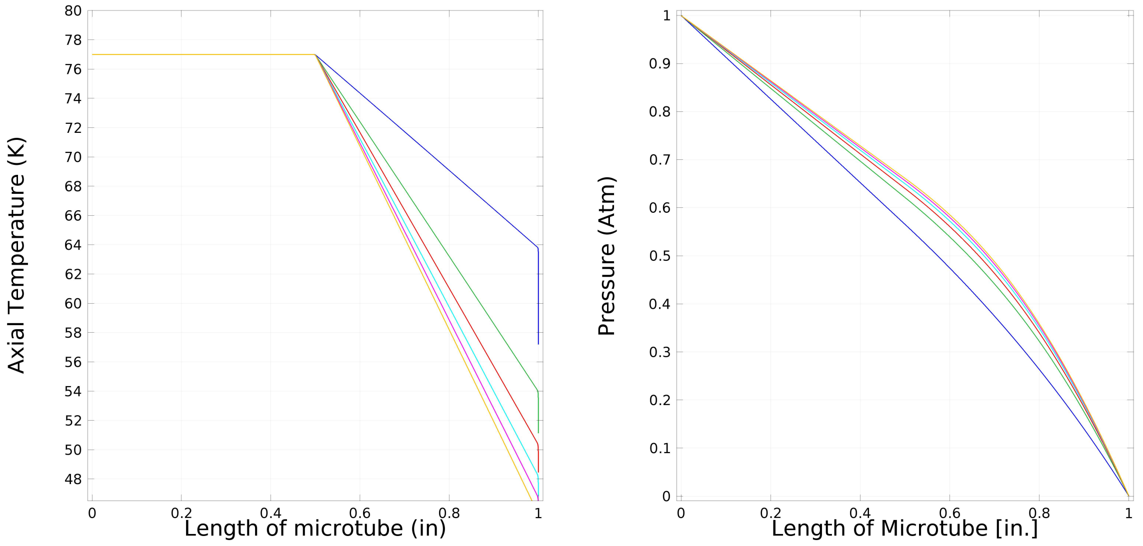

(a) The axial temperature profiles shows temperatures below the triple point of nitrogen near the exit. The top line corresponds to a 1 μm radius drop and the bottom line was a 11 μm radius drop.

(b) The axial pressure profiles deviates from the expected linear fit due to temperature gradients.

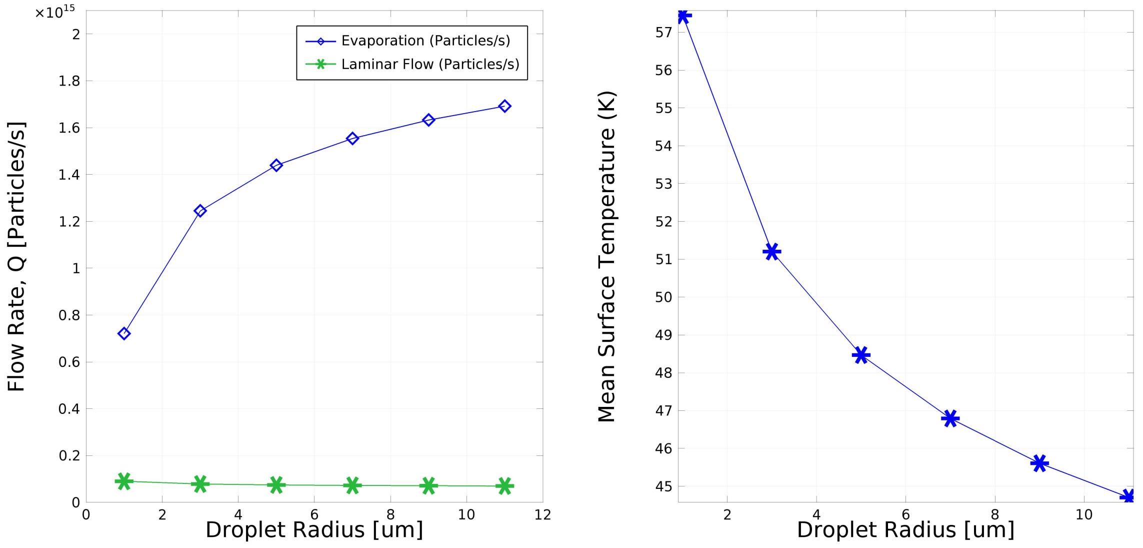

(c) Evaporation was larger than the laminar flow. An internal interface was expected.

(d) Mean surface temperature of the droplet at various radii. The mean surface temperature were below the critical point of nitrogen ≈63 K.

Figure 3.7: COMSOL: N_2 flow at 77 K in glass capillary. D=1.8 μm, L=1 in.

and a new model should be suggested for internal interfaces. An assumption we made which was supported by liquid helium data suggests that the internal interface experiences no heat flux and was in thermal equilibrium with the liquid reservoir.

A qualitative argument can be devised based on the models in COMSOL as to answer the questions why freezing was very likely to occur in nanopore studies while freezing in microtubes was much less likely. For small microtubes of large aspect ratio an internal interface would most likely not significantly alter the temperature profile. For larger microtubes the higher flow rates would result in large drops growing at the tips of the capillary. Although the surface temperature was below the critical point the distance from the exit could lower the probability that a nucleation event would occur near the pipe's exit and cause clogging. In contrast to the microtube model small, equilibrated drops were predicted with the nanopores. A nucleation event in the smaller drop would be more likely to clog the the pore. Although these results and inferences were based on an evaporation flux which was much higher than reality, the models helped with a qualitative understanding of non-isothermal laminar flows. With the proper mass flux equation a refinement to the model is possible.

3.5 Flow of Water

The optical cell described in section 3.2 was designed to further investigate freezing in micro flows. Water was used instead of nitrogen for two reasons. The first was overcoming the experimental challenge of observing a micron scale interface within a cryostat. The second was the importance of water in all living systems and its application to a variety of industrial applications. The thermophysical properties of liquid nitrogen and water differ sufficiently as to prevent direct comparisons. For example the latent heats and vapor pressures at 320 K and 77 K for water and nitrogen both differ by an order of magnitude from each other. Although being thermodynamically distinct the hope was to observe the interface and better understand the onset of freezing. A 10 μm diameter, $5''$, fused quartz capillary was used for all optical experiments. To save computing power a $1''$ of same diameter was modeled in COMSOL. The pressure drop was reduced by 80% to mimic the flow rates in the actual 5″ pipe.

3.5.1 Microscope Images

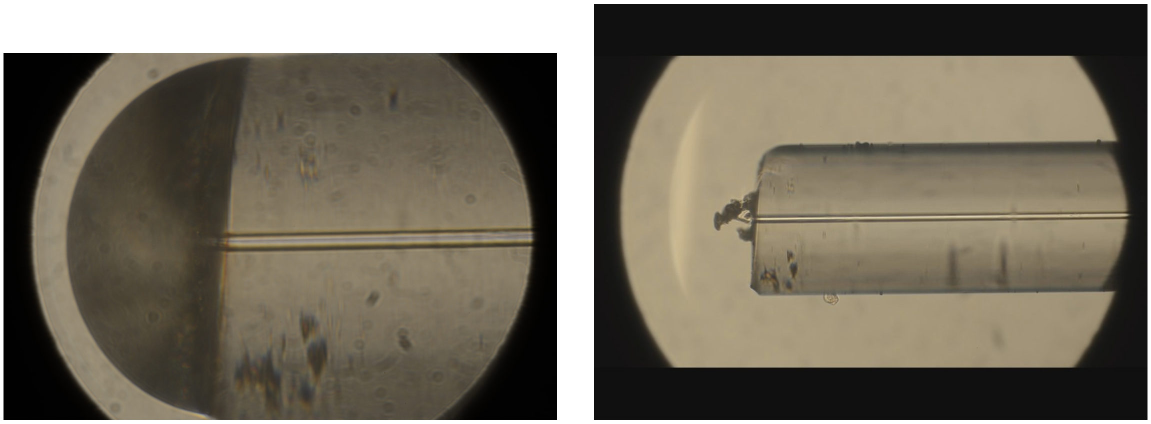

(a) Water drop at the end of a 10 μm diameter and 5 in. long glass capillary at T=320 K. The pressure drop was 1.2 Atm.

(b) Same capillary and temperature as part a. A pressure drop of 17 Atm caused a cyclic freezing, melting, and flow at a time scale of a few milliseconds.

Figure 3.8: Water images: small and large pressure drop.

Through observation the behavior of water flow into vacuum was divided into two states at high and low pressure drops. Figure 3.8(a) shows one state existing as a liquid at a constant pressure drop of 1.2 Atm. The 10 μm microtube can be seen within the capillary. The outer diameter of the fused quartz was 353 μm. The drop grew unhindered and remained in a liquid state at periods up to ≈ 20 minutes before the size would cause it to crawl to the sides of the capillary. Water can exist in a metastable supercooled state down to ≈ 15 K [54]. This implied the temperature of our drop to be on the order of -15 K or higher to maintain its supercooled state. Although the liquid was in a supercooled state a variety of externally induced mechanical vibrations would not induce the nucleation of ice.

An instability was observed for pressure drops greater than ≈ 3 Atm. Figure 3.9 replaces a well defined liquid droplet with a smaller drop fluctuating in time. Water appeared to cyclically alternate between a liquid entering vacuum (figure 3.9(a)), subsequent freezing (figure 3.9(b)),

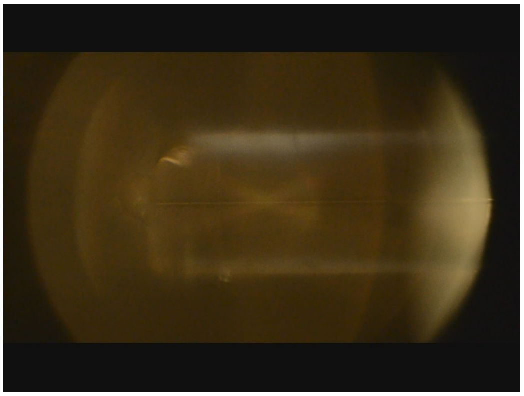

(a) Cross polarized image of water flow into vacuum. The capillary end was imaged. D=10 μm and L=5 in.

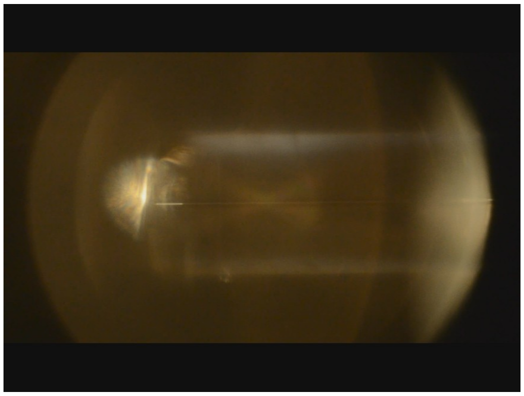

(b) The white colorations near the center of the image was the formation of ice on the exterior. The ice then melts in a time scale of a few milliseconds and the process was cyclic.

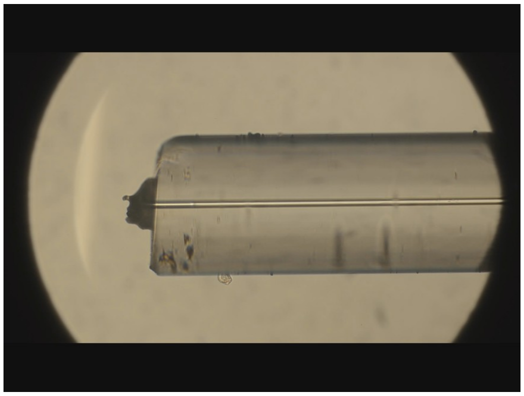

(c) Polarizers removed and the sublimating ice was shown. The 10 μm diameter microtube can now be observed clearly along the axis. The outer diameter of the capillary was 353 μm.

Figure 3.9: Water 320 K: capillary freezing at a pressure drop of 17 Atm

sublimation of the frozen plug, and finally liquid flow again. This cycle occurred on the order of a milliseconds. Freezing was confirmed experimentally by placing the cell between two orthogonal, linear polarizers and setting the transmission of the polarized light to zero. The nucleation of ice shifted the polarization of the light which produced a finite transmission. Flashes of white light would indicate ice nucleating as seen in figure 3.9(b). Without the polarizers ice could be inferred by the disappearance of the water drop and appearance of small fluctuations in water structure near the exit. The instability onset occurred always at ≈ 3 Atm regardless of the direction in pressure. The source of the instability is still unknown but the thermal Peclet number (Pe=$\frac{DU\rho c_p}{\kappa}$) informs us that vaporization was not occurring because of a superheated liquid rapidly entering vacuum. This process is called flash vaporization. The temperature of the external drop appears to be a function of the pressure drop as higher flow rates create the onset of ice formation. The instability dependence on reservoir temperature could not be studied as the pumping system was not strong enough to remove all water vapor before condensation at higher vapor pressures.

3.5.2 COMSOL results for water flow

Although experimental mass flow measurements were inconclusive an analysis using the mass flux equation 3.7 was still attempted. The temperature dependent properties of water was uploaded from the material library of COMSOL. The COMSOL results of D=10 μm, glass capillaries in figure 3.10 were for pressure drops equivalent to 1 Atm and 3 Atm across a 5 in. pipe. Steady state drops were predicted with diameters of 12 micron and 43 micron for pressure drops of 1 Atm and 3 Atm respectively. These results severely underestimate the actual drop if compared to figure 3.8(a). The image does not show a steady state because after about 20 minutes the drop would move to the side of the capillary walls and continue growing. The severe underestimation was because of the overestimated evaporation rate in equation 3.7. Modifications to the Hertz-Knudsen equation have been proposed by [46, 45, 47]. A suggested improvement can be made by defining a pseudo temperature equivalent to the kinetic energies of the outgoing gas in equation 2 of reference [47]. McGaughney et al. applied the statistical rate theory (equations 11-15) which

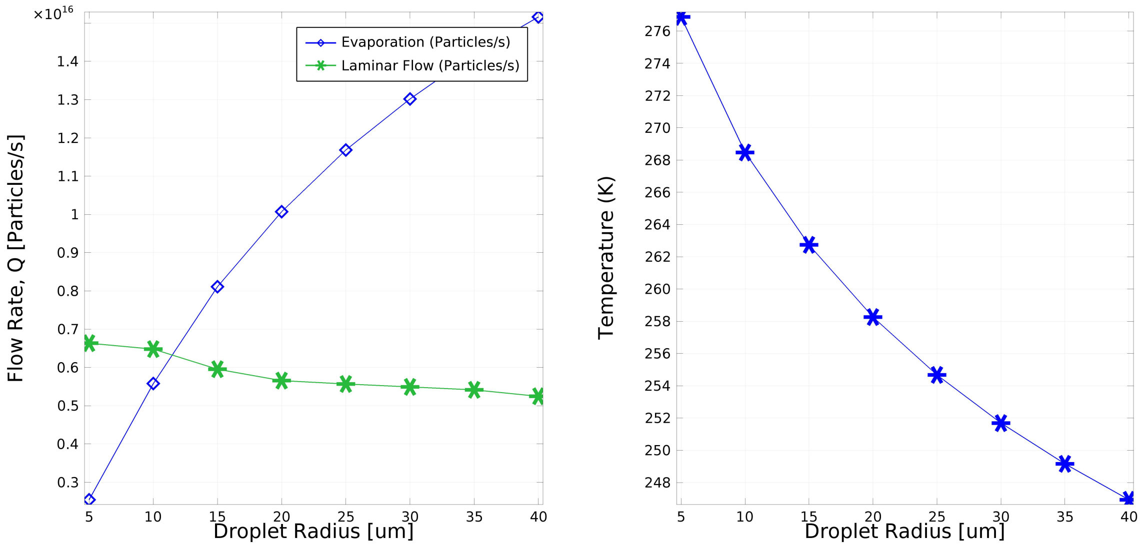

(a) Modeling an equivalent pressure drop of 1 Atm the steady state radius of the drop was ≈ 12 μm. The capillary diameter was 10 microns.

(b) Mean surface temperature of various drops with a flow rate corresponding to a pressure drop of 1 Atm. At steady state a temperature of 262 K was predicted.

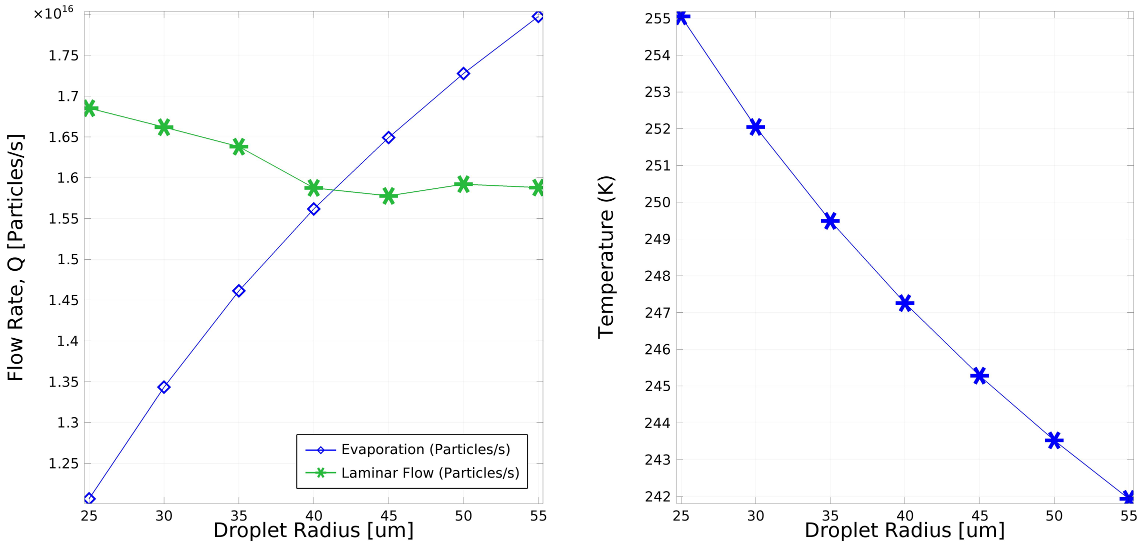

(c) Modeling an equivalent pressure drop of 3 Atm the steady state radius of the drop was ≈ 43 μm.

(d) Mean surface temperature of various drops with a flow rate corresponding to a pressure drop of 3 Atm.. At steady state a temperature of 246 K is predicted.

Figure 3.10: COMSOL: 10 micron water flow at 320 K

has corrections to equation 3.7 by the inclusion of the molecular vibrational temperature. With an overestimate of the mass flux the temperatures of the surface in figures 3.10(b) and 3.10(d) were also an overestimate and should be looked for qualitative trends only. With the appropriate equation and spherical profile shape for larger drops our model can be easily improved to provide better quantitative values.

3.6 Flow of Normal Helium-4

3.6.1 Liquid helium-4 data

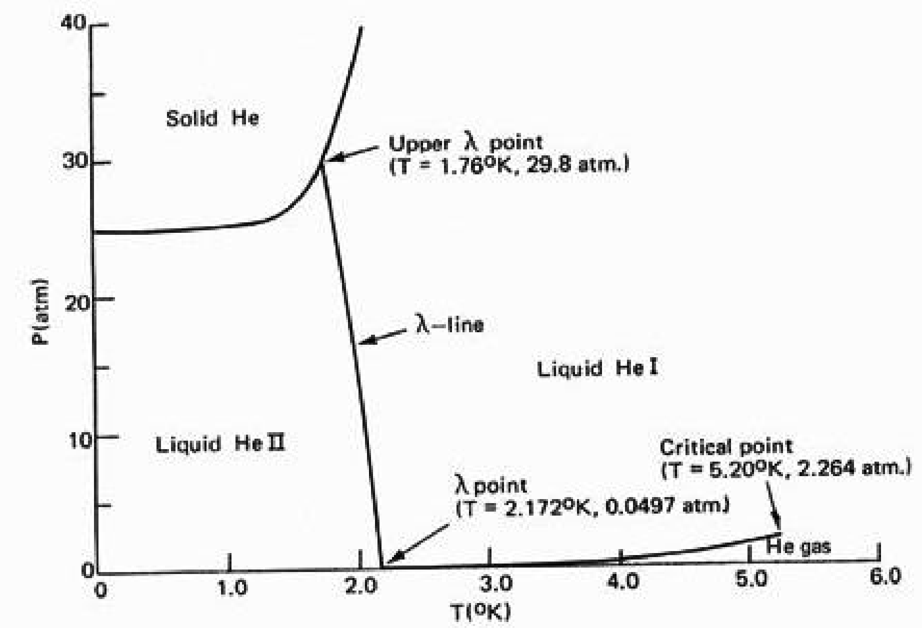

Figure 3.11: Phase diagram of helium-4. [55]

The unique phase diagram of ^4He offers a liquid without the problem of freezing in vacuum. The normal triple point is substituted by a normal liquid, superfluid, and gas triple point. In figure 3.11 the second triple point where solidification occurs is at a pressure of 29.8 Atm. As long as ^4He is maintained at a temperature greater than the lambda point T_λ=2.17 K then a viscous liquid is present. The lambda point is named by the shape of the specific heat of helium-4 as it transitions through it. A superfluid is characterized by a very large thermal conductance and zero viscosity. In contrast to the nitrogen data, helium provides an ultra pure liquid without the chance of freezing by evaporative cooling. Nanopores with large aspect ratios were etched specifically to force an internal interface where a two phase, liquid/vapor flow can occur. By equating the vapor equation 3.2 and liquid equation 3.3 the location of the internal interface x_L was predicted.

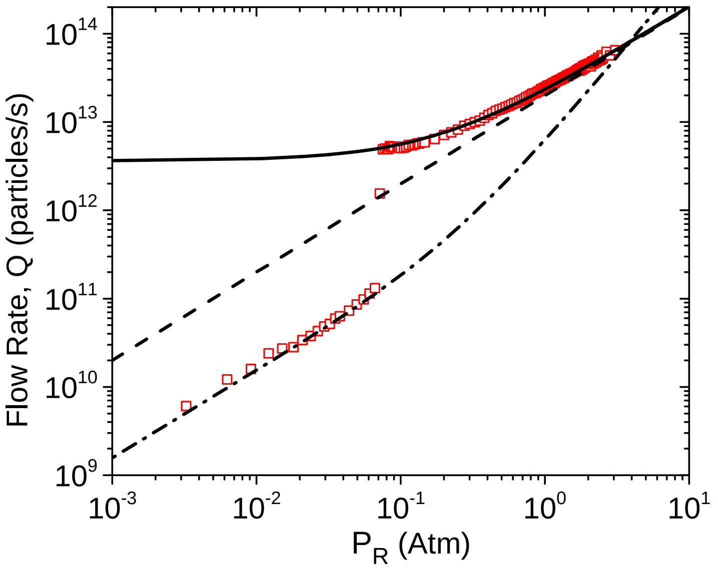

Figure 3.12: Normal helium in 60 nm diameter PET membrane at 2.3 K. The solid line was equation 3.3 with L=12 μm, λ_s=0, and P_{int}=0. The internal liquid/vapor interface was evident by the flat pressure independent regime. The discontinuous step was the onset of liquefaction at the saturated vapor pressure. The dash line equation 3.3 with λ_s=0 or in other words a normal, macroscopic, laminar flow. The dash dotted line was the vapor equation 3.2 with x_L=0 [29].

^4He flow data for a single 60 nm PET nanopore in figure 3.12 shows no sign of reduced flow as in nitrogen. The dash dotted line was the vapor equation 3.2 with x_L=0, L=12 μm, and a perfectly diffuse surface. The dash line was equation 3.3 with no slip (λ_s=0)and the absence of a liquid/vapor interface (P_{int}=0, $\gamma = 0$). This was the laminar flow for a liquid which scales linearly in pressure. The solid line was a liquid flow with a liquid/vapor interface. The curved interface provides a pressure independent flow with a surface tension value of 0.277(mN/m). The data shows the vapor flow followed by an interfacial liquid flow. The discontinuous step representing the liquefaction of the vapor. The interface position can be inferred to be very near the exit of the nanopore. Just as nitrogen transitioned to a supercooled state as it neared the exit so helium can also pass through its lambda point near the exit. This would become a normal/superfluid two phase flow. There was no strong evidence in the data that would lead to the conclusion that although the superfluid had been present that it had any appreciable effects.

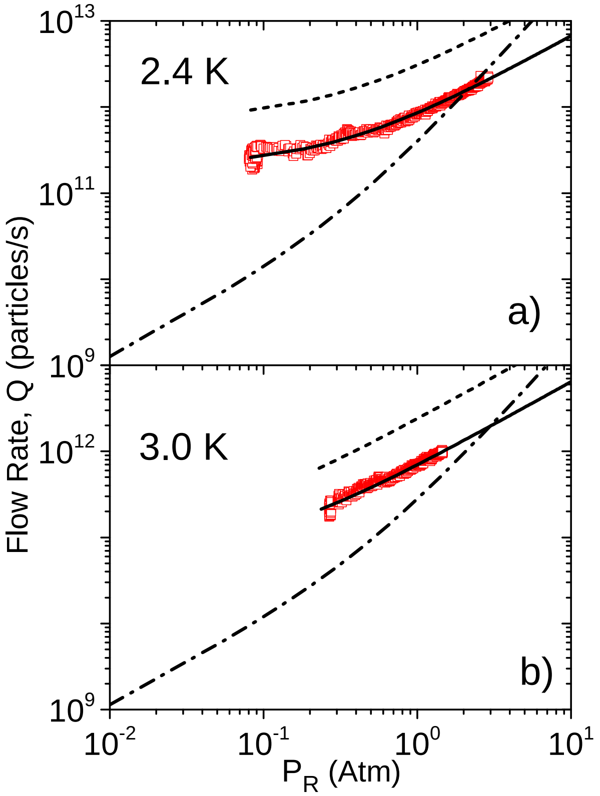

Figure 3.13: Flowrate Q of helium-4 through a mica pore with D=31 nm and L=20 microns as a function of pressure at the inlet P_R. Dashed dotted curves are from equation 3.2 assuming the pipe was full of gas. Solid curves were the predictions of the two phase model assuming slip length λ=0. Dotted curves were from equation 3.3 and 3.4 assuming λ=10 nm. (a) T=2.4 K. x_L ranges from 19.6 μm at the saturated vapor pressure of 0.08 Atm to 19.9 μm at 2 Atm, i.e., the pipe was almost completely filled with liquid for all values of the applied pressure, but the existence of an internal meniscus was required to explain the upward curvature. (b) T=3.0 K x_L ranges from 17 μm at the saturated vapor pressure to 19.4 μm at 2 Atm. From reference [29].

The effects of an internal interface can inverted to be resistive when the temperature approaches the critical point. As T_R was increased the vapor pressure increased exponentially and the Laplace

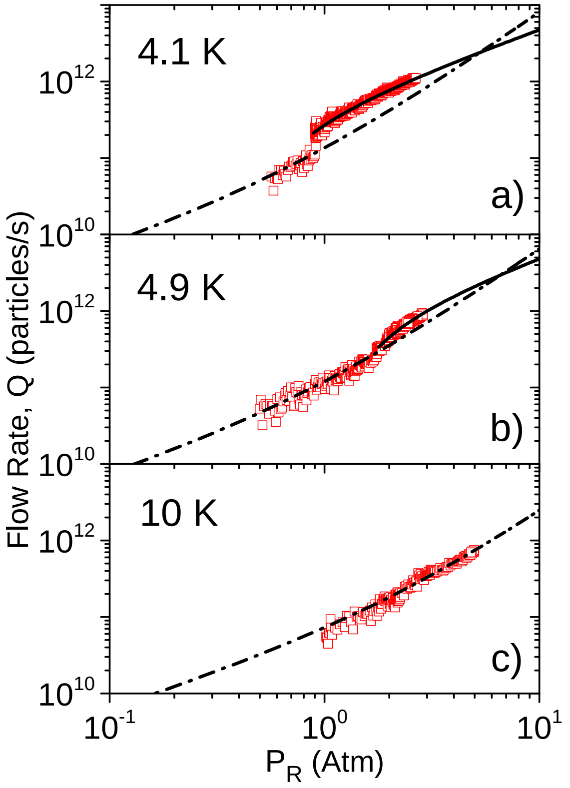

Figure 3.14: Flow rate Q of helium-4 through a mica pore with diameter=31 nm and length=20 μm as a function of pressure at the inlet P_{int}. The dashed-dotted line are from equation 3.2 assuming the pipe is full of vapor, and the solid curve is the prediction of the two phase flow model with zero slip length. In (a) and (b), the pipe partially fills with liquid at the saturated vapor pressure. (a) T=4.1 K. x_L ranges from 11 μm at the saturated vapor pressure to 18.2 μm at the maximum pressure of 2.6 Atm. (b) T=4.9 K. x_L ranges from 3.15 μm at the saturated vapor pressure to 14.5 μm at the maximum pressure of 2.45 Atm. (c) T=10 K. Since the temperature is above the critical temperature, there is no two phase interface [29].

pressure decreased to zero at the critical temperature. The vapor pressure at the interface was a resistive pressure reducing the flow rates more as T_R was increased. The black solid line in figures 3.13 and 3.14 model the two phase flow for a 31 nm diameter, 20 micron long mica nanopore. In figure 3.13a the Laplace pressure increased the flow and the rate was independent of pressure P_R. Figure 3.13b the Laplace pressure and vapor pressure at the interface P_{int} cancel each other and linear pressure dependence on P_R was observed. The dash dotted line were from equation 3.2 assuming the pipe was full of gas. As the dimensions approached the atomic scale slip effects become more evident. The dashed line assumed a slip of 10 nm and the sensitivity of our system was high enough to measure the presence of nanometer slip lengths.

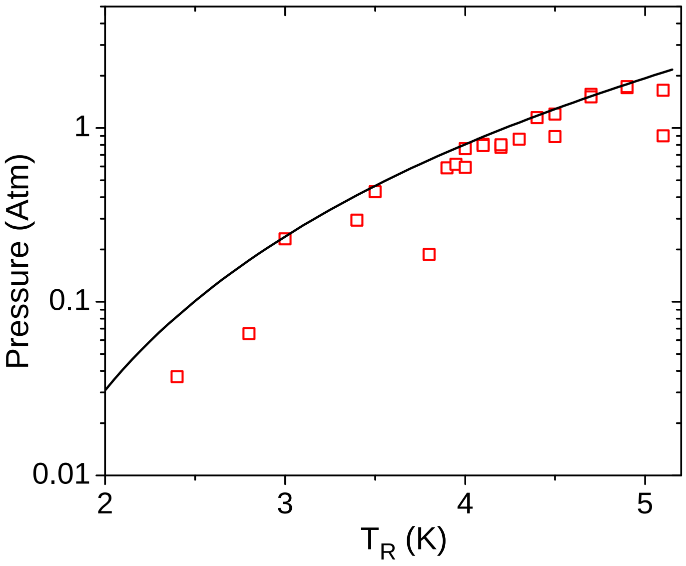

Figure 3.15: Plot of interface pressure P_{int} as function of reservoir temperature T_R for helium in a 31 nm diameter pipe. P_{int} was determined by a self consistent solution of equations 3.2, 3.3, and 3.4. The solid curve was the bulk vapor pressure of ^4He. From reference [29].

As the temperature approached the critical temperature 5.2 K the higher vapor pressures at the meniscus resists the flow to a greater degree. Figure 3.14 shows successively the suppression of the flow as the temperature was raised. The position x_L of the meniscus was expected to not be static but instead be a function of the inlet pressure P_R. Higher P_{int} corresponds to smaller x_L and will increase as a function of inlet pressure. At temperatures greater than the critical point there was no distinction between the liquid and vapor phase. The two phase flow was replaced by a purely vapor flow. The measured vapor pressure was plotted in figure 3.15 with the bulk vapor pressure of ^4He. By the self consistent solution of equations 3.2, 3.3, and 3.4 a simple, no-slip model accurately described a two phase flow in nanopores of large aspect ratios. The position of the meniscus x_L can also be predicted and expected to be a function of the inlet pressure.

3.6.2 Nanotube Flow Instability

$$Q = \rho_N \pi R^2 \sqrt{\frac{R\Delta P}{2\kappa^2 \rho L}} Ln[\frac{R}{d}] \tag{3.9}$$

$$Q = C_1 \rho_N \pi R^2 \sqrt{\frac{2\Delta P}{\rho}} \tag{3.10}$$

An interesting feature appeared with a larger PET nanopore of 441 nm diameter. The laminar flow state was unstable and transitioned to a flow with a $P_R^{1/2}$ dependance in figure 3.16. In certain runs at 3.5 K and 4.4 K the $P_R^{1/2}$ occurred immediately at liquefaction. Although we cannot yet fully explain its origin we present two possible models which have the correct pressure dependance. Similar to the turbulent vapor flow the instability could be a laminar-turbulent transition. The turbulent equation for a liquid in 3.9 had a square root pressure dependance for an incompressible fluid. However the Reynolds number between 250-400 was noticeably lower than the empirical value of 2000 for normal turbulent transitions. The surface profile of a PET nanopore could have large protrusions and expansions along the length of the pore. With the Reynolds number scaling as R^3 a sudden widening in the nanopore could have potentially increased the Reynolds number beyond 2000. The relative surface roughness of 30% was a better fit than the value of 10% which fit well with the turbulent gas data in figure 2.13.

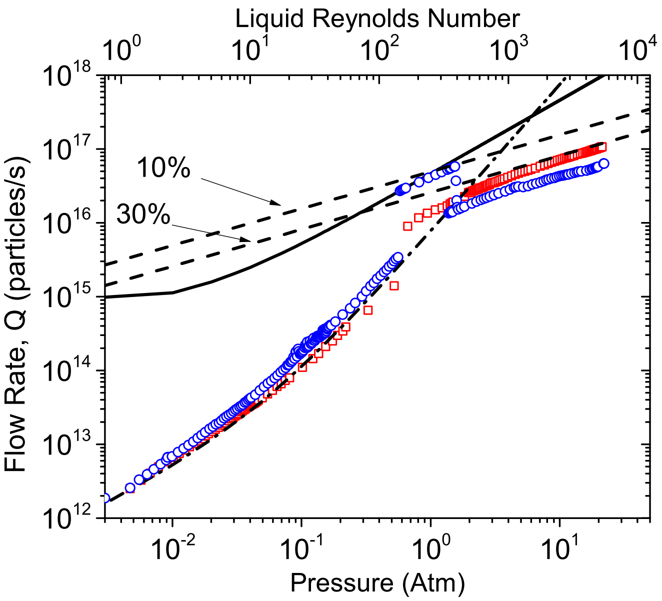

(a) T=3.5 K. The solid line was a two phase flow with P_{int}=0. The dash-dotted line was for a gas flow and the dash lines were the turbulent equation 3.9 with a relative surface roughness of 10% and 30%. The blue circle data saw a transition from a laminar to a flow with $P^{1/2}$ dependance. The laminar flow appeared to be unstable and transition to the more stable $P^{1/2}$ state. Although the turbulent model with a 30% surface roughness models the data well this was in contrast with the gaseous turbulent data in figure 2.13 with a surface roughness of 10%. The Reynolds number of the liquid was placed along the top axes and the transition occurred at 250 and 400. The transition to a turbulent flow typically occurred with a minimum Reynolds number of ≈ 2000.

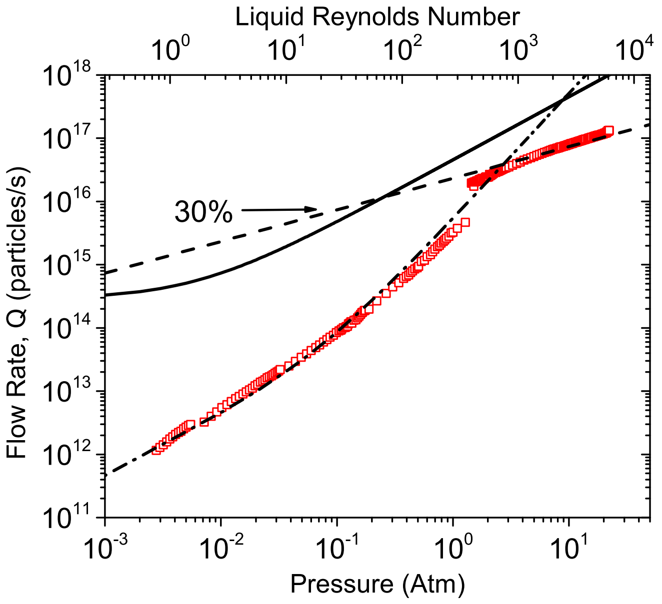

(b) T=4.4 K. The Reynolds number of the liquid was along the top axis and the transition occurred at Re=350.

Figure 3.16: Flow instability in a nanotube

The aspect ratio for a 441 nm diameter nanopore was ≈ 27. The validity of equation 3.1 only is applicable for long, thin pipes. For short pipes and orifices Bernoulli's equation 3.10 with a constant C_1 which takes into account dissipative effects could be a candidate to model the flows in figure 3.16. The mechanism which would cause a transition between a high aspect ratio flow to a small aspect ratio appears at first glance to be unlikely as this would imply a new physical effect becoming dominant. To understand this phenomena better, data for short nanopores and further runs at various temperatures near and far from the critical temperature are needed. Similar to helium gas, liquid helium offers benefits as a fluid to study turbulence in nanotubes.

3.7 Conclusion

The area of two phase flow in nanotubes is rich in phenomena which needs to be further explored. We have made much progress with liquid helium as the problem of freezing was eliminated. A prediction of the internal interface was made which intuitively shows the interface moving closer to the exit as the pressure increased. The internal interface could even be probed by measuring the reduction of the flow rates. Surface tension and vapor pressure values next to the interface can be measured accurately and were provided in the chapter as well. By our method a measurement of the surface tension in smaller nanotubes is now possible. As the atomic length scales are approached it would be interesting to measure any discrepancy in the surface tension from size effects.

Experimentally water and nitrogen were more challenging than helium and needs further attention. The nature of freezing appeared to be dependent on the flow conditions, material, and dimensions of the tube. COMSOL simulations were helpful for qualitative ideas however an improvement on the correct evaporation rate would provide the quantitative results to reflect more our experimental observations. A modification to the water cell was also needed to have better control of the temperature in our system. The glass micropipe has a poor thermal conductance and an evaporating droplet at its end creates a significant temperature gradient. Coating the outer glass with highly conductive material or thermally sinking it to a copper piece should create a uniform temperature profile. The constant temperature may eliminate the flow dependent freezing that was observed.

Carbon nanotubes are on the order of 2 nm in diameter and millimeters in length. To measure the slip with a single nanotube would be the ultimate goal for our two phase research. The effects of the hydrophobic and atomically smooth surfaces on the flow of water, nitrogen, and helium can reveal many interesting phenomena. The interfacial boundaries and surface tensions can also be measured to observe deviations from the bulk values and reveal size effects.

Chapter 4

Superfluid Flow

4.1 Two-Fluid Model

	Mass Flow, Q	Velocity, v	Dissipation	Model
Normal	$\frac{\pi R^4 \rho \Delta P}{8\eta L}$	$\frac{R^2}{8\eta L}\Delta P$	viscous	Navier-Stokes
Superfluid (Critical)	$\pi R^2(\rho_s \mathrm{v}_{sc} + \rho_n \mathrm{v}_n)$	≈ 60 m/s	roton	Landau
		$\frac{\hbar}{m_{He4}R}(ln[\frac{8R}{a_0}] - \frac{7}{4})$	vortex ring	Feynman
		$\frac{\hbar}{m_{He4}2R}ln[\frac{2R}{a_0}]$	rectilinear vortex	Feynman
		$\propto -\frac{\rho_s}{\rho T ln[\frac{\Delta P}{\rho}]}$	vortex ring	ILF
		$\mathrm{v}_{co}(1 - \frac{T}{T_0})$	$\mathrm{E}_a \propto \mathrm{T}$	ILF

Table 4.1: Number flow rate Q for a viscous and superfluid

Liquid helium transitions to a new state below the lambda temperature T_λ=2.17 K. Landau described superfluid ^4He with the two fluid model which treated liquid helium as a superposition of a viscous fluid and a fluid with quantum mechanical effects on a macroscopic scale [25]. With a two fluid description the total mass density and mass flux were described to first order by a linear combination of the normal and superfluid state with equations 4.1 and 4.2 respectively. The total density ρ is fairly constant at 145 kg/m^3 while the superfluid ρ_s and the normal ρ_n densities are highly dependent on temperature as shown in figure 4.1. The normal density becomes negligible below 1 K but only reaches zero at T=0 K.

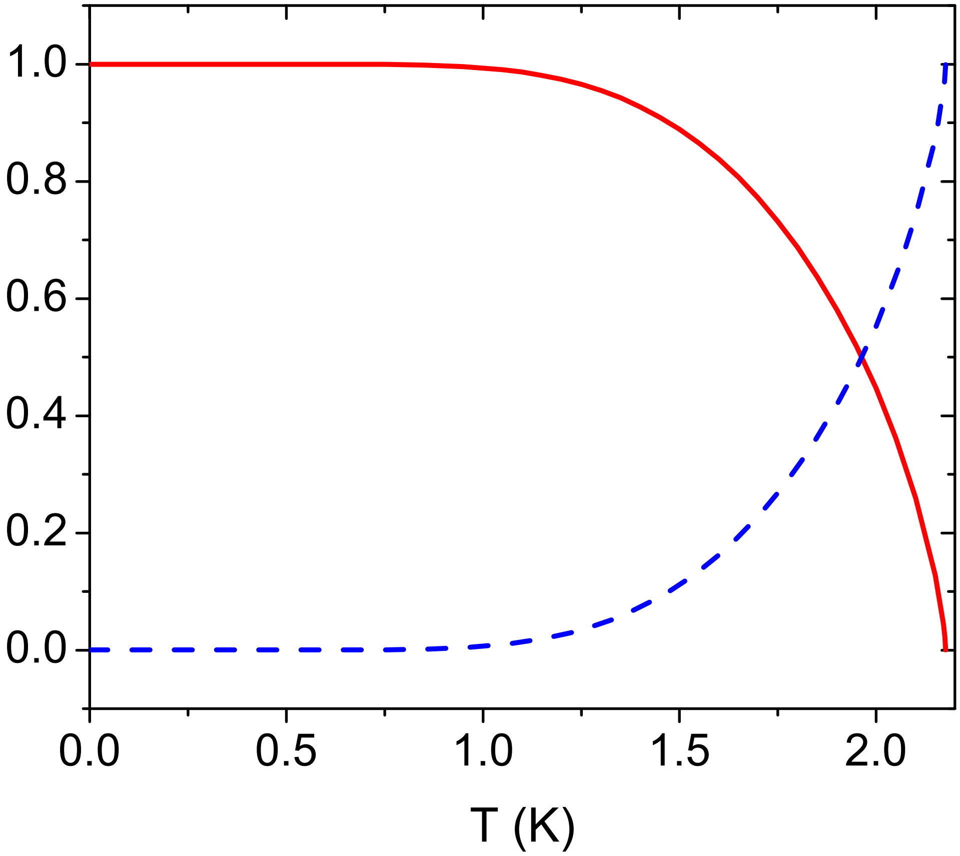

Figure 4.1: The superfluid ρ_s/ρ and normal ρ_n/ρ normalized densities of liquid helium as a function of temperature were plotted in solid red and dashed blue lines respectively[56]. The total density ρ is at a fairly constant value 145.128 kg/m^3 from T=0 K to the lambda temperature T_λ=2.17 K. The normal fraction is zero only at T=0 K while the superfluid fraction is zero at temperatures greater than T_λ. The sum of the components must equal the total density as in equation 4.1.

$$\rho = \rho_n + \rho_s \tag{4.1}$$

$$J = \rho_n \mathrm{v}_n + \rho_s \mathrm{v}_s \tag{4.2}$$

$$\mathrm{v}_n = \frac{-1}{8\eta}\frac{\Delta P}{L}R^2 \tag{4.3}$$

The total mass flux to first order is a superposition of the superfluid and normal mass flux. The normal velocity component v_n is the solution to the Navier-Stokes equation 1.4 for a laminar, viscous flow in a pipe. For velocities below a critical velocity the dynamics of a superfluid are described by the equation 4.5 for an inviscid fluid. Although similar in structure to the classical Euler equation the pressure gradient is replaced with a chemical potential gradient $\nabla\mu$ as the driving force. This new driving source becomes the source for many of the new quantum mechanical effects in helium such as the fountain effect.

$$\frac{\partial \vec{\mathrm{v}}_s}{\partial t} + (\vec{\mathrm{v}}_s \cdot \vec{\nabla})\vec{\mathrm{v}}_s = \frac{-\nabla P}{\rho} + s\nabla T = -\nabla\mu \tag{4.4}$$

$$\frac{\hbar}{m_{He4}}\nabla\varphi = \vec{\mathrm{v}}_s \tag{4.5}$$

A superfluid is a macroscopic example of a quantum mechanical system. As such a complex wavefunction Ψ describes all parameters relevant to the system. The modulus squared is the superfluid density $|\Psi^2|=\rho_s$ and the phase φ of the wavefunction is the order parameter. The gradient of the phase is proportional to v_s [57]. This restricts the superfluid to an irrotational fluid where the circulation is quantized around cores where the wavefunction is excluded. Linear quantized vortices are postulated to have cores with a radius a_0 on the order of the coherence length $a_0 \approx 0.3$ nm and a radial velocity which falls off inversely to the radial distance. The existence of quantized vortices introduces many new phenomena into superfluid dynamics. A few examples include providing a mechanism to dissipate energy, the interaction between many vortices leading to quantum turbulence, recombination events, a method for measurement of the phases, and the quantization of the angular momentum in superfluid systems with sufficient sensitivity to measure the rotation of the earth[58]. Although the effects are widely observed in superfluid dynamics the structures and interactions of the vortex cores are still not fully understood. Fortunately because the cores are much smaller in comparison to the radius R_v of a vortex ring($a_0 < R_v$) they can to first order be ignored.

$$\Gamma = \oint \vec{v}_s \, \mathbf{dl} = \frac{\hbar}{m_{He4}} \oint \nabla\varphi \, \mathbf{dl} = \frac{\hbar}{m_{He4}} 2\pi n = \kappa n \tag{4.6}$$

4.1.1 Extrinsic $\mathbf{v}_{sc}$

The inviscid state of a superfluid is valid up to a critical velocity v_{sc}. Landau predicted at the critical velocity of $v_{sc} \approx 60$ m/s the roton excitations generated in ^4He would be sufficient to destroy superfluidity and restore it to its normal state. Experimentally v_{sc} is typically found to be much lower than Landau's predicted velocity. A new excitation was postulated by Onsager and Feynman through the existence of quantized vortices within an irrotational superfluid [32]. Feynman further attempted to explain critical velocities through the formation of these quantized vortices in the flow[59]. By equating the kinetic energy of the fluid at the exit to the energy dissipated by the excitation of quantized vortices at a specific rate, Feynman predicted a steady state velocity. The Feynman critical velocity v_{sc} is dependent on the structure of the vortex where v_{sc} for either a ring or rectilinear vortex are shown in equations 4.7 and 4.8 respectively. The velocity increases as a function of decreasing pipe radius R and is temperature independent except very near T_λ where the vortex core parameter a_0 diverges. The vortex core parameter is related to the coherence length of the superfluid which also diverges at T_λ but is fairly constant far from T_λ. Feynman's critical velocity predictions better represent experimental data than Landau's critical velocity but only for orifices of radius R greater than 1 micron [60, 61, 62, 63]. The size and temperature dependence are robust but the absolute velocities can vary stochastically between different research groups and

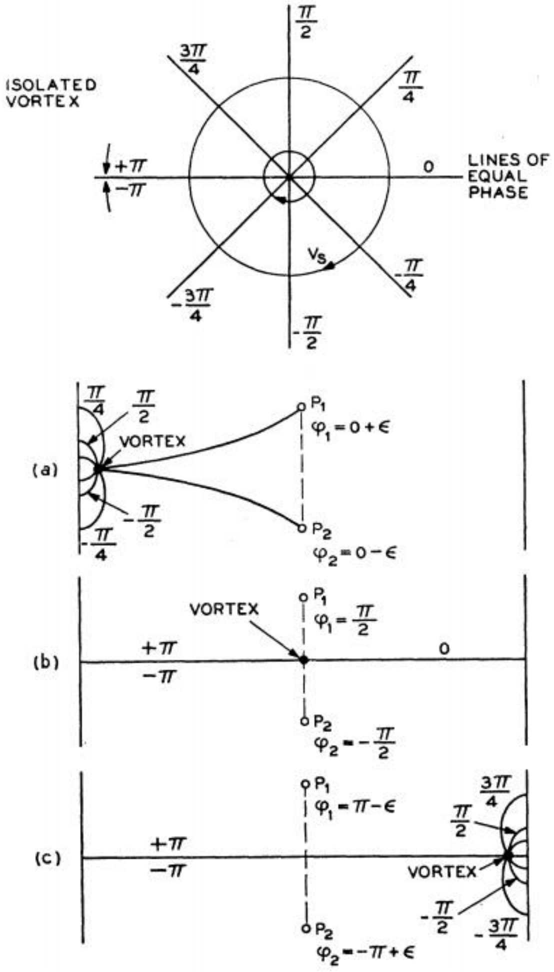

Figure 4.2: An illustration of a 2π phase slip proposed by Anderson taken from reference [57] figure 1. Lines of equal phase extend radially from a vortex line. The measured phase difference $\Delta\varphi$ between two points P_1 and P_2 will change by 2π as the vortex moves between them. The global superfluid velocity moves upward in the direction of increasing phase. The vortex will move from a to b to c as it moves from one boundary to the other.

in some cases even between experimental runs on the same orifice. The discrepancy between data and theory stems from the nucleation mechanism which Feynman's theory does not give insight to.

$$\mathrm{v}_{sc-ring} = \frac{\hbar}{m_{He4}R}(ln[\frac{8R}{a_0}] - \frac{7}{4}) \tag{4.7}$$

$$\mathrm{v}_{sc-line} = \frac{\hbar}{m_{He4}2R}ln[\frac{2R}{a_0}] \tag{4.8}$$

Glaberson and Donnelly proposed the quantized vortex mill model which is also labeled as a type of extrinsic nucleation[64]. A remnant vortex line pinned at the orifice is stretched by the superfluid flow increasing its curvature until at the critical velocity a recombination event pinches off a vortex ring leaving the original vortex line pinned to the boundary to repeat the process. Once detached the ring expands crossing all streamlines and reduces the overall phase difference by 2π until it annihilates at the wall. A reduction in the phase of 2π reduces the velocity by a step κ/L and the energy is reduced by $\pi R^2 \rho \kappa \mathrm{v}_s$. The frequency at which vortex rings need to be created to maintain steady state is at the Josephson-Anderson frequency in equation 4.9. The chemical potential in equations 4.5 and 4.9 are in units of energy per mass. This process is temperature independent except near the lambda point at which point the vortex core becomes appreciable and its effects will affect ring dynamics. The number of remnant vortices in the orifice, which is stochastic in nature, alters the magnitude of the critical velocity but its dependence on size and temperature does not change. In orifices and pipes of larger than 1 micron there is more locations for pinning to occur which can be due to surface roughness, frozen gas, or dust particles [65]. All the vortices pinned will contribute to the generated rings and create stochastic velocities in the data. Hulin et al applied in line filters on either side of the orifice to minimize any remnant vortices from entering the orifice and being pinned[60]. They reduced the number of different critical velocity states to two states within a 6 micron orifice. Size dependent and temperature independent critical velocities were observed to be consistent with the vortex mill model. The critical velocity was expected to scale with the square root of the chemical potential. For the high velocity state a high temperature dependence was observed and was due to a new mechanism which could be generated without pinned vortices.

$$f_{JA} = \frac{\Delta P}{\rho \kappa} = \frac{\Delta \mu}{\kappa} \tag{4.9}$$

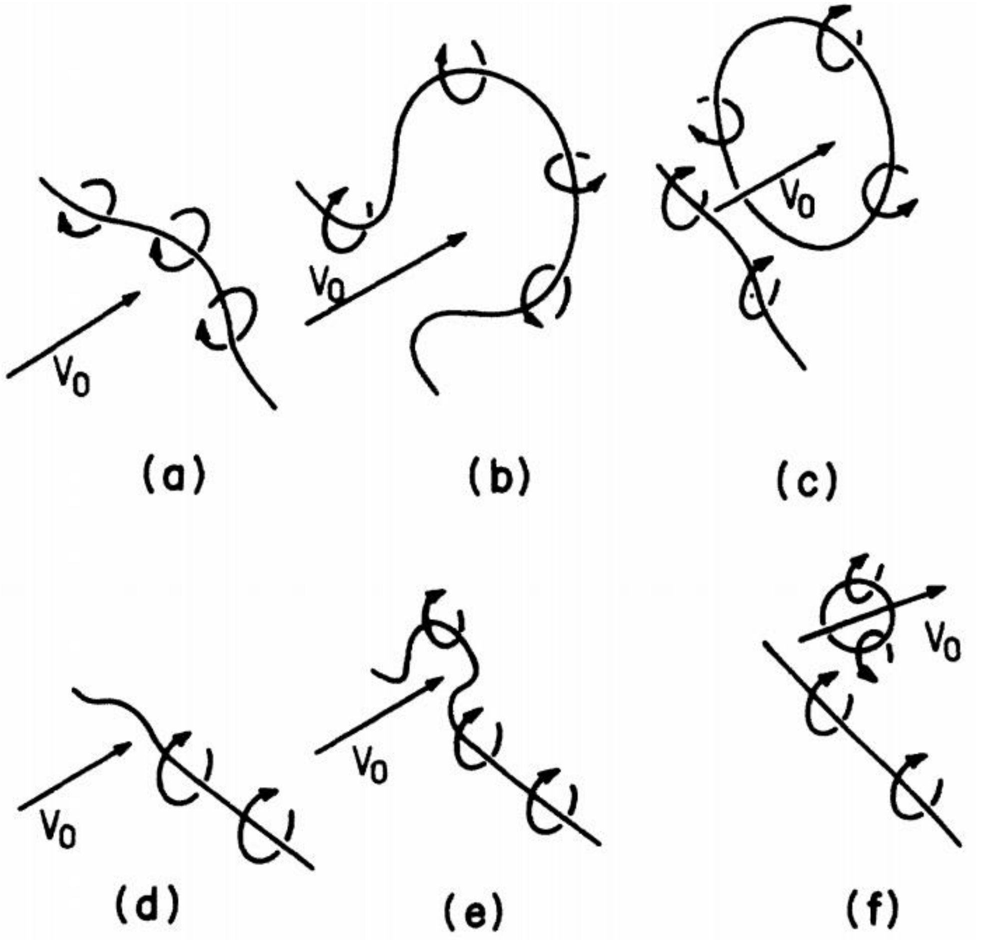

Figure 4.3: An extrinsic nucleation mechanism described by Hulin et al. in figure 8 of reference [60]. A pinned vortex line will grow (a-c) until a vortex ring is emitted using the entire length of the filament. A smaller vortex ring (d-f) can be emitted as well. These rings continue to grow crossing all streamlines and reducing the phase across the pore or orifice by 2π.

4.1.2 Intrinsic v_{sc}

In submicron orifices vortices were less likely to be found within an orifice. Instead an intrinsic mechanism first put forth by Iordanskii-Langer-Fisher (ILF) described a thermal nucleation process by which only vortices with energies equal or larger than the activation free energy ΔF in 4.10 were created [66]. Each vortex reduces the phase difference across the orifice by 2π and by equation 4.5 its velocity as well. The total velocity reduction was proportional to its thermal frequency f_T in equation 4.10 f_0 being a fluctuation frequency[67]. The free energy barrier ΔF was calculated at T=0. The influence of pressure was shown in equation 4.11 by equating the Josephson frequency f_{JA} and the thermal frequency f_T. The free energy barrier can be deduced from data. From experimental evidence two energy barriers were consistent with the data in references [68, 69, 70, 71, 72, 67, 28].

$$\frac{dv_s}{dt} = \frac{\kappa}{L} f_T = \kappa \pi R^2 f_0 e^{\frac{-\Delta F}{k_B T}} \tag{4.10}$$

$$\frac{\Delta P}{\rho \kappa} = \frac{L}{\kappa} \frac{dv_s}{dt} \tag{4.11}$$

The first type of barrier is the nucleation of a vortex ring where the activation energy is equation 4.12. The nucleation energy E_R is reduced when the momentum and flow velocity v_s are at π radians from each other. The energy of a ring is equation 4.13 and its momentum/impulse is equation 4.14. By using the quantized circulation relation 4.6 ΔF is approximated by $\beta \rho_s / \rho v_s$ where β is a weak function of temperature and v_s. When the vortex energy is inputted into equations 4.10 and 4.11 the temperature dependence of the critical velocity is proportional to $\rho_s / (T\rho)$ while the pressure dependence is proportional $1/ln[\Delta P]$[67]. The ring energy $\beta \rho_s / \rho v_s$ is only valid for T>1.2 K and any other temperature the full equation 4.12 should be used. Over a larger temperature range the temperature dependence of the critical velocity is proportional to $\sqrt{\rho_s / (\rho T)}$. An infinite velocity is predicted at T=0 which is physically impossible. Instead the velocity must approach Landau's critical velocity at T=0 where the superfluid fraction will be converted to normal helium by the excitation of rotons.

$$\Delta F = E_R + \vec{p_R} \cdot \vec{v}_s \tag{4.12}$$

$$E_R = \frac{1}{2}\rho_s \kappa^2 R[ln(\frac{8R}{a_0}) - \frac{7}{4}] \tag{4.13}$$

$$p_R = \pi \rho_s \kappa R^2 \tag{4.14}$$

In experiments by references [68, 71, 72, 28] critical velocities were measured to linearly decrease as a function of temperature. A corresponding linearly temperature dependent energy barrier ΔF was necessary to reproduce linearly temperature dependent critical velocities. Although no physical model has yet to be found which could account for a linear energy dependence, the phenomenological function 4.15 was used for the velocity and equation 4.16 for the energy barrier. The three phenomenological constants T_0, v_{co}, and E_{co} can be fitted to the data. T_0 is of the order of 1 K, v_{co} is of the order of 10 m/s and E_{co} is of the order of 100 K for submicron data. The linearity of the critical velocity is valid until quantum tunneling dominates over thermally fluctuated vortices. As with any quantum mechanical system there is a finite probability for tunneling through the energy barrier. The transitional temperature is determined by equating the thermal exponent of the Arrhenius equation to the exponent for tunneling through a square well of width w. In reference [72] the activation energy was assumed to be 106 K and a characteristic width of 10^{-8}m. With these values T_Q was calculated from equation 4.17 to be 0.25 K. The critical velocity indeed was observed to transition to a temperature independent velocity between 200 mK and 400 mK in references [73, 74].

$$\mathrm{v}_{sc} = \mathrm{v}_{co}(1 - \frac{T}{T_0}) \tag{4.15}$$

$$E_{sc} = E_{co}(1 - \frac{T}{T_0}) \tag{4.16}$$

$$T_Q = \frac{h}{2\pi w k_B}\sqrt{\frac{E_0}{2m_{He4}}} \tag{4.17}$$

4.2 Pressurizing Superfluid

To liquify helium the cell was thermally anchored to a continuous pulse tube $^3He/^4He$ cryostat described in section 2.3. Ultra high purity ^4He gas was introduced into the cell through a 1/4″ pipe down to the 4 K plate followed by a 1/8″ pipe. The inlet pipe was heat sunk to the 40 K and 4 K plate to ensure it was precooled. To minimize superfluid heat leaks and allow a pressurization of the cell a 3 inch length capillary pipe with inner diameter 250 microns was attached between the 1/8″ pipe and cell. A 1/4″ pipe connected from the outlet to room temperature was necessary to ensure an ultra low vacuum was present to vaporize all liquid helium. Two sintered stainless steel mesh filters with a 0.5 micron nominal pore size from Swagelok were thermally anchored at the 4 K plate and placed inline to the inlet and outlet lines. The purpose of the filters was to purify the liquified ^4He from trace gases and to prevent blockage of the nanopore from any oil contaminants in our system. The design of the actual low temperature copper cell was described in section 2.2. Data in the next section are for two single mica nanopores of diameter 31 nm and 89 nm and one PET nanopore with a 75 nm diameter.

4.3 Superfluid Data

All velocities measured in our system can be assumed to be at their critical state. Previous work with phase separators have found intermediate flow states beyond the inviscid state that are possible because of the superfluid/vapor interface [75, 76, 77]. Although the pressure differences were comparable to our own ≈10 Torr our pressure gradients which are the relevant parameter are 10^3 times larger for most P_R and can therefore be always assumed to be in the final critical state. Our system inherently carries a pressure gradient on the order of 10^6 Torr/m due to the column of liquid helium above the pore. This constant column pressure of 67.8 Torr dominates below $T_R < 1$ where the vapor pressure is much less than 1 Torr.

A critical velocity can be calculated by equation 4.18 with a measurement of the total flow Q, temperature T_R and nanopore radius R. To simplify calculations the following assumptions were made which are valid far from T_λ. The superfluid velocity far exceeds the normal velocity so that the normal component can be set to zero $\mathrm{v}_n = 0$ and the superfluid density can be approximated by the total density $\rho_s \approx \rho$. With these assumptions the velocity was simply calculated by equation 4.19.

$$\mathrm{v}_s = \frac{1}{\rho_s}\left(\frac{Q}{\pi R^2} - \rho_n \mathrm{v}_n\right) \tag{4.18}$$

$$\mathrm{v}_s \approx \frac{1}{\rho}\left(\frac{Q}{\pi R^2}\right) \tag{4.19}$$

4.3.1 Isotherm Flow

Similar to the set of flow experiments involving normal liquid helium described in section 3.6 superfluid flow rates Q were measured as a function of pressure P_R at constant temperature T_R. The cell could be pressurized an additional ≈10 Torr in addition to its coexistence pressure before the temperature destabilized. The gas flow was too small to be measured and was not shown in any of the superfluid figures. The flow data through a 75 nm PET nanopore had a large deviation around the mean value of 3.25 m/s in figure 4.4. To first order at T=0.7 K the flow had a positive linear dependence on pressure up to a pressure difference of P_R=8 Torr. Fitting the 0.7 K data to a linear relation $\mathrm{v}_{sc} = \mathrm{v}_0(1 - P/P_0)$ the parameters $\mathrm{v}_0 = 3.17$ (m/s) and $P_0 = -28.24$ Torr were found.

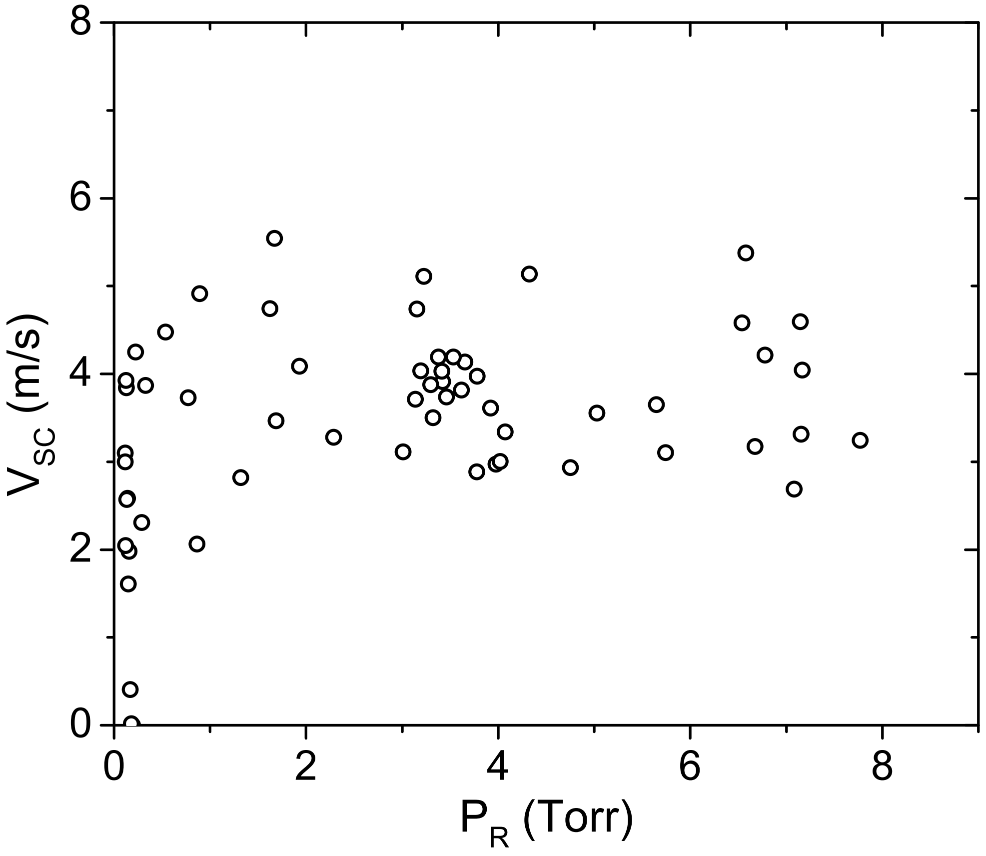

Figure 4.4: Flow rate Q vs pressure drop P_R at T_R=0.7 K for a single 75 nm size PET nanopore. The mean velocity was at 3.25 m/s and a fit to the linear relation $v_{sc} = v_0(1 - P/P_0)$ gives $v_0 = 3.17$ (m/s) and $P_0 = -28.24$ torr.

The large deviation in velocities we hypothesize was a result from the etching process leaving very rough surfaces in PET. The chances for several line vortices to be pinned in a rough pipe was increased greatly leading to a stochastic nature in the velocity.

T_R (K)	v_0 (m/s)	P_0 (Torr)
0.6	10.63	-243.14
0.9	9.17	-100.12
1.4	7.90	3006.99
1.6	6.39	634.44
1.8	4.63	214.93
2.0	2.66	59.02
2.1	1.48	45.54

Table 4.2: Isotherm parameters (v_0, P_0): Data from figure 4.5 fitted to $v_{sc} = v_0(1 - P/P_0)$.

The atomically smooth surface of mica we believe reduced pinning of residual vortices inside the nanopore. Figure 4.5 presents a set of critical velocities in a 31 nm mica nanopore. The initial velocities decreased with increasing temperature of 0.6 K, 0.9 K, 1.4 K, 1.6 K, 1.8 K, 2.0 K, and 2.1 K with a maximum velocity of 10.7 m/s. For each isotherm the velocity began at pressure P_R that coincided with vapor pressures at bulk coexistence. Pressure differences up to a value of 10 torr from bulk coexistence were made. The deviations in mica of the velocity around its mean value were smaller than deviations within a PET nanopore. Table 4.2 lists the best fit parameters for the linear relation $v_{sc} = v_0(1 - P/P_0)$ for each of the isotherms. For the isotherms at T_R<1.4 K the velocity had a positive dependence on pressure. At $T_R \geq 1.4$ K the velocity decreases linearly as a function of pressure with larger slopes as T_λ was approached. A negative linear pressure dependence near T_λ has not been reported in previous experiments. Although our previous assumption of $\rho_s \approx \rho$ near T_λ is no longer valid, the overall pressure dependence of the velocity should not be affected. The density of liquid helium should have increased as a function of pressure and an increase in velocity should be expected instead. The intrinsic nucleation theory predicts the pressure dependence to be inversely proportional to $\ln[\Delta P]$ which was a trend we observed below T_R<1.4 K where vortex core interactions with the normal component were negligible. For $T_R \geq 1.4$ K these interactions would become more dominant. The Josephson frequency predicts vortices must be crossing all stream lines on the order of 10^8 per second at a ΔP=10 Torr in order to maintain a steady state. As these vortex rings are growing they could be interacting in a complex manner with other vortices and scattering off thermal excitations creating additional phase slips in the flow [78, 79].

4.3.2 Coexistence

The critical velocity versus the reservoir temperature T_R offers insight into the nucleation mechanism within the nanopore itself. For the velocities along the coexistence curve the cell was filled with liquid helium and the temperature swept through a range 0.5 K<T_R<3.5 K. In this configuration, the pressure drop was simply equal to the bulk coexistence pressure. Two states were present in the 75nm PET data in figure 4.6 at T_R<1.8 K. The red circles and black squares were data from before and after a thermal cycling to room temperature. The data were taken in no preferential order of temperature with the higher state being consistently less stable than the lower state. There were instances where the velocity would make an abrupt transition from the higher to the lower state with no outside operator perturbation to the system. The pulse tube mechanism from the cryostat itself created vibrations at a few Hz, but this appeared to have little effect on the stability of the higher state. The transitions only occurred from the higher to the lower state and the lifetime of the higher state decreased as T_R was lowered. The temperature independent velocities at T_R<1.25 K resulted from vortices being nucleated at least two locations within the nanopore via the vortex mill model. Feynman's critical velocities for a line and ring vortex were shown as dotted and dashed lines respectively. The velocities appeared to be of the right order of magnitude with the vortex ring model being closer to the nominal values. The two states merged at T_R>1.8 K where at T_λ the flow returned to the normal viscous state. The superfluid velocity exceeded the normal velocity by up to 40 times. The velocity appeared to decay somewhat exponentially near T_λ. The decay was quicker than what an intrinsic mechanism could account for $(\rho_s/\rho T)^{1/2}$. The increased dissipation may be the result of a form of quantum turbulence. A complex, self sustaining entanglement could be interacting with the thermal excitations. Such calculations in that regime were

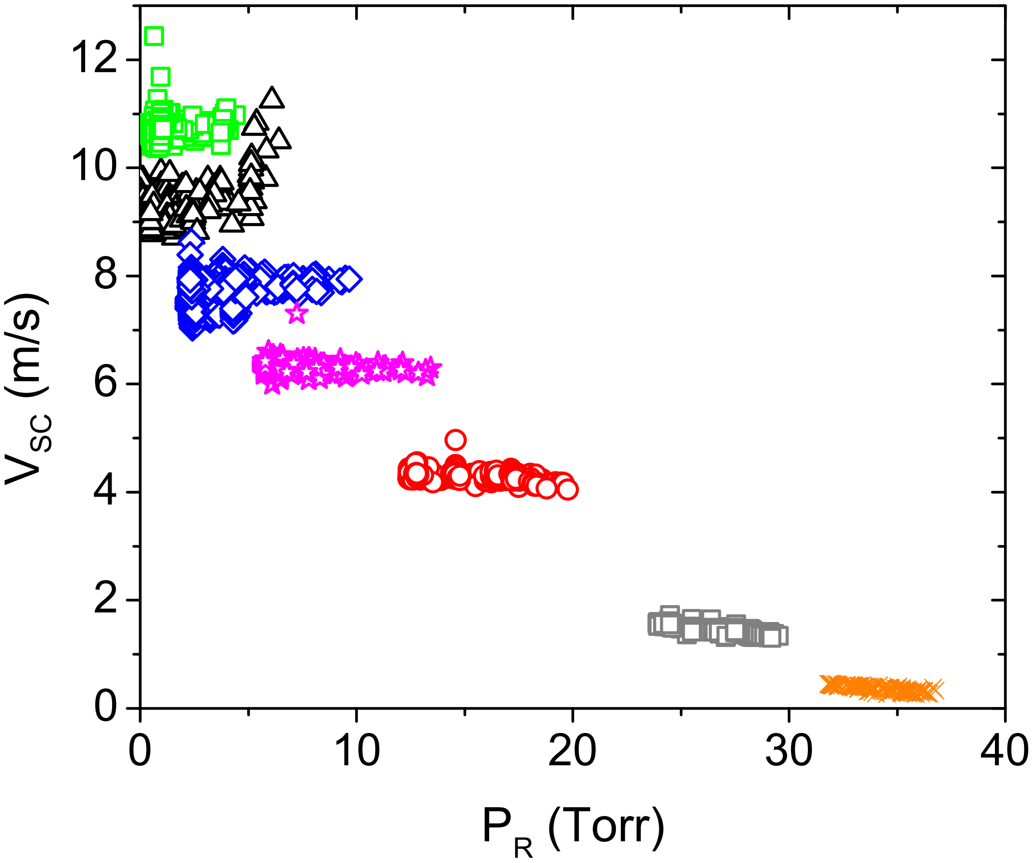

Figure 4.5: Critical velocity data for a single 31 nm, mica nanopore at several isotherms T_R. The mean velocities for each data run decrease as temperature T_R increased. The data legend list: green squares 0.6 K, black triangles 0.9 K, blue diamonds 1.4 K, magenta stars 1.6 K, red circles 1.8 K, gray squares 2.0 K, orange X's 2.1 K. The pressure dependence of the critical velocity fits the relation $v_{sc} = v_0(1 - P/P_0)$ well with the parameters v_0 and P_0 in table 4.2. The positive dependence on pressure decreases as the temperature was increased. Between the temperatures 0.9 K and 1.4 K the pressure dependence crosses to a negative pressure dependence and continued decreasing as T_λ was approached.

beyond the work of this thesis. A complete thermal cycling of the nanopore appeared to affect little the velocity magnitude. The lower state though appeared to be less stable in the subsequent cycling than the higher state. Perhaps freezing of gases on the surface changed pinning locations and the stability of the vortices. We believe the two states and failure to observe an intrinsic nucleation can be tied to the very rough surfaces of the PET nanopore. Typically in submicron orifices there was a lack of pinned vorticity but in longer nanopipes the number of pinning sites increases with surface area. Channels with smoother surfaces such as mica should have a lower probability of pinned vorticity and open up a chance to observe a thermal nucleation process.

After examination of the interiors of mica and PET nanopores in figure 2.2 and 2.3, we decided to try mica membranes as mica surfaces appeared to have less surface irregularities. Two single, mica nanopores of 89 nm and 31 nm diameter were etched and tested in our system one at a time. The etching procedure for mica nanopores was described in section 2.1. Before etching the mica membranes were cleaned in a 3 M solution of KOH at 70° F for 30 minutes then rinsed in deionized water. After etching current-voltage (I-V) measurements were done on two subsequent days to confirm the diameter. The 89 nm had velocities comparable to the PET nanopore but only had a single state with a linear temperature relation $\mathrm{v}_{sc} = \mathrm{v}_{co}(1 - T/T_0)$. The temperature was swept through the range 0.5 K to 3.5 K over the course of a week and a half. After a new temperature was set the mass flow was allowed to equilibrate again and waited for a minimum of two hours before a measurement was taken. The parameters for the blue,solid line in figure 4.7 were v_{co}=3.69 m/s and T_0=2.79 K. At T_R>2.0 the velocity decayed quickly to the normal flow with no slip. A linear temperature relation was consistent with a thermal nucleation process with an activation energy that was also linearly temperature dependent. The smoother surfaces of the mica appeared to remove the remnant vorticity that was prevalent in the PET nanopore.

The temperature independent state appeared once again though in a smaller 31 nm mica nanopore. The black circles in figure 4.8 show the velocities measured by sweeping the temperature similar to the previous two nanopores. The red squares show the initial velocities taken from pressure sweeps at a constant temperature. Similar to the PET nanopore there appeared to be two

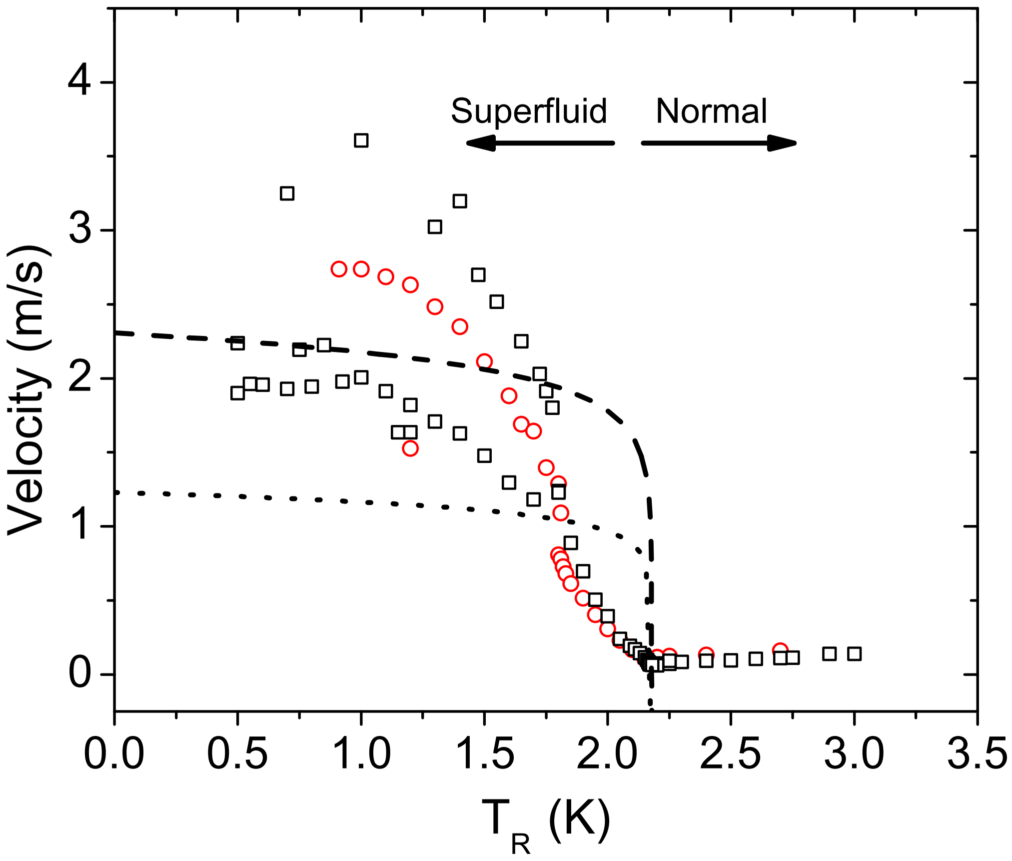

Figure 4.6: Velocity as a function of reservoir temperature T_R for a 75 nm PET nanopore. The black square data is taken after initial cooldown and the red circles are after thermally cycling to room temperature. The cell was filled with liquid helium and then swept through various temperatures waiting for each velocity to stabilize before taking a measurement. Each set of data was taken over the course of a 10 days. Below 1.3 K a temperature independent regime was observed which alternates between two states. At 1.8 K the two branches merged and quickly decreased to the normal state at 2.17 K. Above T_λ the velocities were consistent with a viscous fluid. The dashed and dotted lines were Feynman's critical velocities for a ring and linear vortex respectively. The PET surface roughness provides many locations within the nanopore to pin remnant vorticity coming from a superfluid reservoir.

states within the nanopore. However we believe the smoother walls allowed an environment that was cleaner in remnant vorticity. The states appeared to vary between a single, pinned vortex and in some instances the nanopore can be free of remnant vorticity. The isotherm data can be fitted well below T_R<1.5K with the solid, blue line from equation 4.15 meaning a thermal nucleation mechanism was present. The parameters were v_{co}=12.80 m/s and T_0=3.41 K. The dashed line was Feynman's vortex ring model and underestimates the critical velocity. Perhaps at pinned vortex location the local diameter may be smaller. A 20 nm vortex ring would yield velocities comparable to our data. At temperatures greater than 1.8 K the two velocity states appeared to merge transitioning to the normal state at $T_R=T_\lambda$. The quick decrease in velocity could be the result of interaction between vortex cores and thermal excitations in the liquid.

The full effects of the superfluid/vapor interface are still not understood within our system. Because the isothermal and coexistence data were similar to orifices and channels where the interface was absent we cannot infer details of its importance. The location of the interface is believed, however, to be external as in figure 3.1 part C. The high flow rates and small vapor pressures forces an external interface to exist. Perhaps vortex nucleation via quantum tunneling may provide valuable information of the role of a vacuum interface.

4.4 Conclusion

The presence of a temperature independent state within a submicron nanopore contrasts sharply with previous research on submicron orifices. In submicron orifices the thermal nucleation of vortices dominates the dissipation of the driving chemical potential gradient. Instead our submicron nanopores behaved similarly to apertures larger than micron dimensions. The difference we believe was a result of the increased number of pinning sites available inside long nanopores. Our research goals are to investigate the thermal nucleation process within nanopores. To observe thermal nucleation within our nanopores the number of remnant vortices entering and being pinned in our channel must be minimized or eliminated entirely. An in line filter had been suggested

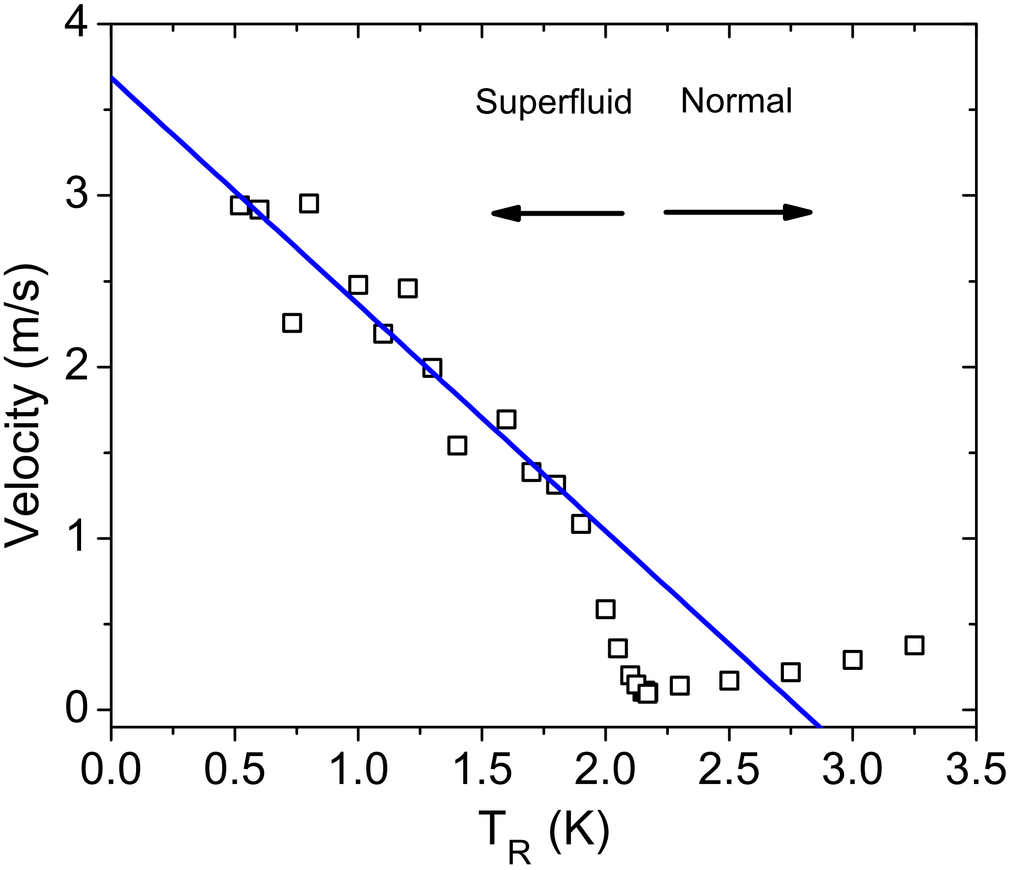

Figure 4.7: The velocity through a 89 nm mica nanopore as a function of the reservoir temperature T_R. The cell was filled with liquid helium and then swept through various temperatures waiting for each velocity to stabilize before taking a measurement. The data set was taken over the course of a week. The solid, blue line was the linear temperature model $v_{sc} = v_{co}(1 - T/T_0)$ with v_{co}=3.69 m/s and T_0=2.79 K. The data fits well from T_R<2.0 K. At T_R>2.0 the velocity quickly approaches the velocity of a no slip, normal fluid. The linear model was indicative of a thermal nucleation mechanism with an activation energy linearly dependent on temperature.

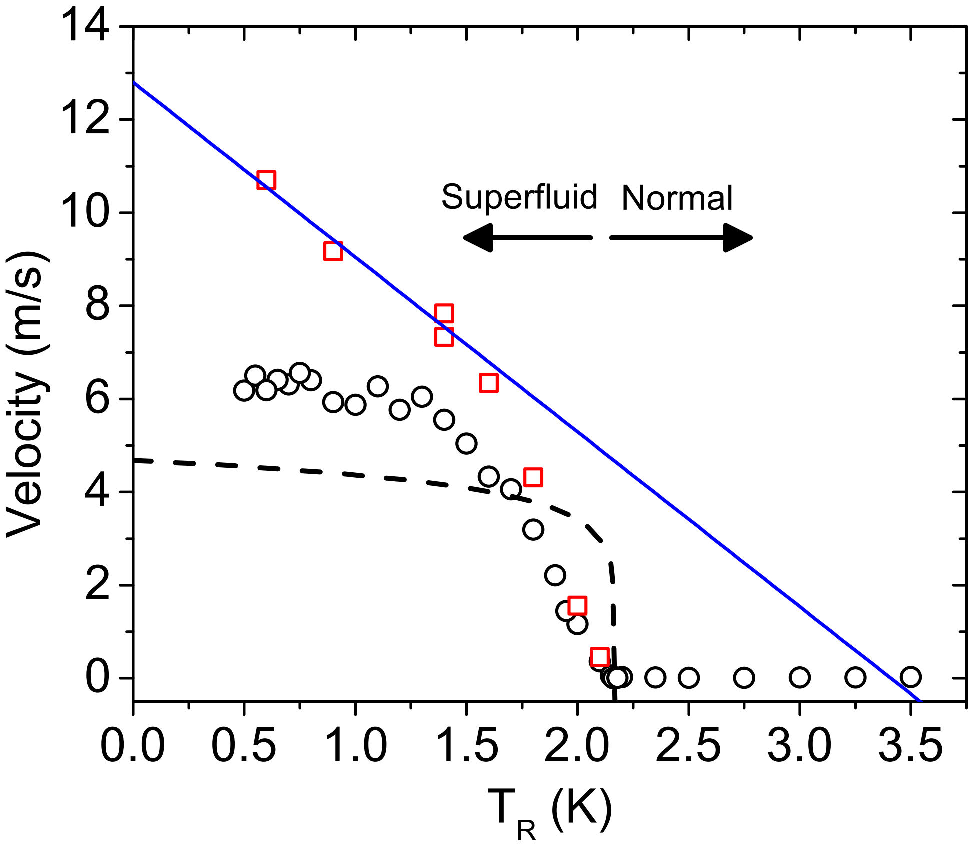

Figure 4.8: The velocity through a 31 nm mica nanopore as a function of the reservoir temperature T_R. For the black circles the cell was filled with liquid helium and then swept through various temperatures waiting for each velocity to stabilize before taking a measurement. The red squares were the initial velocities from the isotherms. The blue, solid line was the linear temperature model $v_{sc} = v_{co}(1 - T/T_0)$ with v_{co}=12.80 m/s and T_0=3.41 K. The dashed line which underestimated the data was Feynman's vortex ring model assuming a diameter of 31 nm. A 20 nm vortex ring model instead models the temperature independent regime better. The isotherm data corresponded to a thermal nucleation with a linearly temperature dependence on energy. At T_R>1.5 the velocity decreased and transitioned to a viscous flow at T_R=T_λ.

to reduce this problem in micron apertures and is a simple modification to our cell. In addition we hope with the removal of remnant vorticity and an improvement to our cryogenic temperature down to at least 300 mK the transition from thermal to quantum nucleation could be also be investigated within nanopores.

A future goal of this research is the measurement of the pressure dependence of the critical velocity at high pressure drops. The large thermal conductivity and easy mobility of a superfluid implies that the heat leak due to the fill line for the high pressure reservoir can be substantial. The thermal load on our current refrigeration system was too large when pressurized and the stability of our temperature was too low, with a thermal fluctuation of ΔT=10 mK. The superfluid transition temperature is expected to be suppressed by size effects on the order of a few milliKelvin for a $\approx 50nm$ nanopore. However our current temperature resolution was insufficient to measure the suppression accurately. The temperature suppression is important information at it tells valuable information on the vortex core.

Two improvements are planned to increase the pressure range of our cell. The first will be increasing the cooling power of our cryostat by the conversion of the current ^3He evaporative fridge to a ^4He evaporative fridge. Although this will raise the bottom temperature to ≈0.8 K the cooling power should increase by five times to ≈15 mW. The second improvement is the installation of a low temperature valve to close the cell and maintain the liquid helium in a pressurized state while removing the superfluid heat leak. The conversion of a stainless steel valve to a cryogenic valve is possible by replacing gaskets with indium wire and the plastic ball seal with a torlon ball [80]. The measurement of the pressurized liquid will be through a measurement of the frequency shift of 32 kHz tuning forks [81, 82]. With the addition of these improvements the critical velocity in an intrinsic nucleation can be measured for the first time to pressure drops on the order of a few Atm. With such large pressure gradients the effects of quantum turbulence within the small scale nanopores could become important below T_R<1.3 K where thermal excitations are negligible.

Carbon nanotubes offers a new platform for which would be advantageous for our system. The atomically smooth walls of carbon nanotubes could leave these nanotubes free of remnant vortices. The lengths of nanotubes can be as long as a few millimeters and the pressure gradients would be reduced significantly. The onset of dissipation could then also be observed. Perhaps the liquid/vapor interface effects would be more noticeable. Finally the 2 nm diameter of a carbon nanotube approaches the size where a Luttinger liquid was predicted [83, 28].

Chapter 5

Helium-4 Phase Transitions on Intermediate Strength Substrates

5.1 Motivation

This chapter switches the research focus to phase transitions of ^4He on alkali substrates. When a few monolayers of ^4He are adsorbed on a surface a variety of two dimensional phenomena emerge. Analogous to a three dimensional bulk system thin films can exist either as a solid, liquid, gas or in the case of helium as a superfluid. The determination of the stable state depends on the potential well depth of the substrate and interatomic potential of helium[84, 85]. Gold and graphite are examples of substrates with strong potentials for which solidification in the first few layers have been demonstrated in Ref. [86, 87]. Once the substrate potential is shielded by the first few solidified layers than a liquid, gas, and superfluid film can be observed in subsequent layer formations. For weaker substrates, no layers are adsorbed until the prewetting line is reached. A prewetting transition is a first order phase transition marked by a discontinuous step in film thickness that occurs at a chemical potential less than coexistence. In the chemical potential vs temperature phase diagram the prewetting line begins at the wetting temperature T_w on the bulk coexistence and monotonically decreases until it ends at a 2D critical point T_c where $T_c > T_w$. Cesium is the only material weak enough for helium to have a finite wetting temperature. The measured phase diagram and discussions of helium on cesium are reported in Ref. [88, 89, 90, 91, 92, 93].

Alkali metals were predicted to be intermediate in strength with the strength of the potential monotonically increasing with atomic mass. The last electron is forced to be predominantly at the farther orbital weakening the short range forces. Lithium and sodium being the heaviest of the alkali metals are classified as intermediate strength substrate. With the absence of solid layers submonolayer helium films grow in direct contact with the surface and the liquid/vapor and superfluid transitions can be observed. Our efforts were to map out the intersection of the superfluid and classical phase transitions and measurement of the 2D critical point. For sodium and lithium it was predicted to be at ≈0.8 K. Previous studies with sodium and lithium were unsuccessful in observing the liquid/vapor transition and the 2D critical point [94, 95, 96]. We report the first evidence and measurement of the 2D critical point on sodium with an ellipsometer.

5.2 Thin Film Deposition and Measurement

Alkali metals are highly reactive as their outermost electron is readily donated in a chemical reaction. As a result oxidation of its surface occurs rapidly when exposed to air. To ensure smooth and chemically pure films, all alkali films were deposited in situ within our high vacuum cryostat at 4 K. An alkali target is placed 2 cm from the gold electrodes of a quartz crystal microbalance (QCM). After the QCM is rotated into a shutter position an Nd:Yag 532 nm laser is pulsed at 30 Hertz where 50-100 mJ/pulse ablates the alkali target cleaning an area of 1 cm^2 [96]. A clean alkali film is ablated onto each gold electrode by alternating sides with a rotational stepper motor. Each side is coated twice with 30-40 layers per ablation. A total of ≈80 layers are ablated uniformly to each side. In a later set of experiments the QCM crystal was substituted with a highly order pyrolytic graphite piece (HOPG) of surface area 1 cm^2 and 1.2 mm thick from K-Tek Nanotechnology LLC. For the HOPG piece only one side was deposited with an alkali film ≈80 layers thick.

5.2.1 Quartz Crystal Microbalance

A QCM is a shear mode oscillator with a high quality factor Q$\approx 5x10^5$ in vacuum. Shear mode oscillators are used as sensitive mass balances in thin film experiments[97, 96, 98]. Third harmonic, AT-cut crystals with a resonant frequency of 5.0 MHz were purchased from Laptech Precision. An HP 8751A Network Analyzer measures the response of the secondary gold electrode on the QCM while sweeping through a frequency range with the primary gold electrode. The quartz crystal is electrically equivalent to an RLC circuit and the frequency response will fit to a Lorentzian curve. The network analyzer outputs the resonant frequency f_0 as the maximum value in a frequency sweep. The quality factor Q of the resonator is calculated by fitting the data to a Lorentzian curve and using the resistance R_0, inductance L_0, and capacitance C_0 as the free parameters. The quality factor is equal to $\frac{2\pi f_0 L_0}{R_0}$ and the dissipation is equal to R_0.

The frequency shift is proportional to the adsorbed film thickness d_c by equation 5.1. One layer of helium is equivalent to the crystal lattice spacing of 3.57 A. The quantity ρd_c is the two dimensional areal density σ_{film}. The necessary parameters in equation 5.1 are the bulk density of liquid helium ρ, the acoustical impedance Z=8.86$x10^6$, n=3 for the third overtone, and the resonant frequency in vacuum $f_0 \approx 5.0$ MHz. A frequency shift Δf of -0.195 Hz is calculated for one monolayer of adsorbed helium and the resolution of our system is a few mHz.

$$\Delta f = -\frac{4(f_0)^2 \rho d_c}{nZ} \tag{5.1}$$

A shear mode oscillator measures film growths by the viscous coupling of a fluid to its surface. As the film thickens the oscillator effectively increases its mass and a negative frequency shift occurs. Helium-4 has a unique 2D superfluid transition which decouples the film from the surface and essentially becomes invisible to this mode of measurement. Any thickness discontinuities or phase changes will be missed once the KT transition occurs. Ellipsometry can measure the total film growth irregardless of the superfluid fraction [99, 86]. A simultaneous ellipsometric and QCM measurement offers a complete mapping of the 2D phase diagram.

5.2.2 Ellipsometer

A photoelastic modulated ellipsometer (PEM) offers submonolayer resolution by measuring changes in the polarization parameters Ψ and Δ on the order of 0.4 $\mu Rads$ and 0.2 mRads respectively.The individual components were purchased from Hinds Instruments and installed to our cryostat as shown in figure 5.1. A Melles Griot frequency stabilized HeNe 632.8 nm laser light was reduced to $\approx 1\mu W$ by an OD3 filter then directed into the cryostat through a 2.5″ window. The light was given a linear polarization of 45° then modulated sinusoidally by the PEM at 50 kHz with a retardation amplitude of $\varphi_r = 137.785°$. The light transmitted through the KG1 windows on the 40 K and 4 K shield followed by a reflection off the substrate at T=0.5 K. The reflection causes a polarization shift linearly proportional to the film thickness for small values. The light continues and exits the cryostat where the analyzer rotates the polarization by $-45°$ and enters into a Hamamatsu R2949 photomultiplier (PMT) tube for detection. The PMT and analyzer were enclosed in a metallic hat for the PMT to function properly in a dark environment. The analyzer and polarizer were of the Glan-Thompson type. A SRS PS325 high voltage power supplied powered the PMT through high voltage electrical feedthroughs. The intensity of the measured signal was dependent on the supplied voltage with a maximum sensitivity at 1 kV. A voltage of 600 to 700 V was sufficient to maximize signal to noise ratios without saturation. The output current signal was converted, inverted and amplified to a positive voltage by a Stanford Research Systems SR570 preamplifier. A Hinds Signal Conditioning Unit (SCU-100) separated the voltage signal into its time dependent and independent values. The DC component was measured by an Agilent 34401 digital multimeter and the frequency dependent signal by a Stanford Research SR830 Lock-in amplifier. The 50 KHz PEM signal was used as the reference for the lock-in and the fundamental component 1f and second harmonic 2f at 100 kHz of the signal were measured and recorded with Labview along with the DC voltage.

The ellipsometer signal intensity is a monotonic function of the complex index of refraction n_i. Helium is nearly transparent with n_{He}=1.028 very close to the value of vacuum n_v=1. In com-

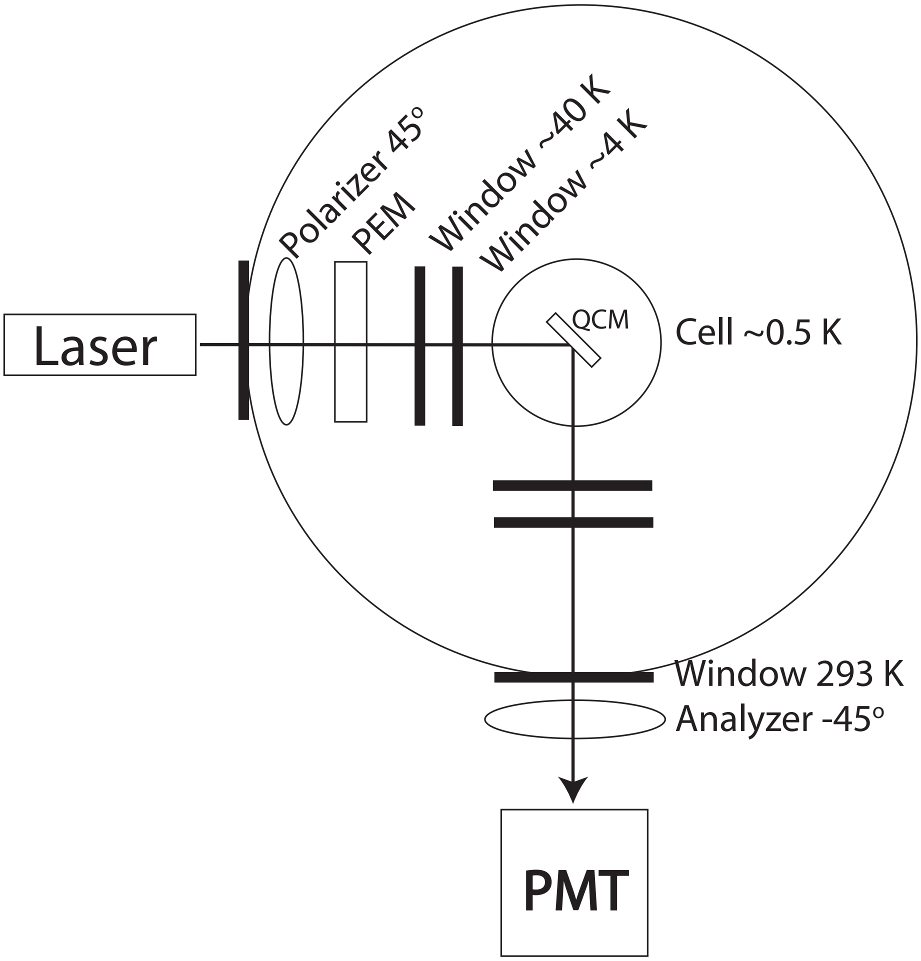

Figure 5.1: The ellipsometer components were attached directly to the cryostat. A 632.8 nm, frequency stabilized HeNe laser was reduced in power to 1 μW by an OD3 filter. The laser was directed at a substrate inside the cryostat. The polarizer and PEM were maintained at T=308 K to within 5 mK. The Glan-Thompson polarizers imparted a 45° linear polarization to the signal. The PEM oscillated the polarization at 50 kHz with an amplitude of 137.785°. The laser reflected of either a gold electrode or HOPG surface at T=0.5 K where an adsorbed film of helium shifted the polarization by an amount proportional to the thickness d_c. The signal exited the cryostat and passed through an analyzer at −45° and was measured with a Hamamatsu PMT tube. The analyzer and PMT tube were kept in the dark with an enclosure which also isolated from convective wind currents. The signal was then converted to a voltage and measured with a DMM and lock-in amplifier for the the DC, 1f, and 2f components.

parison water has a much larger index of refraction n_{H20}=1.31. To maximize the signal to noise ratio for submonolayer helium films we systematically isolated and minimized several sources of noise which were of mechanical, thermal, and optical in origin. First vibration induced noises were reduced by attaching all ellipsometer components including the laser and PMT directly to the cryostat. The mechanical attachment also ensured optical alignment. Second the laser reflections from each window generated a cascade of reflected lights within the cryostat. Reducing the power of the laser by three orders of magnitude significantly reduced the intensity from these secondary sources. The third source for noise were the thermal gradients on the glass windows. Thermal gradients induced birefringence which rotated the polarization by non zero values over time constants on the same order as an experimental run of 12 hours. Specially treated Schott KG1 glass were annealed in an oven over several weeks to remove any thermal stresses trapped in the glass. These circular windows were then epoxied into thin rimmed, titanium window holders. The thermal expansion of titanium and glass were similar enough to prevent stresses when cooling down. The titanium holders were indium sealed into the 40 K and 4 K shields. KG1 Schott glass absorbs infrared radiation and were not necessary for the cell windows. Instead SF-57 glass which was specifically designed for low birefringence applications were indium sealed to the cell for optical access. The outer windows on the cryostat were of standard borosilicate glass. To remove the birefringent effects of the incoming borosilicate glass the polarizer and the PEM were placed inside the vacuum environment of the cryostat. Only changes in polarizations after the polarizer component were important. Thermal drifts of the optical components were reported to shift the polarization in ref. [99]. The polarizer was mechanically and thermally attached to the PEM and moved into the vacuum of the cryostat for thermal isolation. We further temperature regulated the combined polarizer/PEM unit with a PID loop at T=308 K to minimize temperature fluctuations to +/-5 mK. The analyzer and PMT were out of necessity placed outside the cryostat. The ellipsometer after cool down needed to be realigned as the thermal contractions were significant. To minimize thermal drifts in these components and provide the PMT a dark environment a covering was placed over these components to remove convective air currents.

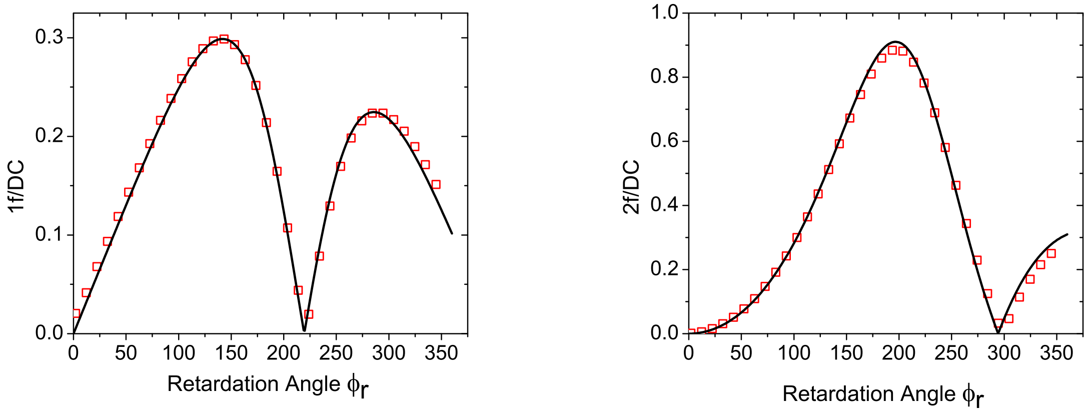

(a) Data of the first harmonic to the DC component ratio (red squares) as a function of the retardation angle for a gold electrode on the QCM. The table top measurement was open to the room environment at P=1 Atm and T=293 K. The black line is the theoretical values with the bulk index of refraction for gold n_{au}=0.124+ 3.26I.

(b) Data of the second harmonic to the DC component ratio (red squares) as a function of the retardation angle for a gold electrode on the QCM. The table top measurement was open to the room environment at P=1 Atm and T=293 K. The black line is the theoretical values with the bulk index of refraction for gold n_{au}.

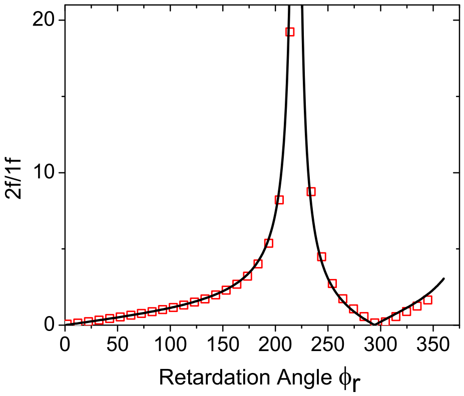

(c) Data of the second harmonic to the first harmonic ratio (red squares) as a function of the retardation angle for a gold electrode on the QCM. The table top measurement was open to the room environment at P=1 Atm and T=293 K. The black line is the theoretical values with the bulk index of refraction for gold n_{au}.

Figure 5.2: Ellipsometer ratios for gold film in air at T=293 K.

To confirm the ellipsometer setup and theory were correct, the ellipsometric ratios 1f/DC, 2f/DC, and 2f/1f were measured as a function of the PEM retardation angle φ_r. The ratio of these signals were plotted to eliminate variations in the intensity of the signal. Our system could be approximated as a two layer system consisting of the helium film and a bulk alkali metal. The full theory for a phase modulated ellipsometer in a two layer system was given in refs. [100] and [101]. Data in figure 5.2 were taken in a simplified setup with the components on a table top and open to air at P=1 Atm and T=293 K. The sample substrate was the gold electrode film on the flat side of the plano-convex QCM. The black lines were from the theory in refs. [100] and [101] with the adsorbed helium layers set to zero and the bulk index of refraction for gold n_{au}=0.124+3.26I [102]. Although the gold electrode was a film a few hundred nanometers thick the bulk index of refraction models the signals well. This model can easily be used to measure the index of refractions for other bulk and thin films by fitting the ellipsometric ratios to data. One thing to note on the index of refraction nomenclature in references [100] and [101] is the imaginary part k is defined as negative n_i=j-kI. The new sign convention must be adopted to correctly model the signal change as a function of adsorbed layer growth.

The room temperature sodium index of refraction n_i=0.039+2.73I for a 633 nm wavelength was used in our theoretical modeling [103]. A wider spread of values for the HOPG index of refraction were found in the literature. n_i=3.2+2I worked well for our own HOPG sample [104]. To measure helium films the change in the ellipsometric ratios were measured as a function of pressure at a constant retardation angle. The retardation angle $\varphi_r = 137.785°$ maximized the 2f and 1f signals as a function of layer growth. The ratio of the harmonic components had smaller noise levels and we used for most of the measurements. For small film thickness the first harmonic 1f can be approximated as $\approx \alpha d_c$ and the DC component as $\approx \beta d_c + \gamma$ where d_c is the thickness of the film. The ratio of these components becomes proportional to the thickness $\alpha d_c/(\beta d_d + \gamma) \approx \frac{\alpha}{\beta} d_c$. By assuming a constant calibration factor the calibration error deviates by $\approx 1\%$ at 1 layer completion. The experimental calibration factor $\frac{\alpha}{\beta}$ was measured by fitting the ellipsometer signal to the QCM data. The experimental calibration factors for the 2f/1f data in figure 5.6 were 25% and

111% of the the theoretical value of 0.000906445 signal/layer. The differences could be related to the temperature dependent index of refraction or the laser spot shifting locations on the surface of the film in between isotherms.

5.3 2D Phase Diagram

Analogous to the bulk superfluid phase, helium can have a corresponding superfluid transition in a thin film. The Kosterlitz-Thouless (KT) transition (Eq. 5.2) predicts that at a temperature T_c there exists a critical thickness d_c at which the onset of superfluidity occurs. Equation 5.2 simplifies with the appropriate constants to $d_c = 2.75T_c$ where d_c here is measured in layers and T_c in Kelvin. This prediction was derived independent of a substrate and should be a universal feature. A superfluid state is unique to helium where the pairing of quantized vortices creates a pseudo long range order. At constant areal density the vortices unpair at T>T_c and superfluidity is destroyed.

$$T_c = \frac{\pi\hbar^2}{8k_B m_{He4}^2}\sigma_{He4} \tag{5.2}$$

$$\sigma_{He4} = \rho d_c \tag{5.3}$$

In addition to the superfluid transition, which is governed by quantum mechanics, helium films can also undergo a classical 2D liquid-vapor transition which is driven by classical van der Waals interactions. Analogous to the bulk phase, a liquid-vapor coexistence curve terminates at a critical point in two dimensions. Unlike the bulk phase the critical point can shift due to the substrate and is predicted to be at $\approx 0.8K$ for sodium and lithium. The existence and interaction of these classical and quantum transitions lead to two predicted phase diagrams in figure 5.3. In the first case the KT transition intersects the coexistence curve below the critical point as in figure5.3(a). The experimental QCM signature in our isotherms should be marked by three different regions. Isotherm at temperatures greater than the critical point a normal KT transition can be expected. A KT transition is marked by a dip in the frequency signal where the fluid viscously decouples and an associated peak in the dissipation. Between the T_c and T_{end} the isotherm signal should be fairly flat with a sudden step growth signaling coexistence followed by a steady liquid growth then a sudden drop signaling the onset of superfluidity. Below T_{end} the expected experimental signal is debated. From the point of view of a classical phase transition there should be a discontinuous step growth at coexistence. However the new phase is a superfluid which is viscously decoupled from the QCM. Because the KT line intersects at coexistence the actual mechanism to which superfluidity is created is uncertain. Essentially superfluid is born and does not go through the standard KT mechanism.

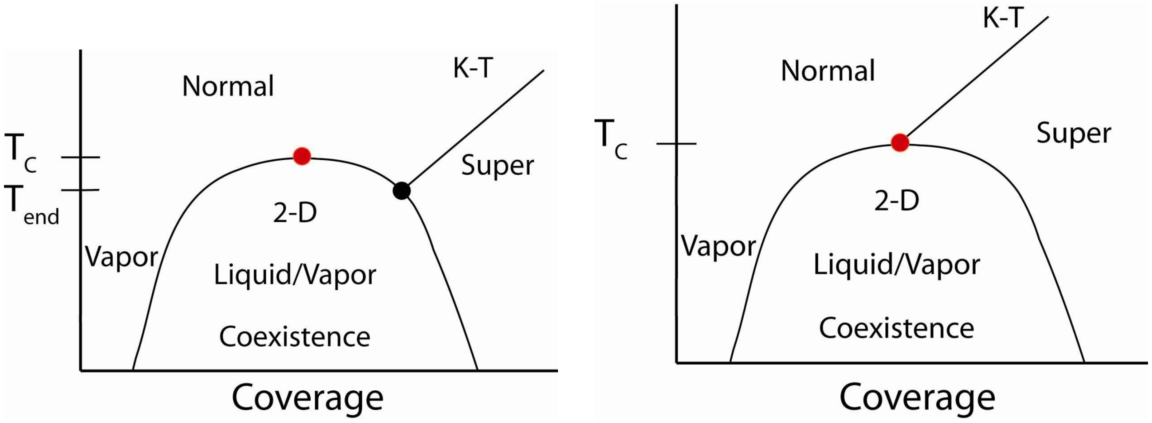

(a) The KT transition intersects the coexistence curve on the side marked by the black circle and at a temperature of T_{end}. The boundaries of the liquid/vapor coexistence region has a peak at the critical point marked by the red circle and the critical temperature T_c. Along an isotherm of increasing density a discontinuous step occurs at coexistence from thin to thick. Above the critical point a KT transition occurs.

(b) The KT line intersects the red critical point directly forming a tricritical point. Below the critical point the vapor discontinuously grows into a thick superfluid film jumping over its normal KT mechanism. Above the critical point the normal fluid transitions into a superfluid film.

Figure 5.3: Two possible phase diagrams for helium on sodium and lithium

A second phase diagram candidate is shown in figure 5.3(b). The KT transition intersects at the 2D critical point forming a tricritical point. The existence of this phase diagram should be experimentally identified by two distinct regimes in our QCM data above and below the critical point. At T>T_c a normal KT transition should occur. When T<T_c the experimental behavior is unclear as the fluid spontaneously forms a superfluid. The KT mechanism will be circumvented and superfluid film are born into existence. An ellipsometer measures total thickness and the superfluid state is hidden to it. So although the QCM data may be uncertain below the critical point the ellipsometric signal should measure clearly discontinuous steps as it cuts through the coexistence curve at constant temperature. At T>T_c we expect the ellipsometer data to increase in a smooth and continuous manner until saturation with no interruption.

5.4 Experimental Results

5.4.1 QCM Data

Ninety layers of lithium were ablated on each gold electrode of a QCM. Experimental isotherms at temperatures above and below the critical temperature are in figure 5.4. At temperatures below 0.9 K the abscissa was presented in millimoles of helium gas added to the entire volume. The frequency response in monolayers was shown in red on the left axis while the dissipation was on the right axis in blue. The 1.6 K isotherm shows a continuous growth from P=0 with a sudden drop at 3.5 layers. No solidification was observed as predicted for intermediate strength substrates. The dissipation also showed a peak at P/P_0=0.45. The pressure was normalized to the bulk vapor pressure and showed the behavior of a normal KT transition. The 0.5 K isotherm showed a region up to 0.02 millimoles where film growth was negligible followed by a quick rise and decline in film thickness. The peak reached a maximum at 0.4 layers before a superfluid type transition occurred. A corresponding peak in the dissipation also appeared at 0.025 millimoles. Although the features were the same as the KT mechanism it would be premature to call it as such. Hidden in the total film thickness could be additional features which are associated to superfluid being born into its new state.

Adsorption isotherms on ablated sodium have features very similar to the lithium data. Ninety layers were also ablated on each gold electrode. A smooth, continuous film grew for the 0.7 K and

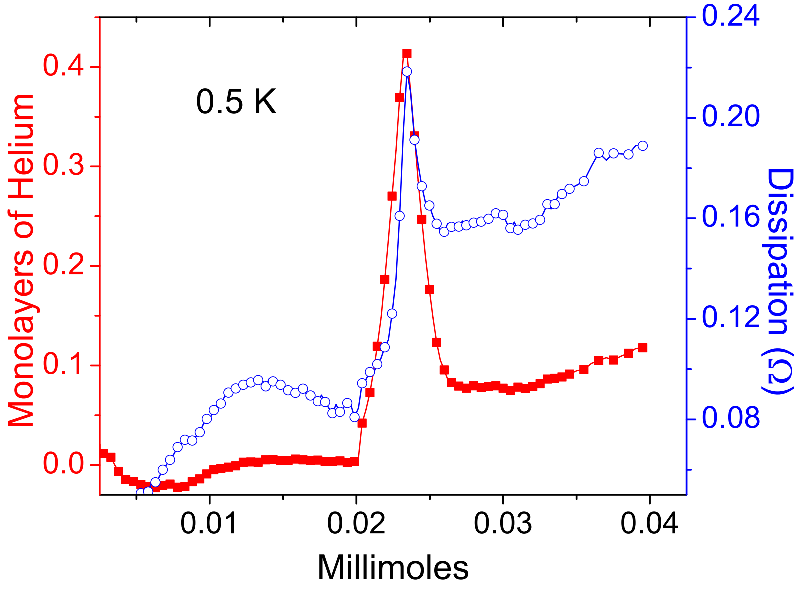

(a) Frequency (red) and dissipation (blue) response for a 0.5 K isotherm. The abscissa is in millimoles and frequency response is in monolayers of helium. No growth is observed until a sudden rise and drop beginning at 0.02 millimoles. A dissipation peak was also observed which coincides with the superfluid drop.

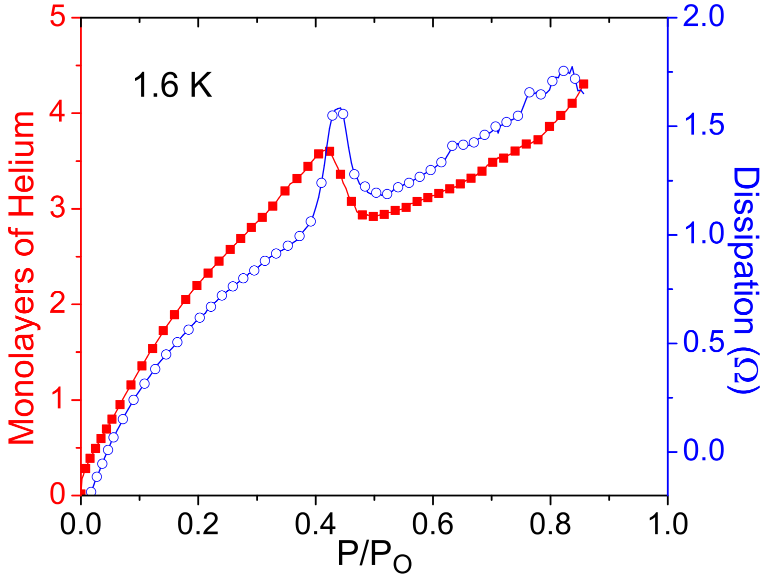

(b) The film shows a continuous growth from P=0 which was predicted for an intermediate strength substrate. At 0.45 P/P_0 the KT transition is observed with a frequency drop and dissipation peak.

Figure 5.4: QCM data for lithium

1.4 K isotherms. There were corresponding peaks in the dissipation as well. The features of the isotherms for T>T_c and T<T_c appeared to be the same and offered no clues to the location of the critical point. Perhaps the clues lies after the superfluid transition occurred. For both the lithium and sodium data the layer thickness at which the KT transition occurs was less than predicted by equation 5.2.

5.4.2 Ellipsometer Data

The combined ellipsometer and QCM data in figure 5.6 shows a complete picture of the helium film growth on sodium. The total film was measured by the ellipsometer and the normal fraction by the QCM. The superfluid fraction was the difference between the two. The ellipsometer signal was the ratio of the second to the first harmonic. For low pressures the QCM (black squares) and ellipsometer (red circles) data matched well until the KT transition. The superfluid decouples from the QCM and the resonance decreased. The ellipsometer signal was unaffected by the superfluid transition and continued uninterrupted until an ”infinite” layer growth occurred at saturation. The QCM signal after the layer drop grew steadily until saturation where a rapid growth also appeared. Although most of the superfluid is decoupled some motion in the normal direction can still be measured by the QCM. The difference between the ellipsometric and QCM signal was the superfluid fraction. Two isotherms at T>T_c and T<T_c showed similar features with no indication of a discontinuous film thickness. The existence of a discontinuous step also implies a critical point at which the discontinuous step size approaches zero. The dissipation plots were not plotted but do mark a peak in the dissipation for above and below the critical point at the same location as the frequency drop. These isotherms were representative of the results for several isotherms on a number of different QCM and sodium films.

Suspecting rough surfaces of the gold electrodes as the reason for the absence of a liquid/vapor transition HOPG was substituted for the supporting substrate. Before ablating a sodium film on the HOPG we did an isotherm at 0.5 K and 0.7 K. The 0.7 K isotherm is shown in figure 5.7 for the 2f/1f ellipsometer signal as it was the most sensitive. The ellipsometer conversion factor 0.0025

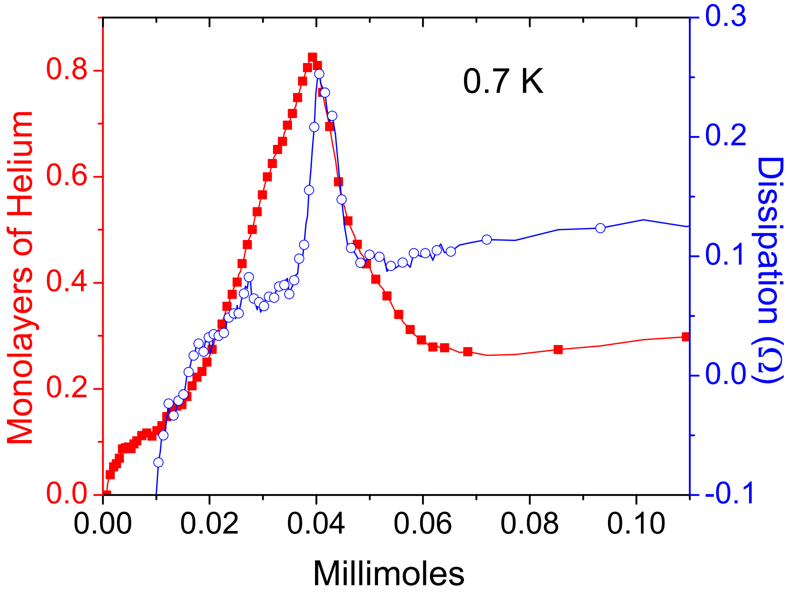

(a) Frequency and dissipation response of a 0.7 K sodium isotherm. The abscissa was in millimoles of added gas to the total volume. The film grew smooth and continuous until the onset of a superfluid like transition at a thickness of 0.85 layers. The dissipation also had a peak at the transition.

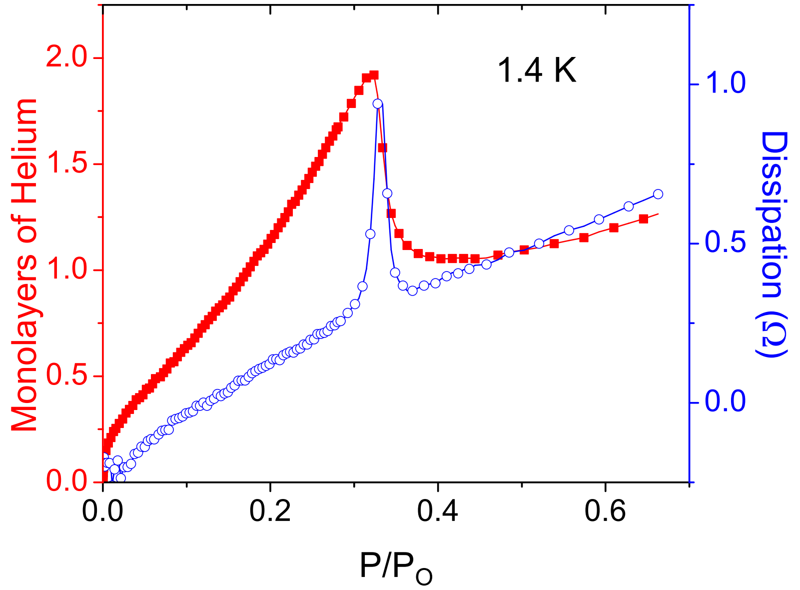

(b) Frequency and dissipation response of a 1.4 K sodium isotherm. The pressure was normalized to the bulk vapor pressure at 1.4 K. The film grew smooth and continuous until the KT transition at a thickness of 2 layers.

Figure 5.5: QCM data for sodium

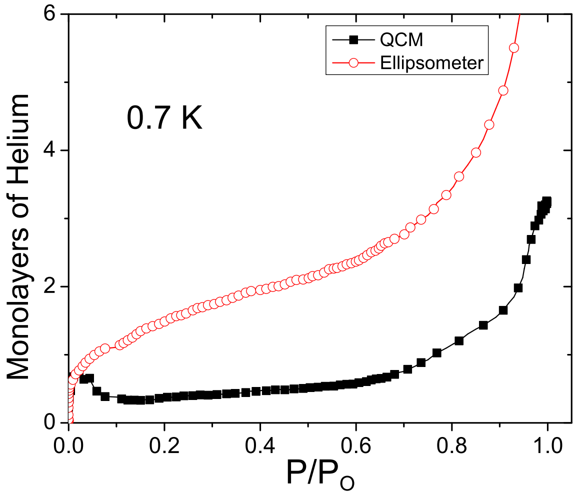

(a) The frequency response converted to the unit of layers as a function of pressure for a 0.7 K helium isotherm on sodium. The red circles are for the 2f/1f ellipsometer signal and the black squares for the QCM response. At P/P_0 ≈0.008 the frequency drop associated with a superfluid transition occurred. The expected discontinuous step in film growth was not observed below the critical point T≈0.8 K. A conversion factor of 0.002789 signal/layer was used, 11% higher than theory.

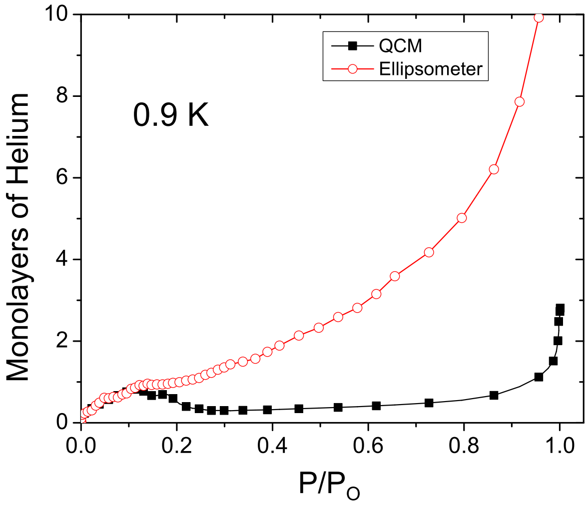

(b) A 0.9 K helium isotherm on sodium. At P/P_0=0.15 the KT transition causes the QCM to decouple from the superfluid fraction. The conversion factor for the 2f/1f data was 0.0006043 signal/layer was used, 25% lower than theory.

Figure 5.6: QCM and ellipsometer film thickness

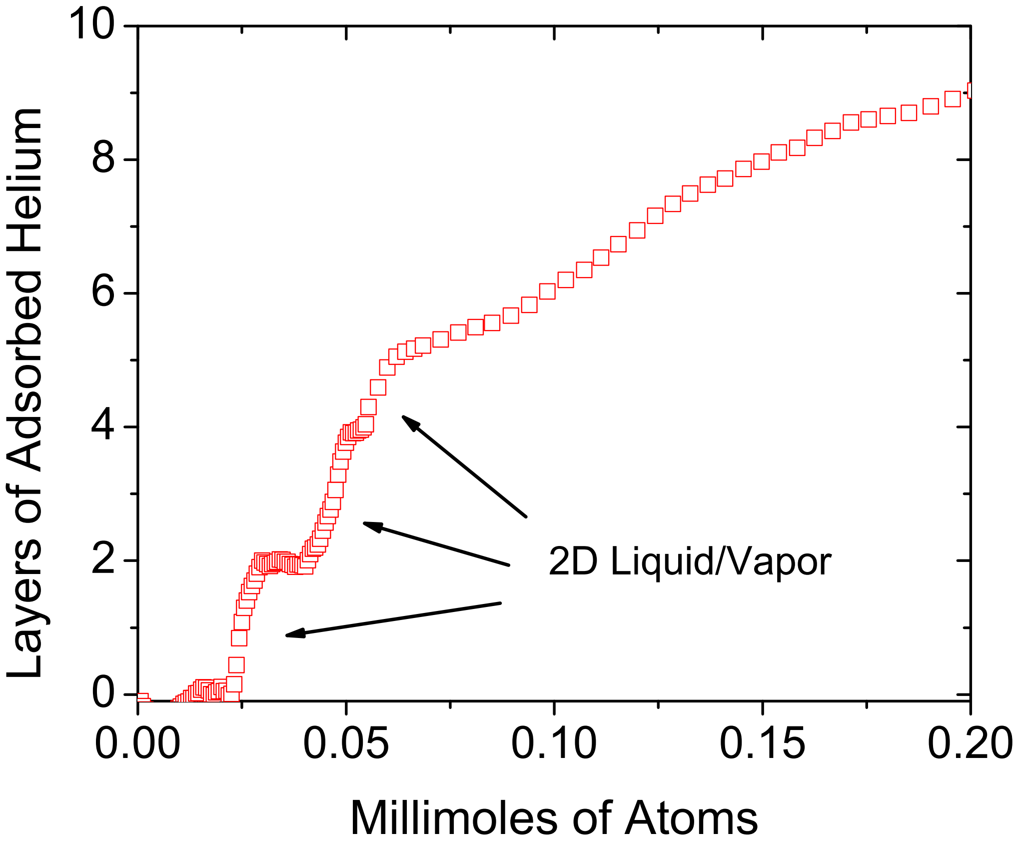

Figure 5.7: The 2f/1f ellipsometer signal has three steps indicated by the arrows. The first two layers grew instantly at the first introduction of helium. The calibration constant was found by fitting the first step to mark the growth of two layers. This two layer growth had been measured in [86]. After the third layer the film grew continuously until saturation.

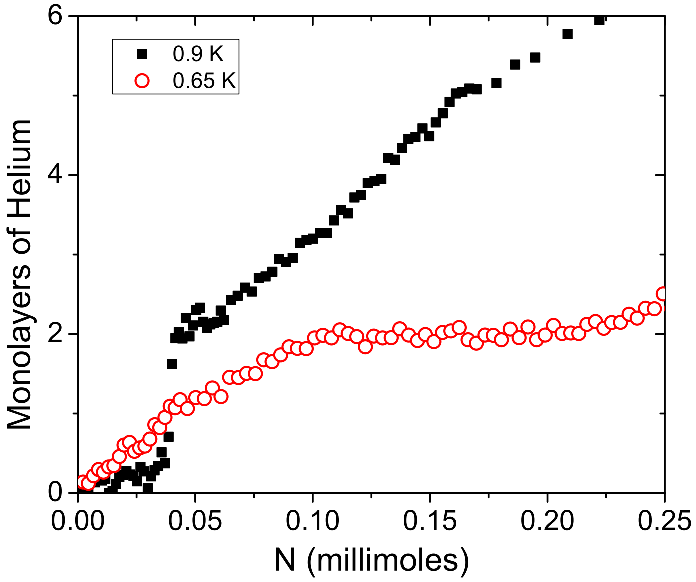

(a) The 2f/1f ratio measuring film thickness versus millimoles of helium-4 added to the cell were plotted together. A clear step in the 0.65 K was present while absent at 0.9 K. The theoretical value 0.0025 signal/layer converted the signal change to layer growth.

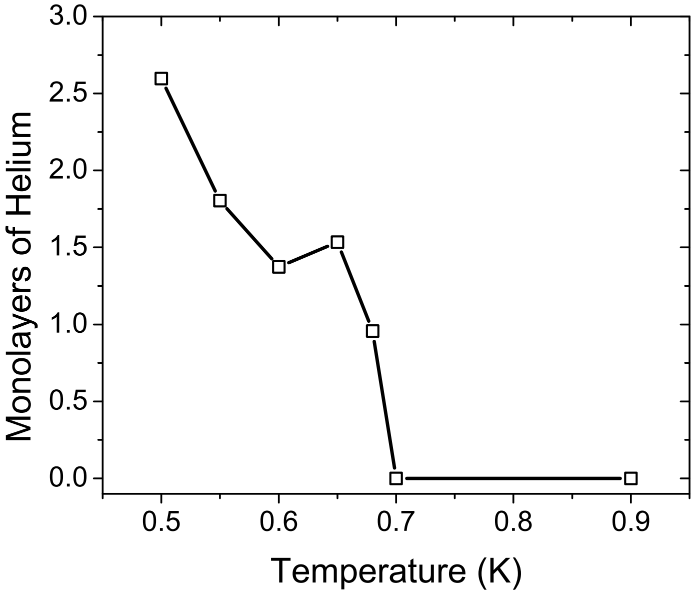

(b) The size of the discontinuous step for each isotherm was plotted as a function of temperature. The step size decreased until it disappeared between 0.68 K and 0.7 K. This indicated the first evidence of a 2D critical point on sodium.

Figure 5.8: Evidence for 2D critical point on sodium

signal/layer was chosen to have the first step be equal to two layers as that has been observed previously [86]. The conversion factor was 6 times greater than theoretical calculations. Without a QCM the ellipsometer was the sole measurement device and the superfluid fraction was undetectable. Similar to ref. [86] three steps can be observed before the growth became smooth and continuous. The discontinuous steps meant the substrate was atomically smooth and the HOPG surface appeared to be sufficiently clean and smooth for the sodium film. After the helium was pumped out of the cell sodium was ablated onto the HOPG. The same parameters used to ablate 90 layers of sodium on a QCM was repeated on the HOPG. The ellipsometer measured on the bare sodium film reported an index of refraction similar to the bulk values.

A series of isotherms at T<T_c clearly showed a discontinuous step in the 2f/1f ellipsometer signal. After the discontinuous step the film thickened continuously until an infinite film formed at saturation. At T>T_c the step disappeared and the film grew in a smooth and continuous manner from P=0 to saturation. The 0.65 K and 0.9 K isotherms are shown in figure 5.8(a) with the step size clearly present in the 0.65 K data and absent in the 0.9 K data. A plot of the step size as a function of temperature in figure 5.8(b) shows the step size approaching zero at a temperature between 0.68 K and 0.7 K. This plot indicates the first evidence of a 2D critical point on sodium.

5.5 Conclusion

We present the first evidence of a 2D critical point on sodium. As to why this was not observed on the QCM could be attributed to the surface roughness of the gold electrodes. A rough surface can smear the critical temperature. Using an atomically smooth HOPG as the backbone would create smoother alkali films. With a sodium/HOPG system a discontinuous step decreased to zero at a critical temperature between 0.68 K and 0.7 K. The ellipsometer only provides total film thicknesses and is invisible to superfluid transitions. A complete phase diagram requires for a QCM to be used. Providing a smoother substrate for the alkali films appeared to be the key to observe the 2D critical point. The gold QCMs we used in our research had macroscopic scratches which were sent back to be smoothed away by Laptech Precision Inc. The crystals used in these sets of experiments could have come from a bad batch of crystals. A new batch of crystals should be tested before dismissing the gold substrates as the supporting substrate. A second option has been shown recently in ref. [105, 106, 107, 108]. HOPG samples could be bonded to the gold electrodes of the QCM followed by ablation of the alkali metals onto the HOPG. We hope with either of these improvements the full phase diagram for helium on lithium, sodium, and magnesium films can be measured.

Further work is needed to refine the ellipsometer where several factors are needed to be understood. The discrepancy between theoretical and experimental conversion factors can differ by as much 4 times when compared to QCM signals. The differences could be related to the temperature dependent index of refraction and potentially the effects of the gold underlying films being still dominant. Ablating much thicker films would be a possible solution to this problem. Another oddity to our system is a sinusoidal variation in the signal on the order of a few hours was also present which was not a result of laser frequency variations. It appeared to be thermal in nature and though it did not affect our results the source of this noise should be clarified.

Chapter 6

Conclusion

We have experimentally surveyed various flow regimes of gases, liquids, and superfluid through single nanopores. The robustness and accuracy of a calibrated mass spectrometer was shown with the observation of a number of transitions in regimes and phases. For the classical liquid and vapor the much debated no slip boundary condition was investigated for nitrogen and helium. To the accuracy of our measurements the flow had a slip length of zero matching a normal macroscopic system well. Surface tension though was found to be dominant in the nano flows having a significant impact on its flow. In normal liquid helium a simple two phase model which included the effects of a curved interface was presented to explain our measurements which showed a pressure independent flow at low temperatures and an inhibited flow near the critical temperature. In superfluid both intrinsic and extrinsic nucleation mechanism were observed to be present in a submicron nanotube. These results are in contrast to flows through orifices which an extrinsic nucleation is noticeably absent. The results of this thesis and future research directions outlined in the chapters have many applications in the world where a liquid/vapor interfaces are needed. Separation of gases and liquids, purification of particles, turbulent phenomena, and superfluid plugs as satellite thrusters are just a few examples which nano scaled phenomena are important.

The phase transitions of chemically pure helium on the alkali metals provide a particularly simple model system which enhances the fundamental understanding of surface science. As research continues approaching the nano scale surface phenomena becomes ever more dominant.

Chemical reactions on surfaces for energy production, adsorptions of impurities, and controlling the hydrophobicity of industrial materials are a few examples of the importance of surface physics. Our investigation focused on the competition between the classical (liquid and vapor) and quantum (superfluid) phases on intermediate strength substrates. With a highly stable ellipsometer we measured the liquid/vapor transition of sodium on an atomically smooth HOPG substrate. The first evidence of the two dimensional critical point on sodium was measured at T_c=0.7 K. There is still much work left to completely map out the full phase diagram for lithium and sodium but as the research in this thesis shows we are headed in the right direction.

Bibliography

[1] S. Pezzagna, D. Rogalla, H. W. Becker, I. Jakobi, F. Dolde, B. Naydenov, J. Wrachtrup, F. Jelezko, C. Trautmann, and J. Meijer, Physica Status Solidi a-Applications and Materials Science **208**, 2017 (2011).

[2] S. Howorka and Z. Siwy, Chemical Society Reviews **38**, 2360 (2009).

[3] M. Pevarnik, K. Healy, M. E. Toimil-Molares, A. Morrison, S. E. Létant, and Z. S. Siwy, Acs Nano **6**, 7295 (2012).

[4] B. Bhushan, Beilstein Journal of Nanotechnology **2**, 66 (2011).

[5] S. Gruener and P. Huber, Physical Review Letters **100** (2008).

[6] T. G. Knudstrup, I. A. Bitsanis, and G. B. Westermannclark, Langmuir **11**, 893 (1995).

[7] J. T. Cheng and N. Giordano, Physical Review E **65** (2002).

[8] S. Sinha, M. P. Rossi, D. Mattia, Y. Gogotsi, and H. H. Bau, Physics of Fluids **19** (2007).

[9] Z. Yang and S. V. Garimella, Physics of Fluids **21** (2009).

[10] N. V. Churaev, V. D. Sobolev, and A. N. Somov, Journal of Colloid and Interface Science **97**, 574 (1984).

[11] C. H. Choi, K. J. A. Westin, and K. S. Breuer, Physics of Fluids **15**, 2897 (2003).

[12] A. Maali, T. Cohen-Bouhacina, and H. Kellay, Applied Physics Letters **92** (2008).

[13] R. Pit, H. Hervet, and L. Leger, Physical Review Letters **85**, 980 (2000).

[14] D. C. Tretheway and C. D. Meinhart, Physics of Fluids (1994-present) **14**, L9 (2002).

[15] X. Zheng, G. P. Kong, and Z. H. Silber-Li, Acta Mechanica Sinica **29**, 411 (2013).

[16] J. P. Rothstein, *Slip on Superhydrophobic Surfaces* (Annual Reviews, Palo Alto, 2010), vol. 42 of *Annual Review of Fluid Mechanics*, pp. 89–109.

[17] J. K. Holt, H. G. Park, Y. M. Wang, M. Stadermann, A. B. Artyukhin, C. P. Grigoropoulos, A. Noy, and O. Bakajin, Science **312**, 1034 (2006).

[18] M. Majumder, N. Chopra, R. Andrews, and B. J. Hinds, Nature **438**, 44 (2005).

[19] M. Majumder, N. Chopra, and B. J. Hinds, Acs Nano **5**, 3867 (2011).

[20] A. Noy, H. G. Park, F. Fornasiero, J. K. Holt, C. P. Grigoropoulos, and O. Bakajin, Nano Today **2**, 22 (2007).

[21] M. Whitby, L. Cagnon, M. Thanou, and N. Quirke, Nano Letters **8**, 2632 (2008).

[22] G. Karniadakis, A. Beskök, and N. R. Aluru, *Microflows and nanoflows fundamentals and simulation* (2005).

[23] T. Young, Philosophical Transactions of the Royal Society of London **95**, 65 (1805).

[24] P.-S. Laplace, Traite de Mecanique Celeste **4**, 1 (1805).

[25] L. D. Landau and E. M. Lifshitz, *Fluid mechanics*, Course of Theoretical Physics (Pergamon Press, 1959).

[26] A. E. Velasco, S. G. Friedman, M. Pevarnik, Z. S. Siwy, and P. Taborek, Physical Review E **86** (2012).

[27] M. Savard, C. Tremblay-Darveau, and G. Gervais, Physical Review Letters **103** (2009).

[28] M. Savard, G. Dauphinais, and G. Gervais, Physical Review Letters **107** (2011).

[29] A. E. Velasco, C. Yang, Z. S. Siwy, M. E. Toimil-Molares, and P. Taborek, Applied Physics Letters **105** (2014).

[30] F. Sharipov, I. Graur, and C. Day, Journal of Vacuum Science and Technology A **28**, 443 (2010).

[31] N. B. Zolotoi, G. V. Karpov, V. E. Skurat, and V. L. Tal'roze, Soviet Physics - Doklady **24**, 69 (1979).

[32] R. J. Donnelly, *Quantized vortices in helium, ii* (1991).

[33] A. E. Velasco, *Masters Thesis* (University of California-Irvine, 2012).

[34] Z. Siwy, P. Apel, D. Baur, D. D. Dobrev, Y. E. Korchev, R. Neumann, R. Spohr, C. Trautmann, and K. O. Voss, Surface Science **532**, 1061 (2003).

[35] M. R. Powell, I. Vlassiouk, C. Martens, and Z. S. Siwy, Physical Review Letters **103** (2009).

[36] L. Chang Young, C. Wonjoon, H. Jae-Hee, and M. S. Strano, Science **329**, 1320 (2010).

[37] J. A. Quinn, J. L. Anderson, W. S. Ho, and W. J. Petzny, Biophysical Journal **12**, 990 (1972).

[38] J. C. Burton, E. Van Cleve, and P. Taborek, Cryogenics **51**, 209 (2011).

[39] F. Sharipov and V. Seleznev, Journal of Physical and Chemical Reference Data **27**, 657 (1998).

[40] F. M. Huisman, A. E. Velasco, E. Van Cleve, and P. Taborek, Journal of Low Temperature Physics pp. 1–14 (2014).

[41] P. Clausing, Journal of Vacuum Science and Technology **8**, 636 (1971).

[42] M. Lorenzini, G. L. Morini, and S. Salvigni, International Journal of Thermal Sciences **49**, 248 (2010).

[43] S. Müller, C. Schötz, O. Picht, W. Sigle, P. Kopold, M. Rauber, I. Alber, R. Neumann, and M. E. Toimil-Molares, Crystal Growth and Design **12**, 615 (2011).

[44] E. Lauga and H. A. Stone, Journal of Fluid Mechanics **489**, 55 (2003).

[45] A. J. H. McGaughey and C. A. Ward, Journal of Applied Physics **91**, 6406 (2002).

[46] C. A. Ward and D. Stanga, Physical Review E **64** (2001).

[47] R. Holyst and M. Litniewski, Journal of Chemical Physics **130** (2009).

[48] A. L. Woodcraft and A. Gray, *A low temperature thermal conductivity database* (Amer Inst Physics, Melville, 2009), vol. 1185 of *AIP Conference Proceedings*, pp. 681–684.

[49] G. K. White and P. J. Meeson, *Experimental techniques in low-temperature physics fourth edition*, Experimental techniques in low-temperature physics (Clarendon Press: Oxford University Press, 2002).

[50] R. T. Jacobsen, R. B. Stewart, and M. Jahangiri, Journal of Physical and Chemical Reference Data **15**, 735 (1986).

[51] R. Span, E. W. Lemmon, R. T. Jacobsen, W. Wagner, and A. Yokozeki, Journal of Physical and Chemical Reference Data **29**, 1361 (2000).

[52] B. A. Younglove, Tech. Rep., DTIC Document (1982).

[53] G. J. Dunn, S. K. Wilson, B. R. Duffy, S. David, and K. Sefiane, Colloids and Surfaces a-Physicochemical and Engineering Aspects **323**, 50 (2008).

[54] I. Satoh, K. Fushinobu, and Y. Hashimoto, International Journal of Refrigeration **25**, 226 (2002).

[55] URL `http://ffden-2.phys.uaf.edu/212_fall2003.web.dir/Rodney_Guritz%20Folder/properties.htm`.

[56] R. J. Donnelly and C. F. Barenghi, Journal of Physical and Chemical Reference Data **27**, 1217 (1998).

[57] P. W. Anderson, Reviews of Modern Physics **38**, 298 (1966).

[58] K. Schwab, R. Bruckner, and R. E. Packard, Nature **386**, 585 (1997).

[59] R. P. Feynman, *Chapter II Application of Quantum Mechanics to Liquid Helium* (Elsevier, 1955), vol. Volume 1, pp. 17–53.

[60] J. P. Hulin, Dhumiere.D, B. Perrin, and Libchabe.A, Physical Review A **9**, 885 (1974).

[61] G. B. Hess, Physical Review Letters **27**, 977 (1971).

[62] G. Marees, R. P. Slegtenhorst, and H. Vanbeelen, Journal of Low Temperature Physics **51**, 165 (1983).

[63] A. Talmi and J. Landau, Journal of Low Temperature Physics **12**, 275 (1973).

[64] Glaberson.Wi and R. J. Donnelly, Physical Review **141**, 208 (1966).

[65] G. B. Hess, Physical Review Letters **29**, 96 (1972).

[66] J. S. Langer and M. E. Fisher, Physical Review Letters **19**, 560 (1967).

[67] H. A. Notarys, Physical Review Letters **22**, 1240 (1969).

[68] J. Steinhauer, K. Schwab, Y. Mukharsky, J. C. Davis, and R. E. Packard, Physical Review Letters **74**, 5056 (1995).

[69] W. Zimmermann, C. A. Lindensmith, and J. A. Flaten, Journal of Low Temperature Physics **110**, 497 (1998).

[70] E. Varoquaux, O. Avenel, and M. W. Meisel, Canadian Journal of Physics **65**, 1377 (1987).

[71] A. Amar, Y. Sasaki, R. L. Lozes, J. C. Davis, and R. E. Packard, Physical Review Letters **68**, 2624 (1992).

[72] R. E. Packard and S. Vitale, Physical Review B **45**, 2512 (1992).

[73] G. G. Ihas, O. Avenel, R. Aarts, R. Salmelin, and E. Varoquaux, Physical Review Letters **69**, 327 (1992).

[74] J. C. Davis, J. Steinhauer, K. Schwab, Y. M. Mukharsky, A. Amar, Y. Sasaki, and R. E. Packard, Physical Review Letters **69**, 323 (1992).

[75] C. R. Lages, R. H. Torii, and D. B. DeBra, Cryogenics **35**, 31 (1995).

[76] U. Schmidtchen, Journal of Low Temperature Physics **97**, 365 (1994).

[77] U. Schotte, Zeitschrift Fur Physik B-Condensed Matter **48**, 183 (1982).

[78] K. W. Schwarz, Physical Review B **38**, 2398 (1988).

[79] W. F. Vinen and J. J. Niemela, Journal of Low Temperature Physics **128**, 167 (2002).

[80] V. K. Chagovets, E. Y. Rudavskii, K. U. Taubenreuther, and G. Eska, Physica B **284**, 2045 (2000).

[81] I. Gritsenko, A. Zadorozhko, and G. Sheshin, Journal of Low Temperature Physics **171**, 194 (2013).

[82] M. J. Lea and P. Fozooni, Journal of Low Temperature Physics **56**, 25 (1984).

[83] A. Del Maestro, M. Boninsegni, and I. Affleck, Physical Review Letters **106**, 105303 (2011).

[84] E. Cheng, G. Ihm, and M. W. Cole, Journal of Low Temperature Physics **74**, 519 (1989).

[85] M. C. Gordillo and D. M. Ceperley, Physical Review B **58**, 6447 (1998).

[86] T. McMillan, J. E. Rutledge, and P. Taborek, Journal of Low Temperature Physics **138**, 995 (2005).

[87] P. A. Crowell and J. D. Reppy, Physical Review B **53**, 2701 (1996).

[88] J. E. Rutledge and P. Taborek, Physical Review Letters **69**, 937 (1992).

[89] D. Ross, J. E. Rutledge, and P. Taborek, Science **278**, 664 (1997).

[90] D. Ross, P. Taborek, and J. E. Rutledge, Journal of Low Temperature Physics **111**, 1 (1998).

[91] P. Taborek and J. E. Rutledge, Physical Review Letters **68**, 2184 (1992).

[92] P. Taborek and J. E. Rutledge, Physical Review Letters **71**, 263 (1993).

[93] P. Taborek and J. E. Rutledge, Berichte Der Bunsen-Gesellschaft-Physical Chemistry Chemical Physics **98**, 361 (1994).

[94] J. A. Phillips, D. Ross, P. Taborek, and J. E. Rutledge, Physical Review B **58**, 3361 (1998).

[95] J. A. Phillips, P. Taborek, and J. E. Rutledge, Journal of Low Temperature Physics **113**, 829 (1998).

[96] E. Van Cleve, P. Taborek, and J. E. Rutledge, Journal of Low Temperature Physics **150**, 1 (2008).

[97] R. J. Lazarowich and P. Taborek, Physical Review B **74** (2006).

[98] M. Rodahl, F. Höök, A. Krozer, P. Brzezinski, and B. Kasemo, Review of Scientific Instruments **66**, 3924 (1995).

[99] T. McMillan, P. Taborek, and J. E. Rutledge, Review of Scientific Instruments **75**, 5005 (2004).

[100] E. Van Cleve, *Ph.D. Thesis* (University of California-Irvine, 2011).

[101] R. M. A. Azzam and N. M. Bashara, *Ellipsometry and polarized light*, Ellipsometry and polarized light (North-Holland, 1977).

[102] M. J. Weber, *Handbook of optical materials*, vol. 19 (CRC press, 2002).

[103] J. Monin and G. A. Boutry, Physical Review B **9**, 1309 (1974).

[104] G. E. Jellison, J. D. Hunn, and H. N. Lee, Physical Review B **76** (2007).

[105] N. Hosomi, A. Tanabe, M. Suzuki, and M. Hieda, Physical Review B **75** (2007).

[106] N. Hosomi and M. Suzuki, Physical Review B **77** (2008).

[107] F. Nihei, K. Ideura, H. Kobayashi, J. Taniguchi, and M. Suzuki, Journal of Low Temperature Physics **162**, 559 (2011).

[108] K. Noda, K. Okamura, J. Taniguchi, M. Suzuki, and M. Hieda, Journal of Low Temperature Physics **171**, 638 (2013).